Development of a Zero-Dimensional Thermodynamic Model for Internal Combustion Engines: Application to Diesel and Hydrogen Fuels

Siddharth Jain

Delft University of Technology

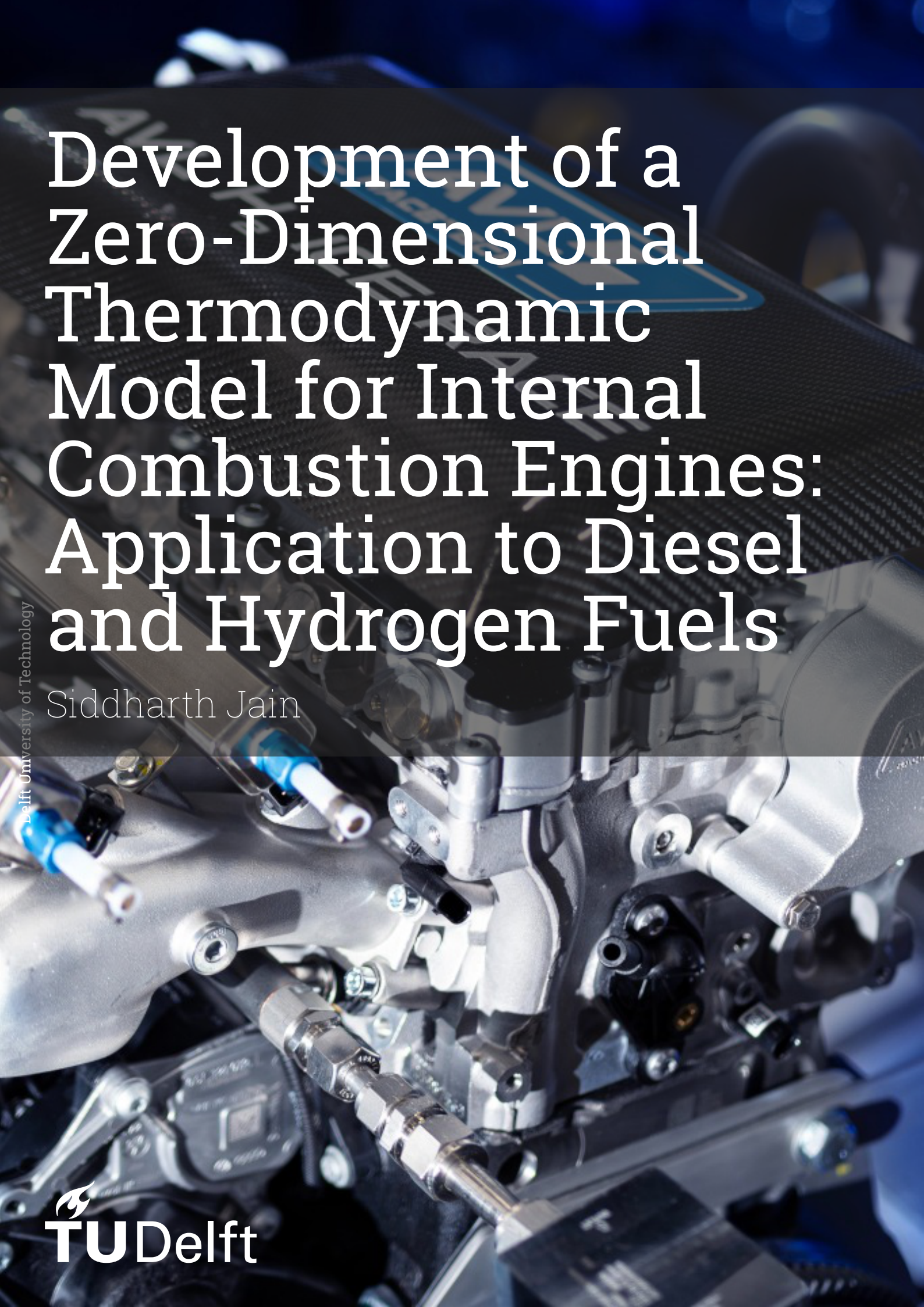

TU Delft

Development of a Zero-Dimensional Thermodynamic Model for Internal Combustion Engines: Application to Diesel and Hydrogen Fuels

by

Siddharth Jain

to obtain the degree of Master of Science
at the Delft University of Technology,
to be defended publicly on Thursday July 10, 2025.

Student Number:	5926378	
Project Duration:	December 2024 - July 2025	
Thesis Committee:	Prof.dr.ir. B.J. Boersma	Supervisor, TU Delft
	Prof.dr. R. Pecnik	Co-Supervisor, TU Delft
	Prof.dr.ir. S.A. Klein	Member, TU Delft

An electronic version of this thesis is available at `http://repository.tudelft.nl/`.
Cover Image: Hydrogen Internal Combustion Engine by AVL RACETECH [1]

TU Delft

Acknowledgements

I would like to express my gratitude to many individuals who supported and guided me while I completed this master's thesis. They have made invaluable personal and professional contributions.

First and foremost, I would like to express my profound gratitude to Prof. Dr.ir. B.J. Boersma, who supervised my thesis. His suggestions, helpful criticism, and constant backing have been crucial in determining the direction and outcome of this research. Throughout this challenging but rewarding project, Professor Boersma's knowledge and guidance were invaluable.

I am equally grateful to my co-supervisor, Prof.dr. R. (René) Pecnik. His willingness to dedicate valuable time for insightful discussions and to offer constructive criticism significantly enhanced the quality and depth of this work. His perspectives provided crucial refinements to my research.

On a more personal note, this journey would not have been possible without the steadfast encouragement and understanding of my family and friends. To my parents and family, thank you for your unconditional love, patience, and for instilling in me the value of perseverance. Your belief in me has been a constant source of motivation. To my friends, near and far, thank you for your companionship, understanding during long hours of work, and for providing a much-needed balance to academic life. Your support has been a true blessing.

Siddharth Jain
Delft, June 2025

Abstract

To improve the understanding and analysis of internal combustion engines, this thesis develops a thermodynamic model that simplifies the complex processes within an engine cylinder into a single, uniform system. The core energy conversion phases of compression and expansion were first simulated using a computationally effective ”zero-dimensional” method, which was first applied to a diesel engine using MATLAB. A key investigation involved comparing four established empirical models used to estimate in-cylinder heat loss, a critical factor for engine efficiency. This comparison revealed that there are significant variations in the predicted engine performance depending on the model choice. The diesel simulation was then validated against experimental data and refined using more realistic gas properties and a dual-zone combustion model to better represent the diesel combustion.

A major contribution of this work was adapting the validated framework to a hydrogen-fuelled spark-ignition engine, testing the model's flexibility for alternative fuels. This involved recalibrating fuel properties and the combustion model to match hydrogen's unique burning characteristics. When compared against experimental results, the simulation accurately replicated in-cylinder pressure and energy release patterns. The Woschni heat loss model was identified as most representative for the hydrogen experiments; however, the simulation consistently overestimated the engine's work output and thermal efficiency.

The study concludes that these simplified models are highly effective for analysing internal thermodynamic trends and comparing the behaviour of different fuels. However, their ability to predict absolute performance is fundamentally limited by the accuracy of the empirical sub-models used for heat transfer and, most significantly, combustion. This work underscores that achieving high-accuracy performance predictions from such models requires robust experimental calibration to account for real-world combustion inefficiencies not captured by idealised functions.

Contents

List of Figures

List of Tables

Nomenclature

Abbreviations

Abbreviation	Definition
AFR	Air-Fuel Ratio
aROHR	Average Rate of Heat Release
ATDC	After Top Dead Centre
BDC	Bottom Dead Centre
BTDC	Before Top Dead Centre
CA	Crank Angle
CFD	Computational Fluid Dynamics
CHTC	Convective Heat Transfer Coefficient
CI	Compression Ignition
CIDI	Compression Ignition Direct Injection
CO	Carbon Monoxide
CO_2	Carbon Dioxide
CR	Compression Ratio
DI	Direct Injection
DW	Double Zone Wiebe
EU	European Union
EV	Electric Vehicle
EVO	Exhaust Valve Opening
FMEP	Friction Mean Effective Pressure
HCCI	Homogeneous Charge Compression Ignition
HCNG	Hydrogen-Enriched Natural Gas
HTC	Heat Transfer Coefficient
ICE	Internal Combustion Engine
IMEP	Indicated Mean Effective Pressure
IVC	Intake Valve Closing
LHV	Lower Heating Value
NO_x	Nitrogen Oxides
0D	Zero-Dimensional
PV	Pressure-Volume
RPM	Revolutions Per Minute
SI	Spark Ignition
SoC	Start of Combustion
SW	Single Zone Wiebe
TDC	Top Dead Centre

Symbols

Latin Symbols

Symbol	Definition	Unit
a	Wiebe efficiency parameter (also Crank radius = $S/2$)	[-] (or m)
A_s	Instantaneous heat transfer surface area	m^2
B	Cylinder bore	m
b_{st}	Dimensionless tuning parameter for swirl (Sitkei)	[-]
$C_0, C_1, ...$	Empirical constants for heat transfer correlations	[-]
c_p	Specific heat at constant pressure	$\mathrm{kJ\,kg^{-1}\,K^{-1}}$
c_v	Specific heat at constant volume	$\mathrm{kJ\,kg^{-1}\,K^{-1}}$
d_e	Equivalent hydraulic diameter	m
E_{ref}	Reference energy ($P_{BDC} \cdot V_{BDC}$)	J
h_c	Convective heat transfer coefficient	$\mathrm{W\,m^{-2}\,K^{-1}}$
h_{dim}	Dimensionless heat transfer coefficient	[-]
k	Thermal conductivity	$\mathrm{W\,m^{-1}\,K^{-1}}$
l	Connecting rod length	m
m	Mass	kg
$\dot{m}$	Mass flow rate	$\mathrm{kg\,h^{-1}}$
M	Molar mass	$\mathrm{g\,mol^{-1}}$
n	Wiebe form or shape factor	[-]
N	Engine speed	RPM
N'	Engine speed	$\mathrm{rev/s}$
Nu	Nusselt number	[-]
P	In-cylinder pressure	Pa
P_b	Brake Power	kW
Pr	Prandtl number	[-]
Q	Heat Transfer	J
$\dot{Q}$	Heat transfer rate	W
q''	Wall heat flux	$\mathrm{W\,m^{-2}}$
r	Compression ratio	[-]
R	Specific gas constant	$\mathrm{kJ\,kg^{-1}\,K^{-1}}$
$\bar{R}$	Universal gas constant	$\mathrm{J\,mol^{-1}\,K^{-1}}$
R_c	Ratio of connecting rod length to crank radius (l/a)	[-]
Re	Reynolds number	[-]
S	Stroke length	m
t	Time	s
T	Absolute temperature	K
t_w	Dimensionless wall temperature (T_w/T_{BDC})	[-]
U	Internal energy	J
$\bar{U}_p$	Mean piston speed	$\mathrm{m\,s^{-1}}$
V	Volume	m^3
w	Characteristic gas velocity	$\mathrm{m\,s^{-1}}$
W	Work	J
x_b	Wiebe mass fraction burned	[-]
y	Instantaneous combustion chamber height	m
y_i	Molar fraction of species i	[-]

Greek Symbols

Symbol	Definition	Unit
β	Dimensionless volume scaling factor	[-]
Δ	Finite change in a quantity (e.g., ΔU)	(varies)
δ	Inexact differential for a path function (e.g., δQ)	(varies)
γ	Specific heat ratio (c_p/c_v)	[-]
η	Efficiency	%
θ	Crank angle	°CA
κ	Fuel fraction for premixed combustion (double Wiebe)	[-]
λ	Air-fuel equivalence ratio	[-]
μ	Dynamic viscosity	$\mathrm{Pa\,s}$
ρ	Density	$\mathrm{kg\,m^{-3}}$
ω	Engine angular speed	$\mathrm{rad\,s^{-1}}$

Subscripts

Subscript	Definition
a	Air
b	Burned (fraction) or Brake (power/efficiency)
bth	Brake thermal (efficiency)
BDC	Bottom Dead Centre
c	Clearance (volume)
$char$	Characteristic (length, velocity)
d	Displacement (volume) or Duration (combustion)
exp	Experimental
f	Fuel
g or gas	Gas
$H2$	Hydrogen
hr	Heat Release
ht	Heat Transfer (to walls)
i	Index for species, step, or Indicated (performance)
in	Input
max	Maximum value
mix	Mixture
mot	Motoring
net	Net
$norm$	Normalised
$peak$	Peak of the graph
$prod$	Product
ref	Reference state
s	Start (of combustion) or Stoichiometric
th	Thermal
TDC	Top Dead Centre
$total$	Total
vol	Volumetric
w	Wall
$1, 2$	Designates first or second zone/stage

1

Introduction

1.1. Background

The global energy consumption has been growing over the years. This increase in the energy demands has been due to rising industrialisation and improving living standards, as well as population growth. The increased need for energy has placed significant stress on renewable energy sources, given the concerns of global warming and climate change. The annual global energy consumption per source can be seen in Figure 1.1 below from the year 1800 to 2023. The rising energy use makes it harder to switch from fossil fuels to cleaner energy sources. Low-carbon renewable energy must not only replace existing reliance on oil, gas, and coal, but also satisfy the growing global energy demand. This creates a two-fold challenge: meeting future needs and moving away from current fossil fuel dependence.

Hence, there is an increased dependence on fossil fuels today. The transport industry's combustion of these fossil fuels is one of the highest contributors to carbon emissions [2] as evident in Figure 1.2 . The combustion of fossil fuels like diesel or petrol produces harmful greenhouse gases such as CO_2, CO and even NO_x.

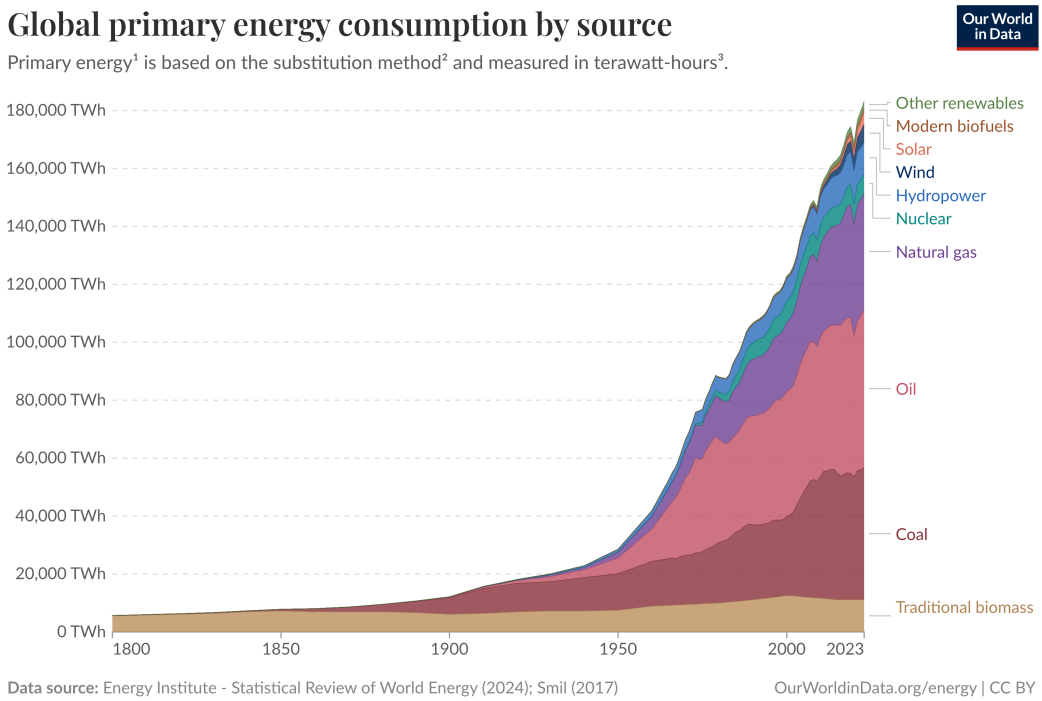

Figure 1.1: Annual Global Energy Consumption per Source Type [2]

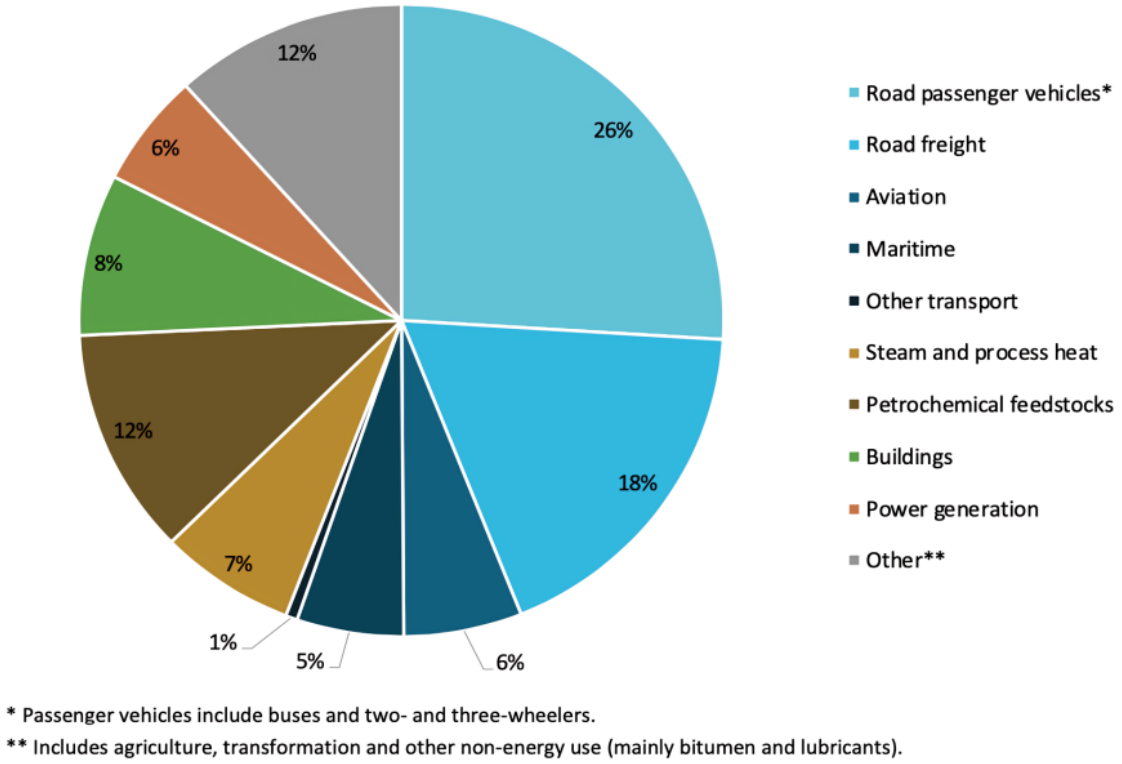

Figure 1.2: World Oil Consumption per Sector [3]

The combustion of fuel is done majorly through the internal combustion engines (ICE) used by cars, heavy-duty vehicles, ships and other modes of transport. The transport industry has also been exploring electric powertrains as a potential source to replace engines. However, given the challenges associated with electric powertrains, such as low energy density, range anxiety, limited charging infrastructure and environmental impacts of battery production [4], [5].

Since many forms of transport are heavily reliant on ICE, it is essential to further develop them. The ICE can be developed to enhance its efficiency to reduce emissions. Another method is to explore other fuels, such as hydrogen, which are renewable and offer carbon-neutral combustion possibilities. The literature currently lacks suitable heat loss models targeted for hydrogen combustion engines, and the aim of this thesis is to contribute to this research area. Companies such as TNO and Toyota are also working towards realising this technology [6], [7].

To contribute to this field, this thesis develops a zero-dimensional (0D) thermodynamic simulation to model in-cylinder heat loss. The work first focuses on a single-cylinder diesel engine, where the model is created and used to compare several established heat transfer correlations. Subsequently, this validated model serves as a foundation to simulate a hydrogen-fuelled engine, allowing for a comparative analysis of its distinct combustion and thermal characteristics.

1.2. Research Goals

This research aims to develop and utilise a computationally efficient zero-dimensional (0D) thermodynamic simulation model to investigate in-cylinder processes of internal combustion engines. To establish a robust baseline, the general model is first configured and validated using a compression-ignition Hatz diesel engine as the initial case study. The model's flexibility is then demonstrated by adapting it to simulate a spark-ignited hydrogen engine, which serves as a secondary validation and allows for a comparative analysis of alternative fuels. The key objectives of this work are:

- Develop a 0D thermodynamic engine model in MATLAB focusing on the closed cycle, capable of simulating key in-cylinder phenomena.
- Implement and comparatively evaluate established empirical models for in-cylinder heat transfer and combustion.
- Validate the simulation model against relevant experimental data from literature and fundamental thermodynamic principles to assess its predictive accuracy.
- Investigate model enhancements, such as dual-zone fuel combustion, to improve simulation fidelity.
- Extend the model's applicability to alternative fuels, specifically hydrogen, to analyse its distinct combustion and heat transfer characteristics.
- Ensure the modelling approach is traceable and reproducible by grounding it in established scientific literature.

1.3. Report Outline

This report details the development, validation, and application of a zero-dimensional (0D) thermodynamic simulation model for internal combustion engines, focusing on heat transfer and combustion phenomena.

Chapter 2: Internal Combustion Engines and Heat Transfer Modelling

- Working principles of 4-stroke CIDI engines and rationale for closed-cycle modelling.
- Core thermodynamic equations for in-cylinder analysis, including the first law, pressure gradient, and heat release rate.
- Empirical combustion modelling using the single-zone Wiebe function.
- Engine geometry, piston kinematics, and calculation of instantaneous volume and surface area.
- Convective heat transfer based on Newton's Law of Cooling and a detailed overview of empirical correlations (Woschni, Hohenberg, Sitkei, Assanis).

Chapter 3: 0D Thermodynamic Simulation: Methodology and Application

- Simulation methodology: MATLAB code architecture, Euler forward numerical integration, and a convergence study to determine optimal step size.
- Configuration of the baseline diesel simulation (Hatz 1D90E), including engine specifications, operating parameters, and modelling assumptions.
- Analysis of baseline diesel results, including in-cylinder thermodynamics, heat release profiles, and a quantitative comparison of performance metrics predicted by the different heat transfer models.

Chapter 4: Diesel Model Validation and Improvements

- Validation of the baseline diesel model against published experimental data for a Kubota 140 engine.
- Implementation and impact assessment of three key model improvements:
  - A double-zone Wiebe combustion model to represent premixed and diffusion phases.
  - A temperature-dependent specific heat ratio (γ) using the Gatowski model.
  - A composition-based specific gas constant (R) for exhaust products.

Chapter 5: Application and Evaluation of the 0D Thermodynamic Model for Hydrogen Combustion

- Adaptation of the 0D model for a hydrogen-fuelled engine.
- Configuration and validation against a baseline experimental dataset, including Wiebe parameter tuning.
- Comparative analysis of the four heat transfer correlations against experimental targets to identify the most suitable model (Woschni) for this hydrogen case.
- Evaluation of the model's predictive capability against three additional experimental datasets under varying operating conditions.
- Sensitivity analysis of the hydrogen simulation to variations in Wiebe combustion parameters (θ_s, θ_d, a, n).
- Qualitative comparative analysis of simulated diesel versus hydrogen combustion characteristics.

Chapter 6: Discussion, Conclusions, and Future Work

- Critical discussion of key findings, model capabilities, and inherent limitations for both diesel and hydrogen simulations.
- Analysis of the impact and sensitivity of different sub-models (combustion, heat transfer, gas properties).
- Summary of the main conclusions drawn from the validation exercises and comparative fuel analyses.
- Recommendations for future research, including dedicated experimental validation, advanced thermodynamic property modelling, and full-cycle simulation.

2

Internal Combustion Engines and Heat Transfer Modelling

This chapter presents the essential details needed to understand the thermodynamic simulations of a compression ignition direct injection (CIDI) engine. The basic operation of a four-stroke CIDI engine is explained at the beginning. The reasoning behind concentrating the simulation on the closed part of the engine cycle (compression and expansion strokes) is then explained. The chapter then explains the topic of in-cylinder heat transfer and discusses its significance in engine performance by introducing the common theoretical and empirical approaches used to model it. This establishes the basis for the specific heat transfer correlations and thermodynamic equations used in this study.

2.1. Working Principle of a 4-Stroke Compression Ignition Direct Injection (CIDI) Engine

Compression Ignition Direct Injection (CIDI) engines are a type of internal combustion engine (ICE) that uses high air compression to drive combustion, converting the chemical energy of fuel into mechanical work. Four piston strokes are used in this process, and each one is timed for effective power delivery (Figure 2.1). The cylinder heads, which have intake and exhaust valves for controlling gas flow, seal the cylinders in which the pistons move.

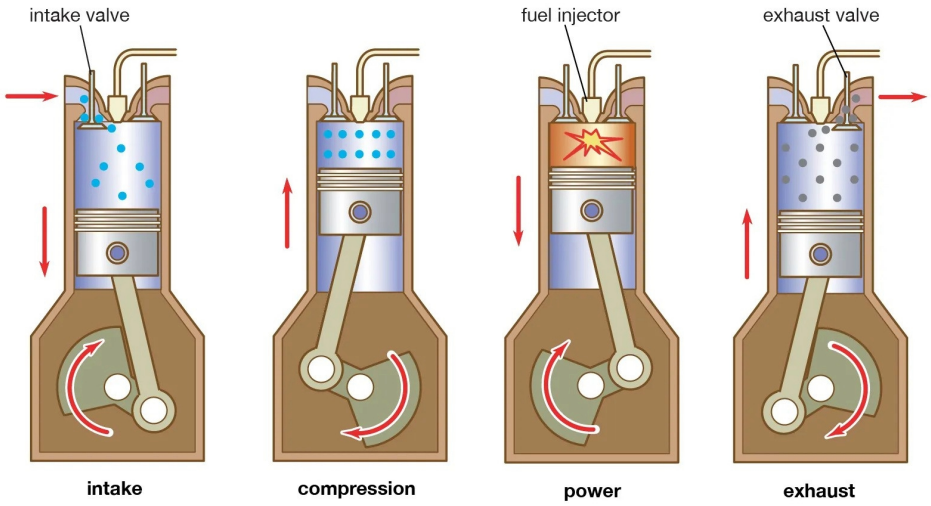

Figure 2.1: Illustration of 4-Strokes of a Compression Ignition Diesel Engine [8]

In direct injection (DI) engines, fuel is injected at high pressure directly into the combustion chamber via an injector in the cylinder head, ensuring good air-fuel mixing. The piston's downward power stroke is converted to rotational energy by the connecting rod and crankshaft, which then drives external systems. The synchronised movement of these parts enables the engine's energy conversion and determines its efficiency [9]. Figure 2.2 illustrates a diesel piston assembly.

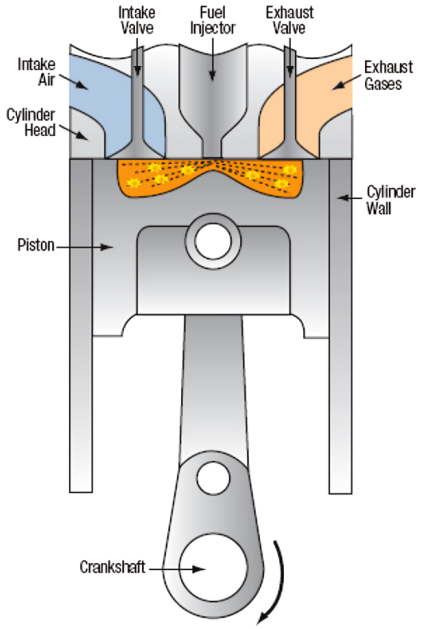

Figure 2.2: Piston and Cylinder Assembly for Direct Injection Diesel Engines [10]

The 4-stroke engine cycle comprises the following stages [9, 11]:

1. **Intake Stroke:** The piston moves from Top Dead Centre (TDC) to Bottom Dead Centre (BDC), drawing a fresh air charge into the cylinder via the intake system. The volume of air inducted is key to the engine's power capability.
2. **Compression Stroke:** The piston ascends with the cylinder sealed, compressing the trapped air. High compression ratios in CI engines (e.g., 14:1 to >28:1) heat this air above the fuel's auto-ignition temperature. Fuel is injected directly into this hot, compressed air near TDC.
3. **Power Stroke (Expansion):** Near TDC, injected fuel auto-ignites in the hot, compressed air. The rapid combustion generates high-pressure gases that force the piston downwards, producing mechanical work at the crankshaft.
4. **Exhaust Stroke:** As the piston moves up from BDC, the exhaust system allows the spent combustion products to be released from the cylinder, preparing it for the next cycle.

2.2. Rationale for Modelling the Closed Cycle: Compression and Expansion Strokes

This study's zero-dimensional (0D) thermodynamic model focuses on the internal combustion engine's compression and expansion strokes. This approach was chosen for several important reasons:

- The compression and expansion strokes are important from a thermodynamic perspective. It is during these phases that the in-cylinder working fluid undergoes significant changes in pressure, temperature, and volume. These changes directly govern the combustion process, the conversion of thermal energy into mechanical work, and eventually affect, the engine's overall efficiency. Capturing these phenomena accurately is thus of importance.

- Repetitive simulations are used to test sensitivity, adjust parameters, and compare engine models with experiments. Each simulation would run much faster when the computations are limited to the compression and expansion strokes instead of the entire cycle. This enables faster improvements and more comprehensive testing in this study.
- Many 0D engine cycle simulations that are present in literature also concentrate on the compression and expansion strokes. This method provides a method to study the main energy conversion steps effectively while keeping the model's complexity and computing needs reasonable.

Thus, focusing the model on these key compression and expansion strokes (as a closed system) strikes a balance between accurately predicting important thermodynamic events and keeping the model development practical and efficient.

2.3. Thermodynamics and Heat Transfer Modelling of the Engine

Heat loss plays a significant role in the performance of internal combustion engines. It affects the engine's efficiency, power output, in-cylinder pressure, emissions, fuel consumption, and heat transfer cooling characteristics [12], [13], [14], [15]. Therefore, analysing the heat transfer to the combustion chamber walls is crucial for engine development, particularly in areas such as the reliability of engine parts under thermal stresses and thermodynamic cycles.

Over the years, a large contribution has been made by researchers to perform numerical simulations to predict convective heat transfer, heat release rate, heat flux and combustion properties [16], [17]. Rakopoulos et al. [18], for example, examined the behaviour of the Heat Transfer Coefficient (HTC) in an air-cooled DI diesel engine and showed that load and engine speed both significantly affect in-cylinder heat transfer rates. Likewise, Trujillo et al. [14] used a single-cylinder air-cooled engine and a combination of simulations and experiments to assess cylinder temperatures under a range of loads. They concluded that convective HTC, heat flux, and cylinder temperature are important indicators for determining heat loss.

Research has also focused on comparing the predictive capabilities of different heat transfer models. Said et al. [19] assessed the Assanis, Hohenberg, Sitkei & Ramaniah, and Woschni correlations in a CI engine. By highlighting the significance of geometric and boundary layer considerations, they found that the Woschni model, which takes engine bore into account, performed best against experimental data and that its accuracy could be improved by modifying its velocity and temperature terms. In a separate study, Bobi and Laoonual [20] looked at the Hohenberg and Woschni models in a CI engine. Their findings show how sensitive heat transfer is to operating parameters, with Woschni consistently predicting higher convective HTC values than Hohenberg, especially in high-pressure, high-speed scenarios. While these studies provide a valuable baseline for diesel engines, applying these same models to alternative fuels like hydrogen presents significant challenges.

Specifically, the heat transfer mechanisms in hydrogen engines are known to be fundamentally different from those in hydrocarbon-fuelled engines. Hydrogen's distinct thermophysical properties, such as its high thermal conductivity and low quenching distance, result in unique in-cylinder thermal behaviour [21, 22]. A computational study by Babayev et al. [23] demonstrated that even with lower near-wall gas temperatures, hydrogen's convective heat transfer coefficient can be more than 50% higher than diesel's. This was largely attributed to hydrogen's thermal conductivity, which is approximately seven times that of the nitrogen that dominates diesel exhaust products. This finding suggests thermophysical properties can be a more dominant factor than temperature alone. Further, experimental work by Demuynck et al. [24] demonstrated that although heat loss in extremely lean hydrogen mixtures is similar to that of petrol, it rises sharply for richer mixtures, which has an adverse impact on efficiency. Early work by Shudo and Suzuki [25] established that conventional models are inadequate for hydrogen engines because they significantly underestimate the cooling loss, a discrepancy attributed to hydrogen's high flame propagation velocity.

A direct consequence is that heat transfer models developed for conventional fuels have been shown to be inaccurate when applied to hydrogen engines. Studies by Michl et al. [21] and Demuynck et al. [24] concluded that the existing work fails to satisfactorily predict measured heat fluxes in hydrogen engines. This has prompted researchers to either propose new phenomenological models tailored for hydrogen [21] or to modify existing equations to better capture the observed behaviour [22]. For hydrogen-enriched natural gas (HCNG) blends, the standard Woschni model has been shown to be a suitable choice, indicating that the heat transfer modelling problem is most acute for pure hydrogen applications [26]. This clearly indicates that there is not yet a universally accepted heat transfer model for hydrogen ICEs, and that the suitability of conventional models requires careful investigation.

In their research on heat transfer in internal combustion engines, Sharief and Chandrashekar [27] studied methods that estimate convective heat exchange using temperature, gas velocity, in-cylinder pressure, and an effective diameter. In particular, they pointed out that the accuracy of these heat transfer predictions is improved by including geometric details such as the cylinder bore and effective diameter.

The objective of this thesis is to develop a flexible, zero-dimensional (0D) thermodynamic simulation framework in MATLAB to systematically investigate these phenomena. The work begins by applying the framework to a single-cylinder, air-cooled diesel engine, using earlier literature studies as a foundation. In this initial phase, the model is validated, and the predictive capabilities of the common heat transfer correlations are evaluated in a conventional context. The validated framework is then adapted to simulate a hydrogen-fuelled engine, enabling a direct evaluation of the performance of the same established correlations in a hydrogen environment. This two-step approach is designed to contribute to the specific research gap identified in the literature concerning appropriate heat transfer models for hydrogen engines.

Zero-dimensional (0D) models are widely employed for analytical studies in internal combustion engine development due to their computational efficiency and relative simplicity in representing complex in-cylinder combustion events. As noted by Lounici et al. [28], engineers frequently find practical value in these 0D codes, especially when calibrated with experimental data from a specific engine, for design and development tasks. Such calibrated models can then be reasonably used to predict qualitative performance trends in new engines that share similar design features.

To calculate in-cylinder heat transfer, engine modelling commonly relies on established empirical correlations. Among the most frequently used are those developed by Woschni [29], Hohenberg [30], Sitkei [31], and Assanis [17]. For diesel Homogeneous Charge Compression Ignition (HCCI) engine simulations, and for many conventional spark-ignition engine models, this reliance on convective correlations is justified because forced convection is the principal mode of heat exchange between the in-cylinder gases and the combustion chamber walls. Consequently, thermal radiation effects are often considered secondary and are typically omitted to simplify the model without substantial loss of accuracy for overall heat transfer estimation.

2.4. Thermodynamic Equations

In this section, the various thermodynamic equations related to heat release and combustion have been discussed in detail.

2.4.1. First Law of Thermodynamics and Heat Release Rate

For the purpose of analysing heat release in the compression ignition engine, a closed-system approach based on the first law of thermodynamics is a suitable starting point [32]. Recognising that the combustion process occurs exclusively during valve closure and in the absence of blow-by, the engine cylinder during this phase can be effectively treated as a closed thermodynamic system. The first law, in this context, can be mathematically represented by the following equation:

For a finite process, the first law states that the change in internal energy (ΔU) of the system equals the net heat added to the system (Q_{net}) minus the net work done by the system (W_{net}):

$$\Delta U = Q_{net} - W_{net} \tag{2.1}$$

Here U is a state function (or property) of the system, while Q_{net} and W_{net} are path functions, representing energy transfer during a process. For an infinitesimal change, the first law is expressed in differential form:

$$dU = \delta Q_{net} - \delta W_{net} \tag{2.2}$$

where dU represents an exact differential of the internal energy. The terms δQ_{net} and δW_{net} denote inexact differentials, indicating that heat and work are path-dependent quantities.

In the context of engine analysis, it is often more convenient to define heat added to the system from combustion (Q_{hr}) and heat lost from the system to the walls (Q_{ht}) explicitly. Thus, δQ_{net} can be written as $\delta Q_{hr} - \delta Q_{ht}$. Substituting this and $\delta W_{net} = PdV$ (for quasi-static work done by the system) into Equation 2.2 gives:

$$dU = \delta Q_{hr} - \delta Q_{ht} - PdV \tag{2.3}$$

Rearranging to solve for the heat released by combustion, δQ_{hr}:

$$\delta Q_{hr} = dU + PdV + \delta Q_{ht} \tag{2.4}$$

According to Bobi et al. [20], Mauro et al. [33] and Ebrahimi [34], this basic relationship serves as the basis for calculating the rate of heat release. Factors such as the heating value of the fuel, the speed of the combustion reactions, and the in-cylinder temperature are all linked to the rate at which thermal energy is released during combustion.

2.4.2. Rate of Heat Release

To analyse processes with respect to time (t) or crank angle (θ), Equation 2.4 is expressed in terms of rates. The rate of heat release with respect to time is:

$$\frac{\delta Q_{hr}}{dt} = \frac{dU}{dt} + P\frac{dV}{dt} + \frac{\delta Q_{ht}}{dt} \tag{2.5}$$

In engine analysis, it is often more practical to express these rates with respect to crank angle θ. The relationship between time and crank angle derivatives is given by $\frac{d}{dt} = \frac{d}{d\theta}\frac{d\theta}{dt} = \omega\frac{d}{d\theta}$, where ω is the engine's angular speed (a function of engine speed N, $\omega = 2\pi N/60$). Applying this transformation, Equation 2.5 becomes:

$$\omega\frac{\delta Q_{hr}}{d\theta} = \omega\frac{dU}{d\theta} + P\left(\omega\frac{dV}{d\theta}\right) + \omega\frac{\delta Q_{ht}}{d\theta} \tag{2.6}$$

Dividing by ω (assuming $\omega \neq 0$) yields the heat release rate per unit crank angle:

$$\frac{\delta Q_{hr}}{d\theta} = \frac{dU}{d\theta} + P\frac{dV}{d\theta} + \frac{\delta Q_{ht}}{d\theta} \tag{2.7}$$

The terms in Equation 2.7 are:

- $\frac{\delta Q_{hr}}{d\theta}$: Rate of heat release from combustion per crank angle degree ($\mathrm{J}/°\mathrm{CA}$). This is often the primary quantity of interest derived from pressure analysis.
- $\frac{dU}{d\theta}$: Rate of change of internal energy of the in-cylinder gases per crank angle degree ($\mathrm{J}/°\mathrm{CA}$).
- $P\frac{dV}{d\theta}$: Rate of work done by the piston per crank angle degree ($\mathrm{J}/°\mathrm{CA}$).
- $\frac{\delta Q_{ht}}{d\theta}$: Rate of heat transfer from the gases to the cylinder walls per crank angle degree ($\mathrm{J}/°\mathrm{CA}$), representing heat loss.

2.4.3. Constitutive Relations and Derived Equations

To solve for the heat release rate and other thermodynamic variables, several constitutive relations and derived equations are employed.

Ideal Gas Law

The in-cylinder gases are typically modelled as an ideal gas, relating pressure (P), volume (V), mass (m), specific gas constant (R), and absolute temperature (T):

$$PV = mRT \tag{2.8}$$

All quantities (P, V, T) in this equation can be considered functions of crank angle, $P(\theta), V(\theta), T(\theta)$, while m and R are often assumed constant during the closed cycle.

Specific Heats and Their Ratio

The change in internal energy (dU) for an ideal gas is given by $dU = mc_v dT$, where c_v is the specific heat at constant volume (e.g., in $\mathrm{J\,kg^{-1}\,K^{-1}}$). The specific heat ratio, γ, is defined as:

$$\gamma = \frac{c_p}{c_v} \tag{2.9}$$

where c_p is the specific heat at constant pressure. For an ideal gas, the relationship $c_p - c_v = R$ holds. While γ inherently varies with temperature and gas composition (typically around 1.4 for air at standard conditions, decreasing to approximately 1.35 before injection and further to 1.26–1.3 post-combustion in CI engines [9]), this study's initial diesel simulations employed a constant $\gamma = 1.3$ for simplification. In refinements introduced to the model in Section 4.2, a temperature-dependent model for γ is implemented.

Using $dU = mc_v dT$ and $c_v = R/(\gamma - 1)$, the rate of change of internal energy with respect to crank angle can be expressed through the product rule for $d(PV)/d\theta$:

$$\frac{dU}{d\theta} = mc_v \frac{dT}{d\theta} = \frac{1}{\gamma - 1}\frac{d(PV)}{d\theta} = \frac{1}{\gamma - 1}\left(V\frac{dP}{d\theta} + P\frac{dV}{d\theta}\right) \tag{2.10}$$

Substituting this into the per-crank-angle form of the first law (Equation 2.7) yields the widely used equation for determining the apparent heat release rate ($\delta Q_{hr}/d\theta$) from pressure data [11, 20]:

$$\frac{\delta Q_{hr}}{d\theta} = \frac{\gamma}{\gamma - 1}P\frac{dV}{d\theta} + \frac{1}{\gamma - 1}V\frac{dP}{d\theta} + \frac{\delta Q_{ht}}{d\theta} \tag{2.11}$$

Pressure Gradient Equation

For cycle simulations where the heat release rate is a prescribed input (e.g., from a Wiebe function), Equation 2.11 is rearranged to solve for the instantaneous pressure gradient, $dP/d\theta$:

$$\frac{dP}{d\theta} = -\gamma\frac{P}{V}\frac{dV}{d\theta} + \frac{\gamma - 1}{V}\left(\frac{\delta Q_{hr}}{d\theta} - \frac{\delta Q_{ht}}{d\theta}\right) \tag{2.12}$$

Heat Loss Rate to Cylinder Walls

The rate of heat transfer from the in-cylinder gases to the combustion chamber walls, $\delta Q_{ht}/d\theta$, is modelled using convective heat transfer correlations.This equation is a specific application of Newton's Law of Cooling. The specific formulation used in this work, adapted from Ferguson and Kirkpatrick [11] for a normalized simulation approach, is:

$$\frac{\delta Q_{ht}}{d\theta} = h_{dim}\left[\frac{P_{norm}V_{norm}}{m_{norm}} - t_w\right]\frac{\pi}{180} \quad \text{(Normalized form)} \tag{2.13}$$

where the terms are:

- $P_{norm} = P/P_{BDC}$: Normalized pressure.
- $V_{norm} = V/V_{BDC}$: Normalized volume.
- $m_{norm} = m/m_{BDC}$: Normalized mass (typically 1 for a closed cycle).
- $P_{norm}V_{norm}/m_{norm}$ is proportional to T_{gas}/T_{BDC}.
- $t_w = T_w/T_{BDC}$: Dimensionless cylinder wall temperature, where T_w is the assumed actual wall temperature and T_{BDC} is the gas temperature at Bottom Dead Centre.
- h_{dim}: Dimensionless heat transfer coefficient (detailed below).
- $\pi/180$: Conversion factor since the rates are considered per degree and h_{dim} is defined based on radian-based quantities.

Dimensionless Heat Transfer Coefficient
The dimensionless heat transfer coefficient, h_{dim}, as employed in Equation 2.13, is derived from empirical convective heat transfer correlations and engine parameters [11]:

$$h_{dim} = \frac{4h_c T_{BDC}}{\omega \beta b P_{BDC}} \tag{2.14}$$

The parameters in this definition are:

- h_c: Convective heat transfer coefficient ($\mathrm{W/m^2/K}$) obtained from an empirical model (e.g., Woschni, Hohenberg) (Section 2.6.2.
- T_{BDC}: Gas temperature at BDC (K).
- P_{BDC}: Gas pressure at BDC (Pa).
- ω: Engine angular speed ($\mathrm{rad\,s^{-1}}$).
- β: A dimensionless volume scaling factor related to engine geometry (Section 2.5).
- b: Cylinder bore (m).

Temperature Update
The instantaneous in-cylinder gas temperature, T, is calculated at each step using the ideal gas law (Equation 2.8). For simulation purposes using normalized variables, it can be expressed relative to BDC conditions:

$$T = T_{BDC} \frac{P_{norm}}{m_{norm}} V_{norm} \tag{2.15}$$

Prescribed Fuel Heat Release Rate
When using a phenomenological model like the Wiebe function to define the combustion process, the rate of heat release from the fuel, $\delta Q_{hr}/d\theta$, is given by:

$$\frac{\delta Q_{hr}}{d\theta} = Q_{in,norm} \frac{dx_b}{d\theta} \tag{2.16}$$

where:

- $Q_{in,norm}$: Total chemical energy effectively released per cycle from the fuel (J). This is a function of the mass flow rate of the fuel burnt and its Lower Heating Value (LHV) (Section 2.6.1).
- $dx_b/d\theta$: Derivative of the Wiebe mass fraction burnt function, $x_b(\theta)$, defining the normalized rate and profile of the heat release (Section 2.4.4).

2.4.4. Wiebe Combustion model

This study employs a single-zone thermodynamic model for the engine cylinder. This method assumes that the contents of the cylinder are a spatially uniform system, which means that characteristics such as composition, temperature, and pressure are presumed to be unchanged throughout the cylinder. Comparing this simplification to multi-dimensional approaches, the computational demands are greatly reduced.

Combustion within this single-zone model is described empirically using the Wiebe function. This well-established function provides a practical and computationally efficient way to simulate the overall heat release pattern typical of internal combustion engines, without needing to resolve complex, multi-dimensional flame physics [9].

The Wiebe function describes the fuel mass fraction burned, $x_b(\theta)$, as a function of crank angle, θ. It has a distinctive sigmoidal (S-shaped) curve that qualitatively reflects the three different stages of engine combustion: initial ignition delay, rapid main burning, and a final, slower completion stage. Results

(Section 3.3, Figure 3.6) show a representative Wiebe curve produced by this model. The standard mathematical form of the single Wiebe function is given by [9, 35]:

$$x_b(\theta) = 1 - \exp\left[-a\left(\frac{\theta - \theta_s}{\theta_d}\right)^n\right] \quad \text{for } \theta \geq \theta_s \tag{2.17}$$

For $\theta < \theta_s$, $x_b(\theta) = 0$. The derivative of the mass fraction burnt with respect to crank angle, $dx_b/d\theta$, is proportional to the rate of heat release:

$$\frac{dx_b(\theta)}{d\theta} = \frac{a \cdot n}{\theta_d}\left(\frac{\theta - \theta_s}{\theta_d}\right)^{n-1} \exp\left[-a\left(\frac{\theta - \theta_s}{\theta_d}\right)^n\right] \quad \text{for } \theta > \theta_s \tag{2.18}$$

For $\theta \leq \theta_s$, $dx_b(\theta)/d\theta = 0$.

The Wiebe function (Equations 2.17 and 2.18) is defined by five key parameters that shape the combustion profile:

- θ: Instantaneous crank angle (typically in °CA relative to TDC).
- θ_s: Start of combustion crank angle (°CA). This marks the crank angle at which the Wiebe function begins to predict heat release.
- θ_d: Combustion duration (°CA). This parameter defines the total crank angle interval over which the majority (e.g., 99% for typical 'a' values) of the fuel is considered to burn according to the Wiebe profile.
- a: Dimensionless Wiebe efficiency or completeness parameter. It influences how quickly the burn fraction x_b approaches unity. A common value is around 6.9 for which x_b reaches approximately 99.9% at $\theta = \theta_s + \theta_d$. The simulations use specific values different for diesel and hydrogen.
- n: Dimensionless Wiebe form or shape factor. This exponent primarily controls the shape of the heat release rate curve, influencing the timing and intensity of the peak rate within the combustion duration θ_d. Higher 'n' values tend to yield a faster, more concentrated heat release around the midpoint of θ_d.

Selection of Wiebe Function Parameters
Typical values found in engine modelling literature and specific studies were used for setting the Wiebe parameters for the simulations. In CI engines, for example, the start of combustion (θ_s) is typically set within 5 °CA to 20 °CA before TDC (BTDC); however, this is highly dependent on engine characteristics and injection timing [9, 36]. Based on the type of fuel and operating conditions, the combustion duration (θ_d) usually falls within 20 °CA to 40 °CA or more [9, 37, 17].

The Wiebe shape parameters 'a' and 'n' for the initial diesel simulations were informed by studies such as Loganathan et al. [35], who investigated optimal values for diesel engines. Their findings for neat diesel fuel included parameter sets such as ($a = 2.75, n = 2.5$) and ($a = 3.0, n = 1.777$) for different injection timings. For this thesis, specific values of $a = 2, n = 3$ were initially adopted for the diesel simulation, and $a = 4, n = 3$ for the hydrogen simulation, with θ_s and θ_d set as detailed in Sections 3, 4, and 5. These parameters were then subject to tuning to achieve good agreement with experimental data, as discussed in the validation sections.

2.5. Cylinder Geometry and Piston Kinematics

A precise definition of the engine's in-cylinder geometry and piston kinematics is necessary for accurate modelling of thermodynamic processes within the engine. This section describes the geometric parameters and kinematic relationships that form the foundation of the 0D simulation framework and determine the instantaneous cylinder volume and heat transfer surface area throughout the engine cycle.

Figure 2.3 illustrates the fundamental geometric parameters. Key terms include cylinder bore (B), stroke length (S), crank radius ($a = S/2$), connecting rod length (l), crank angle (θ from TDC), clearance volume (V_c), and displacement volume (V_d).

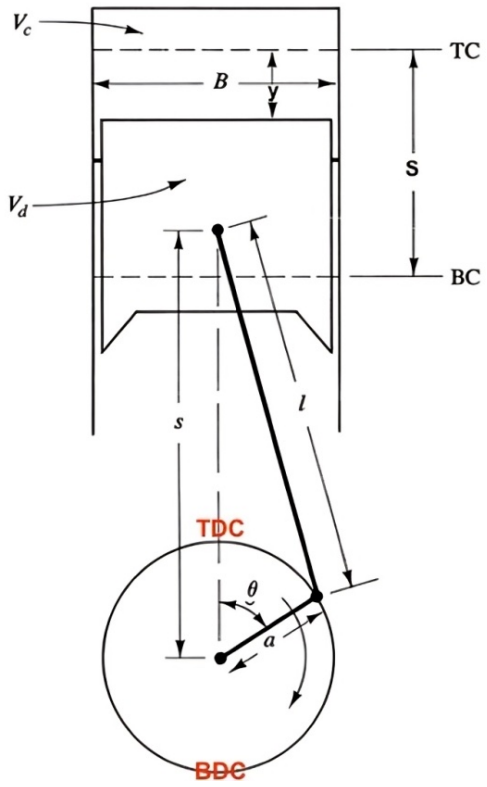

Figure 2.3: Key parameters of cylinder geometry and the crank-slider mechanism [9].

2.5.1. Fundamental Engine Parameters and Kinematic Equations

The following equations define essential engine parameters [9, 11].

Angular Speed (ω)

Crankshaft angular speed ω (in $\mathrm{rad\,s^{-1}}$) relates to engine speed N (in RPM) via:

$$\omega = \frac{2\pi N}{60} \tag{2.19}$$

Mean Piston Speed ($\bar{U}_p$)

The average speed of the piston, $\bar{U}_p$ (in $\mathrm{m\,s^{-1}}$), over a full cycle is given by:

$$\bar{U}_p = 2SN' \tag{2.20}$$

where N' is the engine speed in revolutions per second. If N is the engine speed in revolutions per minute (RPM), then $N' = N/60$, so $\bar{U}_p = 2SN/60 = SN/30$. Alternatively, using the crankshaft angular speed ω (in $\mathrm{rad\,s^{-1}}$, where $\omega = 2\pi N/60$), the mean piston speed can be expressed as:

$$\bar{U}_p = \frac{S\omega}{\pi} \tag{2.21}$$

The variable U (or U_p) used in subsequent heat transfer correlations within this study refers to this mean piston speed calculated using Equation 2.21.

Instantaneous Cylinder Volume ($V(\theta)$)

The volume $V(\theta)$ enclosed within the cylinder above the piston changes with crank angle θ. The exact formulation, derived from the geometry of the crank-slider mechanism, is given by [9]:

$$V(\theta) = V_c + \frac{\pi B^2}{4}\left(l + a - a\cos\theta - \sqrt{l^2 - (a\sin\theta)^2}\right) \tag{2.22}$$

where V_c is the clearance volume, B is the bore, l is the connecting rod length, and a is the crank radius. For many automotive engines, the ratio of connecting rod length to crank radius (l/a) is significantly greater than 1 (often $l/a > 3$). In such cases, the square root term $\sqrt{l^2 - (a\sin\theta)^2}$ can be simplified using a binomial expansion. By factoring out l^2 from under the square root, we get $l\sqrt{1 - (a/l)^2\sin^2\theta}$. Since $(a/l)^2\sin^2\theta$ is small when l/a is large, we can use the approximation $\sqrt{1-x} \approx 1 - x/2$ for small x. This leads to:

$$\sqrt{l^2 - (a\sin\theta)^2} \approx l\left(1 - \frac{1}{2}\left(\frac{a}{l}\right)^2\sin^2\theta\right) = l - \frac{a^2\sin^2\theta}{2l}$$

Substituting this approximation (Equation 2.5.1) back into the exact volume expression (Equation 2.22) yields a commonly used approximate formula for instantaneous cylinder volume:

$$V(\theta) \approx V_c + \frac{\pi B^2}{4}\left(a(1-\cos\theta) + \frac{a^2\sin^2\theta}{2l}\right)$$

Recognising that the displacement volume $V_d = (\pi B^2/4)S = (\pi B^2/4)(2a)$, Equation 2.5.1 can also be written as:

$$V(\theta) \approx V_c + \frac{V_d}{2}\left(1 - \cos\theta + \frac{a}{2l}\sin^2\theta\right) \tag{2.23}$$

This simplified form is often used in engine analyses for its reduced complexity, providing good accuracy when the l/a ratio is sufficiently large. However, for the simulations in this work, a formulation equivalent to the more exact kinematic expression (Equation 2.22) was retained to ensure higher accuracy in volume calculations.

Instantaneous Heat Transfer Surface Area ($A_s(\theta)$)
The instantaneous surface area $A_s(\theta)$ exposed to in-cylinder gases includes the cylinder head, piston crown, and the exposed portion of the cylinder wall. The specific formulation for $A_s(\theta)$ was implemented in this study's simulation. It is adapted from sources, including Sanli [38] and incorporates geometric terms:

$$A_s(\theta) = \frac{\pi B^2}{4} + \left(\frac{\pi B^2}{4} + \frac{4V_c}{B}\right) + \pi\frac{BS}{4}\left((R_c + 1 - \cos\theta) - \sqrt{R_c^2 - \sin^2\theta}\right) \tag{2.24}$$

In this equation:

- The first term, $\frac{\pi B^2}{4}$, represents the area of either the piston crown or the cylinder head (assuming flat surfaces).
- The second term, $\left(\frac{\pi B^2}{4} + \frac{4V_c}{B}\right)$, combines the area of the other end surface (head or piston) and the cylinder wall area exposed at TDC within the clearance height.
- The third term, $\pi\frac{BS}{4}\left((R_c + 1 - \cos\theta) - \sqrt{R_c^2 - \sin^2\theta}\right)$, accounts for the variation in the exposed cylinder liner area as the piston moves. Note that the kinematic part $(R_c + 1 - \cos\theta) - \sqrt{R_c^2 - \sin^2\theta}$ when multiplied by $S/2$ (or a) gives the instantaneous piston displacement from TDC. The $S/4$ factor here is specific to the implemented formulation.

Minimum Heat Transfer Surface Area at TDC (A_{TDC})
At TDC ($\theta = 0$), the minimum heat transfer surface area, A_{TDC}, comprises the sum of the cylinder head area, piston crown area, and the exposed cylinder wall within the clearance height:

$$A_{TDC} = 2 \cdot \frac{\pi B^2}{4} + \pi B y_{TDC} = \frac{\pi B^2}{2} + \frac{4V_c}{B} \tag{2.25}$$

Instantaneous Combustion Chamber Height ($y(\theta)$)
The instantaneous height $y(\theta)$ between a flat piston crown and a flat cylinder head is given by:

$$y(\theta) = y_{TDC} + a(1 - \cos\theta) + l\left(1 - \sqrt{1 - \left(\frac{a}{l}\sin\theta\right)^2}\right) \tag{2.26}$$

where y_{TDC} is the clearance height at TDC:

$$y_{TDC} = \frac{V_c}{\pi B^2/4} \tag{2.27}$$

Dimensionless Volume Parameter (β)
The dimensionless volume parameter β, utilised in certain heat transfer normalizations as per Ferguson and Kirkpatrick [11], is defined in this work as:

$$\beta = \frac{4V_{BDC}}{B\left(A_{TDC} - \frac{4V_c}{B}\right)} \tag{2.28}$$

Substituting Equation 2.25 into Equation 2.28 adds parameters of V_{BDC} (volume at BDC), B (bore), and A_{TDC} (area at TDC). The equation simplifies β to:

$$\beta = \frac{4V_{BDC}}{B\left(\frac{\pi B^2}{2}\right)} = \frac{8V_{BDC}}{\pi B^3} \tag{2.29}$$

2.6. Heat Transfer Analysis

This section details the approaches used to model the primary energy transfer phenomena within the engine cylinder during the closed portion of the cycle: the energy input from fuel combustion and the heat energy lost to the combustion chamber walls.

2.6.1. Modelling Energy Input: Combustion Heat Release

The energy released during combustion is the primary driver of the engine cycle. In this 0D simulation, this energy input is characterised first by determining the total energy available from the fuel and then by prescribing its release rate over crank angle using the Wiebe function.

Total Fuel Energy Input and Dimensionless Scaling
To quantify the energy input, the actual chemical energy available from the combusted fuel per cycle (Q_{in}) is first determined. For a given air mass flow rate ($\dot{m}_a$) and air-fuel ratio (AFR), the fuel mass flow rate ($\dot{m}_f$) is:

$$\dot{m}_f = \frac{\dot{m}_a}{\text{AFR}} \tag{2.30}$$

The fuel energy input per cycle (Q_{in}, in J) is then calculated using the fuel's Lower Heating Value (LHV) and the engine speed (N in RPM). For a four-stroke engine:

$$Q_{in} = \frac{\dot{m}_f \cdot \text{LHV}}{(N/2) \cdot 60} \tag{2.31}$$

For the simulation's normalized thermodynamic framework, particularly when the Wiebe function dictates a normalized heat release profile, this Q_{in} is often scaled by a reference energy, E_{ref}, typically defined by conditions at Bottom Dead Centre (BDC) [11]:

$$E_{ref} = P_{BDC} \cdot V_{BDC} \tag{2.32}$$

This yields a dimensionless total heat release parameter, $Q_{in,norm}$:

$$Q_{in,norm} = \frac{Q_{in}}{E_{ref}} \tag{2.33}$$

This $Q_{in,norm}$ then scales the Wiebe function's rate of burn ($dx_b/d\theta$) to ensure the total simulated energy release matches the actual fuel energy input, appropriately normalized. The specific Wiebe function formulation is detailed in Section 2.4.4.

2.6.2. Modelling Energy Loss: Convective Heat Transfer to Walls

In analysing in-cylinder processes of Compression Ignition (CI) engines, radiative heat transfer is often considered secondary to convection and is frequently neglected for simplification. The primary mechanism for heat exchange (or energy loss) between the hot combustion gases and the cylinder walls is thus modelled using a convective approach based on Newton's Law of Cooling. The instantaneous rate of convective heat transfer, $\dot{Q}_{ht}(\theta)$, can be expressed as: (The specific normalized form used in this study's simulations was presented in Equation 2.13) [9, 13, 39]:

$$\dot{Q}_{ht}(\theta) = h_c(\theta) A_s(\theta)(T_g(\theta) - T_w) \tag{2.34}$$

where the terms are defined as:

- $\dot{Q}_{ht}(\theta)$: Instantaneous convective heat transfer rate from the gas to the cylinder walls (typically in kW). This represents the thermal energy flow per unit time.
- h_c: Convective heat transfer coefficient (CHTC) ($\mathrm{W/m^2/K}$). This coefficient characterises the effectiveness of heat transfer and is a function of crank angle θ, typically determined by one of the empirical correlations discussed subsequently (e.g., Woschni, Hohenberg, Sitkei, or Assanis).
- A_s: Instantaneous heat transfer surface area ($\mathrm{m^2}$). This is the surface area of the combustion chamber (cylinder head, piston crown, and exposed cylinder liner) at crank angle θ (Section 2.5).
- T_g: Instantaneous mean bulk gas temperature within the cylinder (K).
- T_w: Mean effective cylinder wall temperature (K), generally assumed constant over the cycle for modelling purposes.

2.6.3. Empirical Heat Transfer Correlations

The convective heat transfer coefficient, $h_c(\theta)$, in Equation 2.34 is typically determined using empirical correlations. These correlations are generally based on dimensionless numbers, most notably the Nusselt number (Nu), Reynolds number (Re), and Prandtl number (Pr). A common general form for such correlations is:

$$Nu = C \cdot Re^m \cdot Pr^n \tag{2.35}$$

Where Nusselt number (Nu) represents the ratio of convective to conductive heat transfer across a boundary:

$$Nu = \frac{h_c L_{char}}{k_{gas}} \tag{2.36}$$

The Reynolds number (Re) indicates the ratio of inertial forces to viscous forces within the fluid and characterises the flow regime (e.g., laminar or turbulent):

$$Re = \frac{\rho_{gas} v_{char} L_{char}}{\mu_{gas}} \tag{2.37}$$

The Prandtl number (Pr) is the ratio of momentum diffusivity (kinematic viscosity) to thermal diffusivity:

$$Pr = \frac{\nu_{gas}}{\alpha_{gas}} = \frac{\mu_{gas}/\rho_{gas}}{k_{gas}/(\rho_{gas} c_{p,gas})} = \frac{\mu_{gas} c_{p,gas}}{k_{gas}} \tag{2.38}$$

Here, L_{char} is a characteristic length (often cylinder bore B), v_{char} is a characteristic gas velocity, k_{gas} is the thermal conductivity of the gas, ρ_{gas} is gas density, μ_{gas} is dynamic viscosity, and $c_{p,gas}$ is the specific heat at constant pressure of the gas. C, m, and n are empirical constants.

In many practical engine applications, the Prandtl number (Pr) exhibits relatively small variation over the typical operating range. Consequently, its effect is often implicitly incorporated into the constant C and the Reynolds number exponent m, simplifying the correlation.

The specific heat transfer correlations implemented in this model are Woschni [29], Hohenberg [30], Sitkei [31], and Assanis [17] (detailed in Section 2.6.4 to 2.6.7). These correlations are all based on such empirical approaches; each defines the characteristic velocity and length scales differently.

According to Lounici et al. [28], a significant difference is that the Woschni and Assanis correlations account for combustion-induced turbulence, whereas correlations such as Hohenberg's and Sitkei's frequently relate the characteristic gas velocity primarily to the mean piston speed (representing non-combustion conditions). In order to account for the increased gas motion during the combustion phase, they usually add a term that reflects the pressure differential between firing and motoring conditions to the mean piston speed term.

2.6.4. Woschni Heat Transfer Correlation

The Woschni correlation is a widely adopted empirical model for estimating the convective heat transfer coefficient, h_c (denoted h_w for Woschni), in internal combustion engines [29]. It is expressed as:

$$h_c = C_0 B^{-0.2} P^{0.8} T^{-0.55} w^{0.8} \tag{2.39}$$

where $C_0 = 3.26$ when using SI units with pressure P in kPa. The parameters are:

- h_c: Convective heat transfer coefficient ($\mathrm{W/m^2/K}$).
- B: Cylinder bore (m).
- P: Instantaneous in-cylinder gas pressure (kPa).
- T: Instantaneous mean bulk gas temperature (K).
- w: Characteristic average gas velocity within the cylinder ($\mathrm{m\,s^{-1}}$), detailed below.

A key feature of the Woschni correlation is its formulation for the characteristic gas velocity, w, which includes terms for both piston motion and combustion-induced turbulence:

$$w = C_1 \bar{U}_p + C_2 \frac{V_d T_{ref}}{P_{ref} V_{ref}} (P - P_{mot}) \tag{2.40}$$

The components of this velocity term are:

- $\bar{U}_p$: Mean piston speed ($\mathrm{m\,s^{-1}}$), (Section 2.5).
- C_1, C_2: Dimensionless constants dependent on the engine cycle phase:
  - Gas Exchange: $C_1 = 6.18$, $C_2 = 0$.
  - Compression Stroke: $C_1 = 2.28$, $C_2 = 0$.
  - Combustion & Expansion: $C_1 = 2.28$, $C_2 = 0.00324$ (for DI engines).
- V_d: Displacement volume ($\mathrm{m^3}$).
- $P_{ref}, V_{ref}, T_{ref}$: Pressure, volume, and temperature at a reference state (e.g., conditions at BDC).
- P: Instantaneous cylinder pressure during firing (kPa).
- P_{mot}: Motoring pressure at the same crank angle/volume (kPa).

For this study's closed-cycle model (compression and expansion), $C_1 = 2.28$ is used with $C_2 = 0.00324$ applied during the combustion and expansion phases, and $C_2 = 0$ during compression prior to significant combustion [20, 28].

2.6.5. Hohenberg Heat Transfer Correlation

Hohenberg [30] proposed an alternative correlation, aiming to address perceived inaccuracies in the Woschni model, particularly its tendency to underpredict heat transfer during compression and overpredict it during combustion. The Hohenberg correlation for h_c (denoted h_h) is:

$$h_c = C_H P^{0.8} V^{-0.06} T^{-0.4} (\bar{U}_p + C_k)^{0.8} \tag{2.41}$$

The empirical constant C_H depends on the units used for the variables. A commonly cited value is $C_H = 130$ when pressure P is in bar, instantaneous volume V is in m^3, temperature T is in K, and mean piston speed $\bar{U}_p$ is in $\mathrm{m\,s^{-1}}$, yielding h_c in $\mathrm{W/m^2/K}$. The implementation in this work utilises $C_H = 3.26$, with the understanding that P is then taken in kPa. The parameters in Equation 2.41 are:

- P: Instantaneous in-cylinder gas pressure (units depend on C_H; kPa for $C_H = 3.26$).
- V: Instantaneous cylinder volume (m^3).
- T: Instantaneous mean bulk gas temperature (K).
- $\bar{U}_p$: Mean piston speed ($\mathrm{m\,s^{-1}}$).
- C_k: A calibration constant, typically $1.4\,\mathrm{m\,s^{-1}}$ based on Hohenberg's findings, accounting for gas motions not solely dependent on mean piston speed.

2.6.6. Sitkei Heat Transfer Correlation

Sitkei [31] also developed an empirical correlation for h_c (denoted h_s for Sitkei) from diesel engine experiments. A common representation of the Sitkei correlation is:

$$h_c = C_S(1 + b_{st})P^{0.7}\bar{U}_p^{0.7}T^{-0.2}d_e^{-0.3} \tag{2.42}$$

The parameters, with P in kPa, T in K, and $\bar{U}_p$ in $\mathrm{m\,s^{-1}}$, are:

- C_S: An empirical constant (e.g., 0.04 as used in this study's implementation).
- b_{st}: A dimensionless tuning parameter for swirl or turbulence effects, typically ranging from 0 to 0.35. For direct injection (DI) engines, a value of 0.03 was selected for this work.
- d_e: Equivalent hydraulic diameter of the combustion chamber (m), calculated as $d_e = 4V/A_s$, where V is instantaneous volume and A_s is instantaneous heat transfer surface area.

2.6.7. Assanis Heat Transfer Correlation

The Assanis correlation [17] modifies Woschni's approach, notably by using the instantaneous combustion chamber height (y) as a characteristic length and altering the temperature exponent and the combustion-induced velocity term. The formula for h_c (denoted h_a for Assanis) is:

$$h_c = C_A \cdot y^{-0.2}P^{0.8}T^{-0.73}w_A^{0.8} \tag{2.43}$$

where $C_A = 3.4$. Parameters are:

- y: Instantaneous combustion chamber height (m) (Section 2.5).
- P, T: Instantaneous pressure (kPa) and temperature (K).
- w_A: Characteristic gas velocity for the Assanis model ($\mathrm{m\,s^{-1}}$), defined as:

$$w_A = C_1\bar{U}_p + \frac{C_2}{6}\frac{V_d T_{ref}}{P_{ref}V_{ref}}(P - P_{mot}) \tag{2.44}$$

The terms are analogous to Woschni's velocity (Equation 2.40), with $C_1 = 2.28$ and $C_2 = 0.00324$ being Woschni's constants for combustion/expansion. The $C_2/6$ factor reduces the impact of the combustion-induced velocity component.

3

0D Thermodynamic Simulation: Methodology and Application

This chapter comprehensively presents the zero-dimensional (0D) thermodynamic engine simulation developed for this research, detailing its methodology, structural organisation, and key features. The code is implemented in MATLAB, and it simulates the in-cylinder processes of a Compression Ignition (CI) engine by specifically concentrating on the compression and expansion strokes. An overview of the code's architecture, the numerical integration scheme employed (Euler forward method), and the core computational logic are presented. Furthermore, this chapter details the setup for the baseline diesel engine case, including engine specifications, simulation input parameters, modelling assumptions, and fuel-related calculations. The results obtained from these simulations, including comparisons of different heat transfer models, are presented and analysed in Section 3.3.

3.1. Simulation Methodology

3.1.1. Code Architecture

For clarity and modularity, the MATLAB simulation is organised around a primary coding function. Although the original framework was inspired by Ferguson and Kirkpatrick's [11] example code, the current code has been significantly expanded and modified with features and customised logic. This has enabled the creation of a simulation tool that is different from its original template and is appropriate for the goals of this study. The function's organisation comprises the following logical sections:

Parameter Definition:
This initial segment defines and initialises all input parameters crucial for the simulation, including Wiebe combustion settings, engine geometry, operating conditions, gas and fuel properties, heat transfer constants, and simulation controls. This allows for straightforward scenario adjustments.

Simulation Setup and Initialisation:
This section prepares the computational environment by establishing the crank angle domain, integration step size, pre-allocating data arrays for results, and setting initial values for state variables, ensuring a consistent starting point for calculations.

Core Computational Logic - Euler Forward Integration Loop:
The simulation's core is an iterative loop employing the Euler forward integration method, stepping through the compression and expansion strokes in discrete crank angle increments ($\Delta\theta$). All pertinent calculated values are stored at each crank angle. Within each step:

1. Instantaneous cylinder volume $V(\theta)$ and its rate of change $dV/d\theta$ are determined.
2. The rate of heat release from combustion, $\delta Q_{hr}(\theta)/d\theta$, is calculated via the Wiebe function.
3. In-cylinder gas temperature $T(\theta)$ is updated using the ideal gas law.

4. The rate of heat loss to cylinder walls, $\delta Q_{ht}(\theta)/d\theta$, is estimated using a selected heat transfer correlation.
5. The pressure gradient $dP/d\theta$ is computed from the first law of thermodynamics (Equation 2.12).
6. Cylinder pressure $P(\theta + \Delta\theta)$ for the next step is updated using the Euler forward method.
7. Incremental work done PdV, heat loss $\delta Q_{ht}(\theta)$, and internal energy change are tracked and accumulated.

Post-Integration Analysis and Output:
After the integration loop, this section calculates overall engine performance metrics (e.g., net work, efficiency), prints key indicators, and generates plots visualising in-cylinder pressure, temperature, and heat release characteristics, as discussed in Section 3.3.

3.1.2. Zero-Dimensional (0D) Approach and Numerical Integration:

The Euler forward integration scheme is used to numerically solve the governing ordinary differential equation for pressure (Equation 2.12) and other integrated state variables, such as heat release ($Q_h r$), internal energy (U), cumulative work (W) and heat loss ($Q_h t$). This approach is first-order and explicit. The Euler forward method approximates Y at the next step, $\theta_{i+1} = \theta_i + \Delta\theta$, for a general ordinary differential equation $\frac{dY}{d\theta} = f(Y, \theta)$ with an initial condition $Y(\theta_i) = Y_i$:

$$Y_{i+1} \approx Y_i + f(Y_i, \theta_i) \cdot \Delta\theta \tag{3.1}$$

The Euler forward method was selected primarily for its straightforward implementation and computational efficiency per step due to its non-iterative nature. However, since this method is first-order accurate, this requires small step sizes ($\Delta\theta$) for reasonable precision and to maintain numerical stability, as it is only conditionally stable and prone to error accumulation [40].

3.2. Baseline Diesel Engine Simulation: Setup and Parameters

This section details the configuration of the 0D simulation for the baseline diesel engine case, outlining target engine specifications, key input parameters, modelling assumptions, and derived properties.

3.2.1. Target Engine: Hatz 1D90E Specifications

The 0D thermodynamic model is parameterized based on the Hatz 1D90E single-cylinder, air-cooled, direct-injection diesel engine, compliant with EU Stage V emissions standards. Table 3.1 summarises data obtained from manufacturer documentation [41, 42].

Table 3.1: Hatz 1D90E Engine Specifications [41, 42]

Property	Value	Unit
Engine Type	Single Cylinder, 4-Stroke Diesel	
Cooling System	Air-Cooled	
Injection System	Direct Injection	
Aspiration	Naturally Aspirated	
Displacement (V_d)	0.722	L ($0.000\,722\,\mathrm{m}^3$)
Bore (B)	0.104	m
Stroke (S)	0.085	m
Compression Ratio (r)	21.5	–
Rated Power (P_b)	11.2	kW
Rated Speed (N)	3000	RPM
Air Mass Flow Rate ($\dot{m}_a$)	79.5	$\mathrm{kg\,h^{-1}}$
Emissions Control	Diesel Particulate Filter	

3.2.2. Simulation Input Parameters and Modelling Assumptions (Diesel Baseline)

Based on Hatz 1D90E specifications and typical CI engine characteristics, Table 3.2 lists the input parameters and assumptions for the baseline diesel simulation. These values reflect engine data, literature-based assumptions, or preliminary calculations (e.g., AFR justification in Section 3.2.5).

Table 3.2: Input Parameters and Assumptions for Baseline Diesel Simulation

Parameter	Symbol	Value	Unit/Note
Operating Conditions			
Engine Speed	N	3000	RPM
Air Mass Flow Rate	$\dot{m}_a$	79.5	$\mathrm{kg\,h^{-1}}$
Air-Fuel Ratio	AFR	26.6	– (Lean Ratio, See Section 3.2.5)
Initial Thermodynamic State *(BDC, start of compression)*			
Pressure at BDC	P_{BDC}	$100\,\mathrm{kPa}$	Assumed (Naturally-Aspirated Engine)
Temperature at BDC	T_{BDC}	$300\,\mathrm{K}$	Assumed (Naturally-Aspirated Engine)
Wiebe Combustion Model Parameters			
Start of Combustion	θ_s	-9	°CA (Literature-informed)
Combustion Duration	θ_d	40	°CA (Literature-informed)
Wiebe Factor	a	2	Dimensionless (Literature-informed)
Wiebe Exponent	n	3	Dimensionless (Literature-informed)
Thermal and Gas Properties			
Specific Heat Ratio	γ	1.3	Constant, assumed
Specific Gas Constant	R_1	$0.2869\,\mathrm{kJ\,kg^{-1}\,K^{-1}}$	Assumed (Air/Lean Products)
Specific Heat at c_p	c_p	$1.2436\,\mathrm{kJ\,kg^{-1}\,K^{-1}}$	Derived from γ, R_1 (See Appendix B)
Specific Heat at c_v	c_v	$0.9563\,\mathrm{kJ\,kg^{-1}\,K^{-1}}$	Derived from γ, R_1 (See Appendix B)
Effective Wall Temp.	T_w	$500\,\mathrm{K}$	Assumed ($t_w \approx 1.67$, Sec. 3.2.3)
Fuel LHV (Diesel)	LHV	$44.8 \times 10^6\,\mathrm{J\,kg^{-1}}$	Standard value
Fuel Energy Input	Q_{in}	$1487.72\,\mathrm{J}$	Calculated Using Equation 2.31
Initial Air Density	$\rho_{air,BDC}$	$1.1618\,\mathrm{kg\,m^{-3}}$	Derived from P_{BDC}, T_{BDC}, R_1

Wiebe parameters θ_s, θ_d, a, n were selected based on typical diesel CI ranges (as discussed in Section 2.4.4 [9, 35] and evaluated during model validation (Chapter 4). The use of a constant γ is a noted simplification.

3.2.3. Wall Temperature Selection

Many researchers have experimented with choosing different values of the mean cylinder wall temperature T_w. It is not a fixed constant but rather a parameter that is inherently influenced by a multitude of factors. These influencing factors include the combustion temperature itself, the coolant temperature circulating through the engine block, the thermal properties of the combustion chamber wall materials, the inlet air temperature, the fuel-air equivalence ratio, as well as engine operating conditions such as engine speed and load [20].

From literature it was found that there are various values being employed for the wall temperature values of engines. Zak et al. [15] utilised distinct wall temperatures of 410K and 480K. Further, Bobi et al. [20] used a value of 450K. Stone [43], in his study, used a value of 350K for the wall temperature. Determining a representative average cylinder wall temperature (T_w) for 0D simulations is hence challenging. A sensitivity analysis was performed to determine a suitable wall temperature. Simplified conduction estimates showed that varying wall material (e.g., aluminium k $\approx 160\,\mathrm{W\,m^{-1}\,K^{-1}}$ vs. cast iron k $\approx 50\,\mathrm{W\,m^{-1}\,K^{-1}}$) or thickness (e.g., $7\,\mathrm{mm}$ to $65\,\mathrm{mm}$) could alter calculated inner surface temperatures by tens of Kelvins around a baseline condition.

Using the Woschni correlation as an example, full cycle simulations were run with assumed average T_w from $350\,\mathrm{K}$ to $600\,\mathrm{K}$. Results (Table 3.3) indicated that total heat loss decreased (from $182\,\mathrm{J}$ to $129\,\mathrm{J}$), while work and efficiency marginally increased with higher T_w. Given the relatively small impact on overall cycle metrics across this range, $500\,\mathrm{K}$ was chosen as a representative wall temperature for detailed simulations.

Table 3.3: Effect of Assumed Average Wall Temperature (T_{wall}) on Key Engine Performance Metrics.

Parameter	$T_w = 350.00\,\mathrm{K}$	$T_w = 400.00\,\mathrm{K}$	$T_w = 450.00\,\mathrm{K}$	$T_w = 500.00\,\mathrm{K}$	$T_w = 600.00\,\mathrm{K}$
Heat Loss (J)	182.14	171.62	161.03	150.35	128.75
Work (J)	737.42	740.52	743.66	746.83	753.29
Efficiency (%)	49.57	49.78	49.99	50.20	50.63
Max Pressure (MPa)	6.62	6.64	6.67	6.71	6.76
Ind. Power (kW)	12.43	12.51	12.59	12.72	12.83

3.2.4. Convergence Study for Integration Step Size

The accuracy and stability of the Euler forward integration method are highly dependent on the chosen integration step size, $\Delta\theta$. To determine an appropriate step size that balances numerical accuracy with computational efficiency, a convergence study was conducted. This study utilised the Woschni heat transfer correlation as an example to assess convergence, as the underlying numerical integration behaviour is generally independent of the specific HTC model once a stable regime is reached. Starting with a relatively coarse step size of $\Delta\theta = 1\,^\circ$CA, simulations were performed with progressively halved step sizes down to $0.003\,91\,^\circ$CA. The effect of changing $\Delta\theta$ on the main simulation results of indicated thermal efficiency ($\eta_{th,i}$), peak in-cylinder temperature (T_{max}), and peak in-cylinder pressure (P_{max}) was tracked.

Figures 3.1, 3.2, and 3.3 illustrate the convergence behaviour of these parameters as the crank angle step size (plotted on a logarithmic scale) is refined.

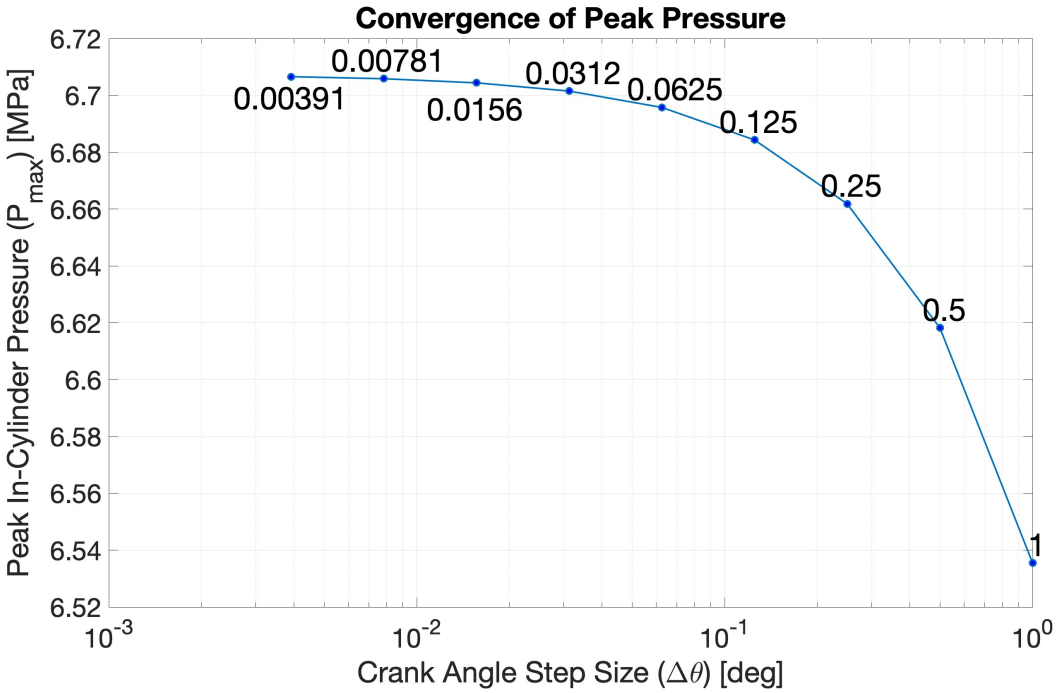

Figure 3.1: Convergence of Peak In-Cylinder Pressure (P_{max}) with decreasing crank angle step size ($\Delta\theta$).

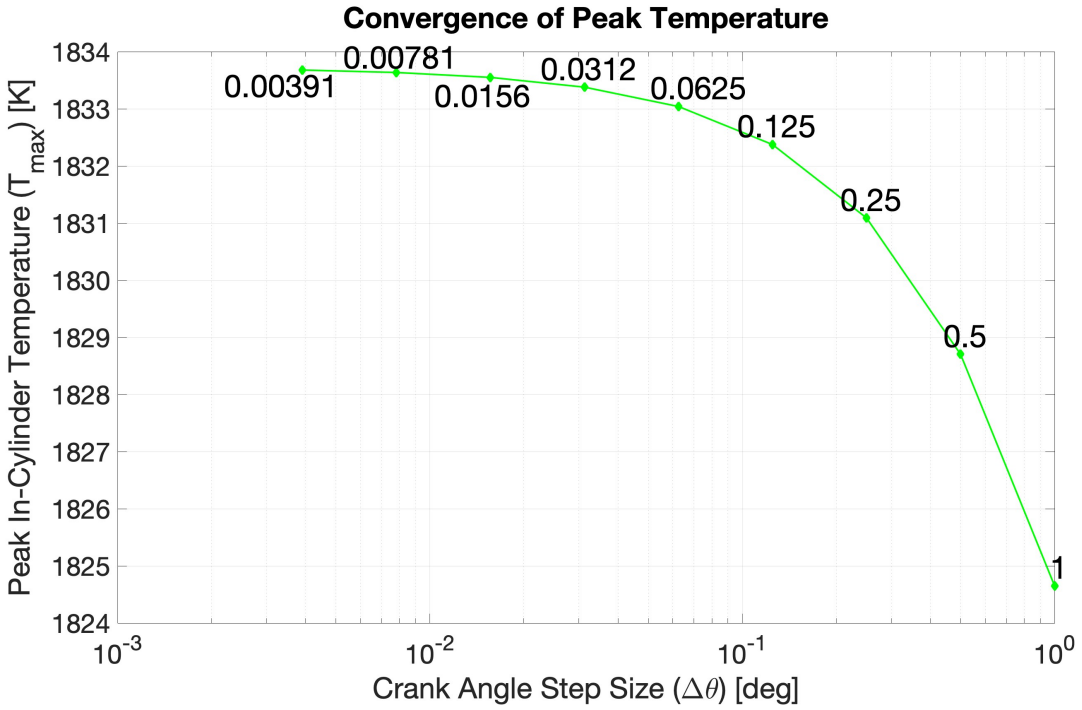

Figure 3.2: Convergence of Peak In-Cylinder Temperature (T_{max}) with decreasing crank angle step size ($\Delta\theta$).

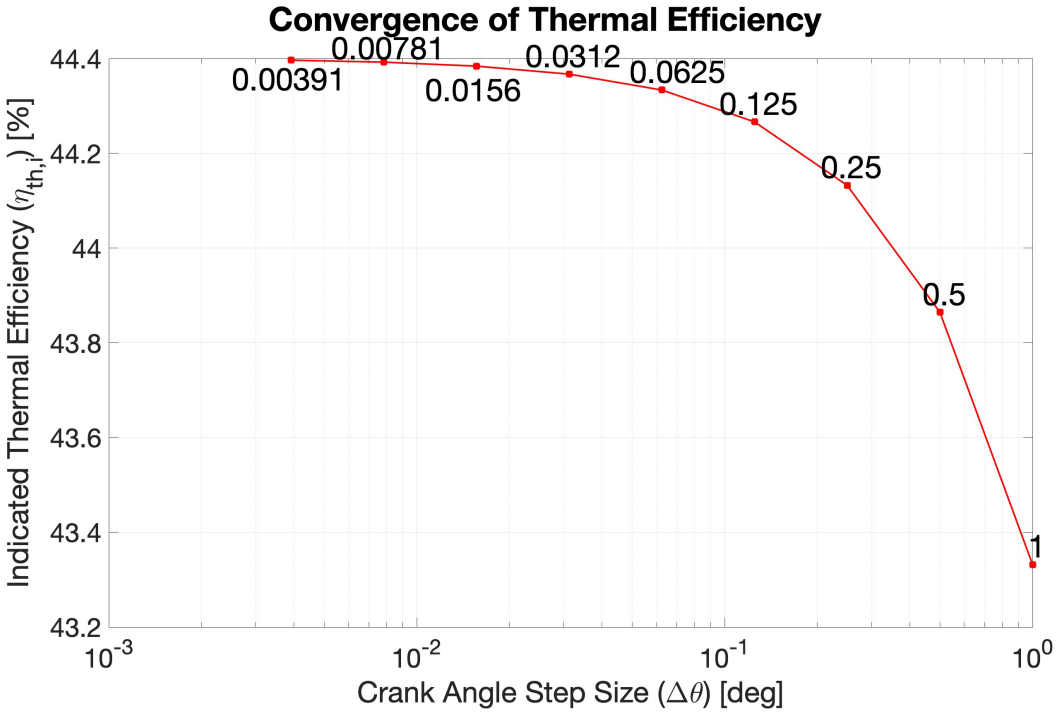

Figure 3.3: Convergence of Indicated Thermal Efficiency ($\eta_{th,i}$) with decreasing crank angle step size ($\Delta\theta$).

As evident from these figures, all three monitored parameters exhibit significant changes with larger step sizes (e.g., $\Delta\theta = 1\,°$CA or $0.5\,°$CA). As $\Delta\theta$ is reduced, the predicted values begin to stabilise. Peak pressure (Figure 3.1) converges towards approximately $6.71\,\mathrm{MPa}$ as $\Delta\theta$ approaches smaller values. Similarly, peak temperature (Figure 3.2) stabilises near $1833.8\,\mathrm{K}$, and indicated thermal efficiency (Figure 3.3) approaches $44.38\,\%$.

The plots demonstrate that reducing the step size from $0.0156\,°$CA to $0.007\,81\,°$CA, and further to $0.003\,91\,°$CA, results in increasingly smaller changes to these key output metrics. For instance, the difference in predicted peak pressure between $\Delta\theta = 0.007\,81\,°$CA and $\Delta\theta = 0.003\,91\,°$CA is minimal. Based on this observed convergence behaviour, a crank angle step size of $\Delta\theta = 0.007\,812\,5\,°$CA was selected for the final simulations presented in this thesis. Further reductions in step size yielded negligible improvements in the primary outputs at the cost of significantly increased simulation duration.

3.2.5. Determination of Air-Fuel Ratio

The simulation for the diesel engine case operates with an Air-Fuel Ratio (AFR) of 26.6. This value represents a lean mixture compared to the stoichiometric AFR for diesel (approximately 14.5). This value was determined by targeting a typical brake thermal efficiency (η_{bth}) for diesel engines at their rated power output.

Given a representative brake thermal efficiency of around $30\,\%$ for such engines, the engine's rated power ($P_b = 11.2\,\mathrm{kW}$), and the Lower Heating Value (LHV) of diesel ($h_L = 44.8 \times 10^6\,\mathrm{J\,kg^{-1}}$), an estimated fuel mass flow rate ($\dot{m}_f$) required to produce this power can be calculated:

$$\dot{m}_f = \frac{P_b}{\eta_{bth} \cdot h_L} = \frac{11.2 \times 10^3\,\mathrm{W}}{0.3 \cdot 44.8 \times 10^6\,\mathrm{J\,kg^{-1}}} \approx 0.833 \times 10^{-3}\,\mathrm{kg\,s^{-1}} \approx 2.99\,\mathrm{kg\,h^{-1}} \tag{3.2}$$

Using the specified air mass flow rate for the engine ($\dot{m}_a = 79.5\,\mathrm{kg\,h^{-1}}$), the resulting AFR is:

$$\mathrm{AFR} = \frac{\dot{m}_a}{\dot{m}_f} = \frac{79.5\,\mathrm{kg\,h^{-1}}}{2.99\,\mathrm{kg\,h^{-1}}} \approx 26.6 \tag{3.3}$$

3.2.6. Estimation of Combustion Product Composition

To approximate the average properties of the combustion products, such as the mixture-specific gas constant (R_{mix}) used in thermodynamic calculations (detailed in Section 4.2.3), an analysis of diesel fuel combustion with excess air was performed. For this calculation, diesel fuel was approximated as dodecane ($C_{12}H_{23}$), and the simulation's lean Air-Fuel Ratio (AFR) of 26.6 was used.

The methodology involved first balancing the stoichiometric combustion equation for diesel with air. The amount of excess air was then calculated using the air-fuel equivalency ratio ($\lambda \approx 1.834$ for AFR = 26.6). The lean combustion equation was then formulated by accounting for this excess air. The main products were identified as carbon dioxide (CO_2), water vapour (H_2O), unreacted (excess) oxygen (O_2), and nitrogen (N_2)

From the balanced lean combustion equation, the molar and mass percentages of these products were determined. The detailed balancing steps and percentage calculations are provided in Section B.2 of Appendix B. The estimated molar composition of the products is approximately: $CO_2 \approx 7.47\%$, $H_2O \approx 7.16\%$, $O_2 \approx 9.21\%$, and $N_2 \approx 76.16\%$. This composition, which is characterised by significant excess oxygen, forms the basis for calculating properties like the average molar mass of the mixture and the specific gas constant for the combustion products.

3.3. Baseline Diesel Simulation: In-Cylinder Characteristics and Performance

This section presents key results from the zero-dimensional (0D) thermodynamic simulation of the baseline diesel engine case, configured as detailed in Section 3.2. The analysis begins with fundamental kinematic and prescribed combustion profiles, followed by an examination of in-cylinder thermodynamic parameters and heat transfer characteristics, highlighting the influence of different empirical heat transfer correlations.

3.3.1. Engine Kinematics and Prescribed Combustion Profile

These are fundamental geometric and combustion characteristics of the diesel simulation:

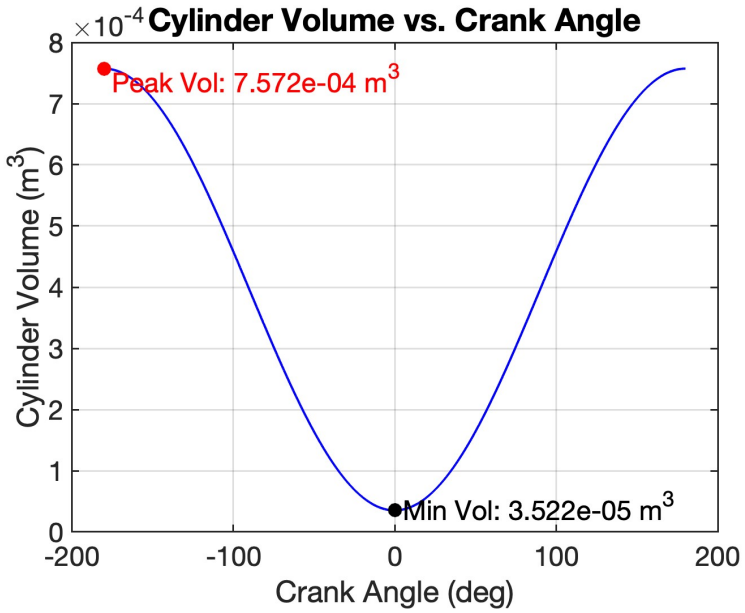

Figure 3.4: Simulated Cylinder Volume as a Function of Crank Angle.

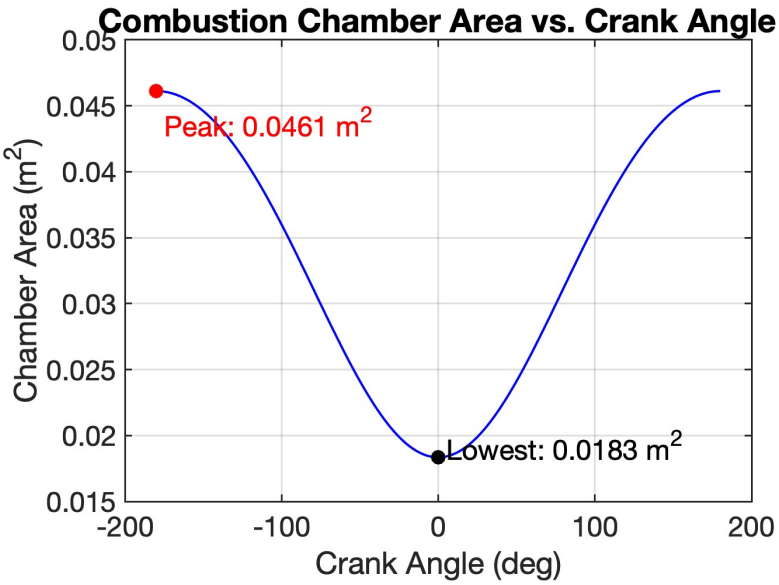

Figure 3.5: Simulated Combustion Chamber Surface Area vs. Crank Angle.

Figure 3.4 illustrates the variation of cylinder volume with crank angle. This profile is periodic and exhibits a characteristic U-shape, though it is not a pure sinusoid due to the finite length of the connecting rod. The volume ranges from its minimum (clearance volume, $V_c \approx 3.52 \times 10^{-5}\,\mathrm{m}^3$) at Top Dead Centre (TDC, $0\,^\circ$CA) to its maximum ($V_{BDC} \approx 7.57 \times 10^{-4}\,\mathrm{m}^3$) at Bottom Dead Centre (BDC, $\pm 180\,^\circ$CA). Similarly, Figure 3.5 shows the corresponding change in the instantaneous combustion chamber surface area available for heat transfer, which also varies with a U-shaped profile from a minimum of approximately $0.0183\,\mathrm{m}^2$ at TDC to a maximum of $0.0461\,\mathrm{m}^2$ at BDC.

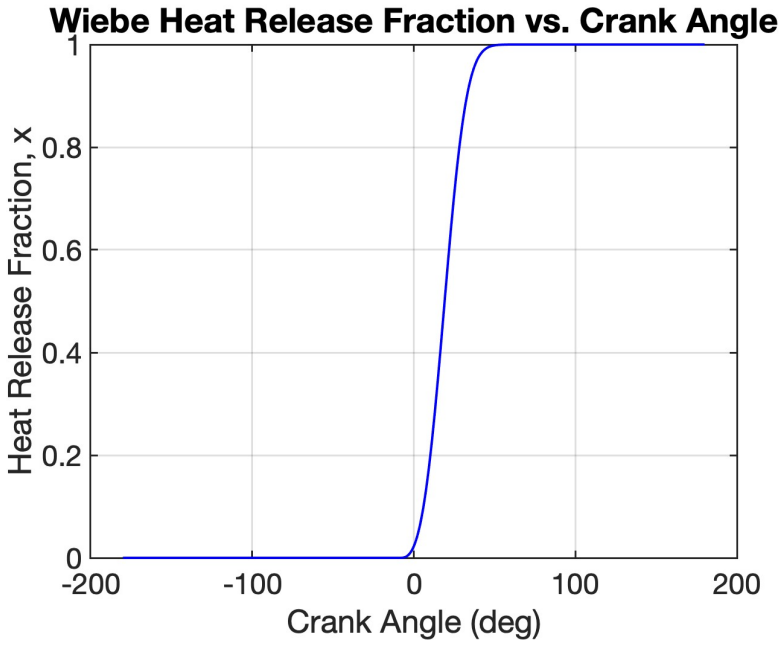

Figure 3.6: Prescribed Wiebe Heat Release Fraction (x_b) vs. Crank Angle.

The Wiebe function is used to model the combustion process. As shown in Figure 3.6, the prescribed mass fraction burnt (x_b) profile starts at the specified start of combustion ($\theta_s = -9\,°$CA) and progresses to near completion within the specified duration ($\theta_d = 40\,°$CA). The simulation's overall energy release pattern and timing are determined by this S-shaped curve.

3.3.2. First-Law Derived Heat Release Characteristics (Hohenberg Model)

The following heat release characteristics are derived from the first law of thermodynamics (Equation 2.11), using the simulated pressure trace obtained with the Hohenberg heat transfer correlation as an illustrative example.

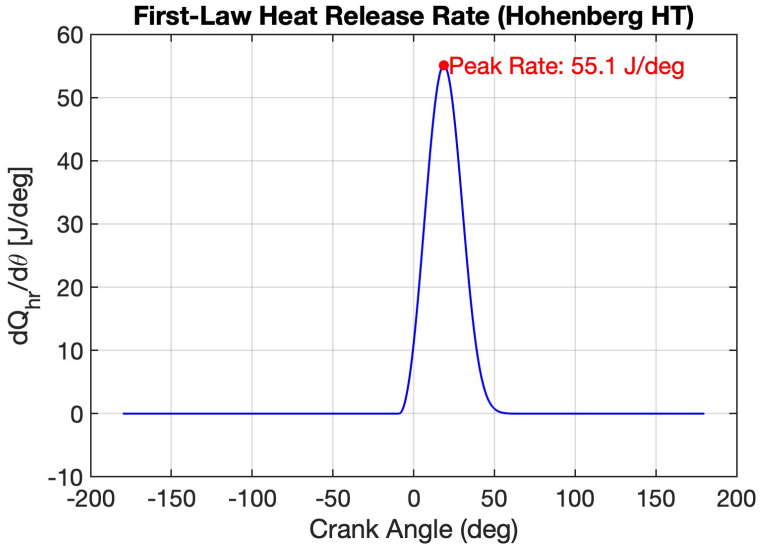

Figure 3.7: First-Law Derived Heat Release Rate (Hohenberg HTC Model) vs. Crank Angle.

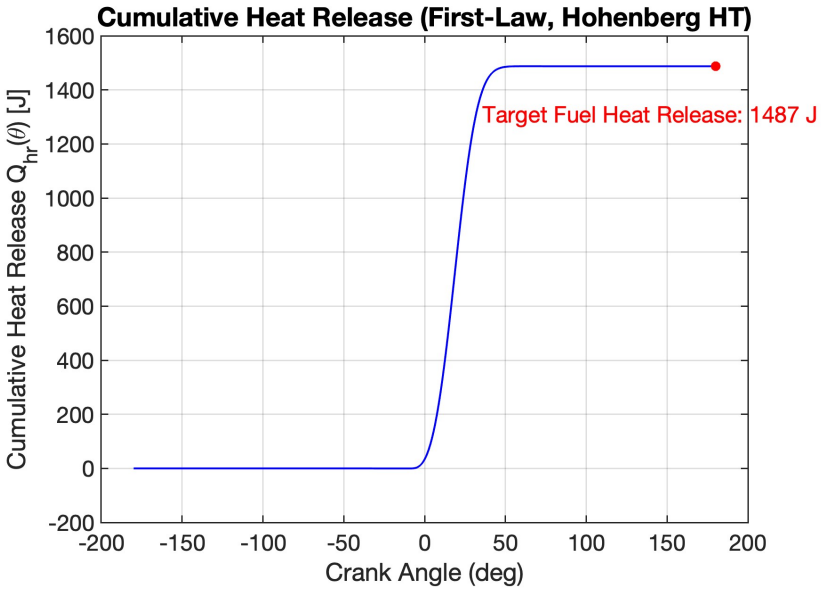

Figure 3.8: Cumulative Heat Release (from First Law with Hohenberg HTC Model) vs. Crank Angle.

Figure 3.7 presents the calculated rate of heat release ($dQ_{hr}/d\theta$). It exhibits a characteristic bell shape, peaking at $55.1\,\mathrm{J/°CA}$ approximately $19\,°\mathrm{CA}$, signifying the point of maximum energy liberation. Outside the defined combustion period, the rate is negligible. The corresponding cumulative heat release (Q_{hr}), shown in Figure 3.8, rises rapidly during combustion and plateaus at approximately $1487\,\mathrm{J}$. This value aligns with the total fuel energy input per cycle specified for the simulation (see Table 3.2), confirming that the modelled combustion process accounts for the available fuel energy.

3.3.3. In-Cylinder Pressure and Temperature (Effect of HTC Models)

While the overall combustion phasing is set by the Wiebe function, the choice of heat transfer correlation influences the precise magnitudes of in-cylinder pressure and temperature.

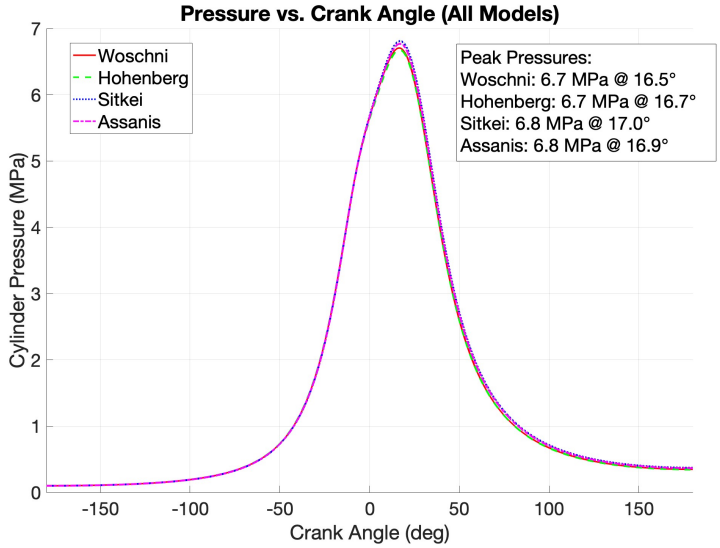

Figure 3.9: Comparison of Simulated In-Cylinder Pressure Traces Using Different Heat Transfer Models.

In Figure 3.9, the four distinct heat transfer models are used to compare the simulated in-cylinder pressure profiles. Subtle variations in peak pressure are noted, though: According to the Sitkei model, the peak pressure is roughly $6.8\,\mathrm{MPa}$ at $17.0\,°$CA, and the Assanis model predicts a very similar peak pressure at $16.9\,°$CA. The Hohenberg and Woschni correlations, on the other hand, produce somewhat lower peak pressures, of about $6.7\,\mathrm{MPa}$, at $16.7\,°$CA and $16.5\,°$CA, respectively. Even though relatively small in magnitude, these variations in peak pressure are a direct result of the varying cumulative heat loss that each correlation predicts, especially during the critical combustion and early expansion phases when in-cylinder temperatures and pressures are at their highest.

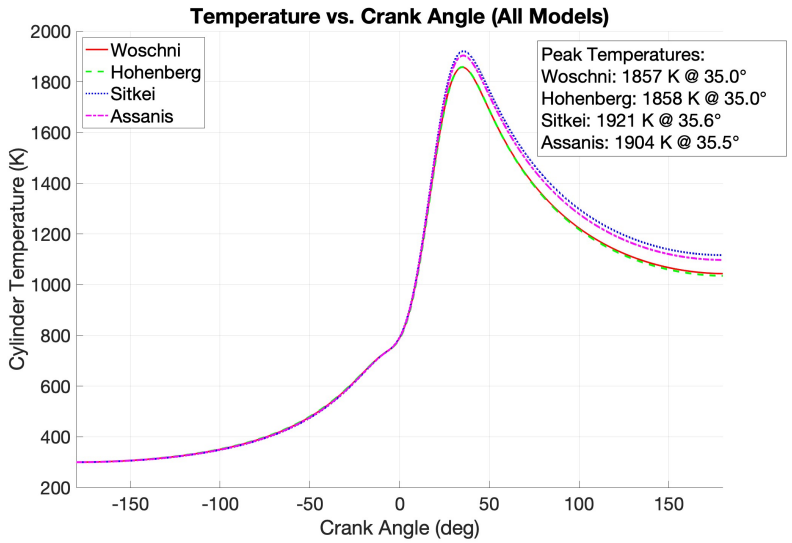

Figure 3.10: Comparison of Simulated Cylinder Temperature Traces Using Different Heat Transfer Models.

Similarly, Figure 3.10 shows the impact of the HTC models on the predicted cylinder temperature. The Sitkei model again predicts the highest peak temperature ($1921\,\mathrm{K}$ @ $35.6\,°$CA), followed by Assanis ($1904\,\mathrm{K}$ @ $35.5\,°$CA). Woschni and Hohenberg predict nearly identical and slightly lower peak temperatures (approx. $1857\,\mathrm{K}$ @ $35.0\,°$CA).

3.3.4. Heat Transfer Characteristics (Comparison of Correlations)

The selection of an empirical heat transfer correlation significantly influences the predicted thermal exchange between the in-cylinder gases and the combustion chamber walls. This subsection examines the distinct predictions for Heat Transfer Coefficient (HTC), wall heat flux (q”), and total instantaneous heat transfer rate (Q_{ht}) obtained from the Woschni, Hohenberg, Sitkei, and Assanis models for the baseline diesel simulation.

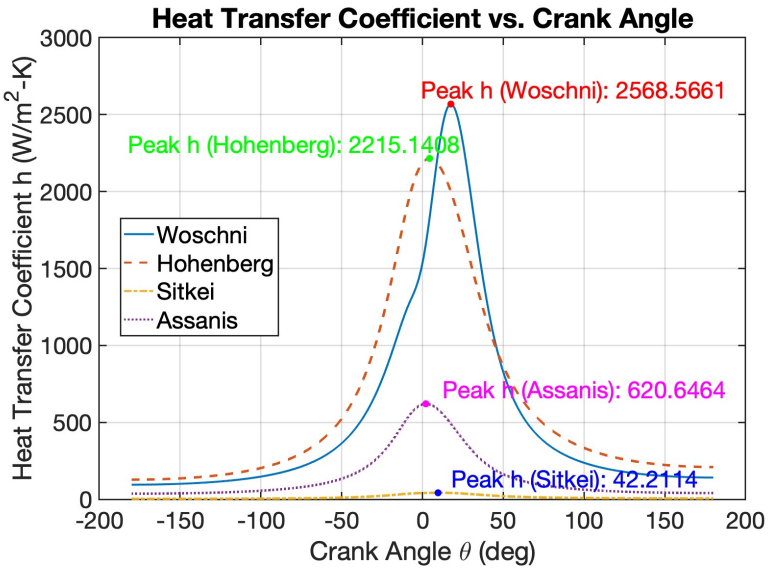

Figure 3.11: Comparison of Heat Transfer Coefficients from Different Correlations.

Figure 3.11 illustrates the HTC profiles. The Woschni correlation yields the highest peak HTC (approx. $2569\,\mathrm{W/m^2{-}K}$), closely followed by Hohenberg (approx. $2215\,\mathrm{W/m^2{-}K}$). Both are known for their strong dependence on in-cylinder pressure and characteristic gas velocity, which includes a term for combustion-induced turbulence in Woschni's case, leading to these elevated values during the high-pressure, high-temperature combustion phase near TDC. The Assanis model, a modified Woschni formulation that often uses chamber height as a characteristic length and can temper the combustion velocity term, predicts a substantially lower peak HTC (approx. $621\,\mathrm{W/m^2{-}K}$). The Sitkei correlation, which frequently emphasises mean piston speed and an equivalent hydraulic diameter, results in the lowest peak HTC (approx. $42\,\mathrm{W/m^2{-}K}$) among the four, suggesting a lower sensitivity to peak combustion pressures or gas velocities in its formulation for this engine setup. All correlations correctly phase their peak HTC around TDC, coinciding with peak combustion activity.

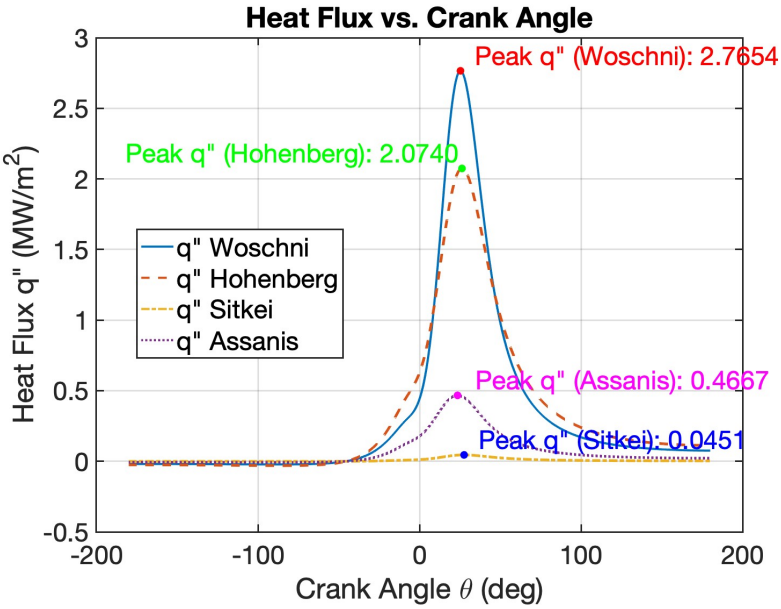

Figure 3.12: Comparison of Heat Flux (q") from Different Correlations.

The predicted wall heat flux (q"), depicted in Figure 3.12, is a direct consequence of the HTC and the gas-to-wall temperature difference ($T_g - T_w$). The trends largely mirror those of the HTC, with Woschni predicting the highest peak q" ($2.77\,\mathrm{MW/m^2}$), followed by Hohenberg ($2.07\,\mathrm{MW/m^2}$). Assanis ($0.47\,\mathrm{MW/m^2}$) and Sitkei ($0.045\,\mathrm{MW/m^2}$) predict considerably lower peak heat flux intensities. These substantial variations underscore the significant uncertainty inherent in predicting peak local heat transfer rates using different empirical approaches, even when driven by the same underlying thermodynamic cycle simulation.

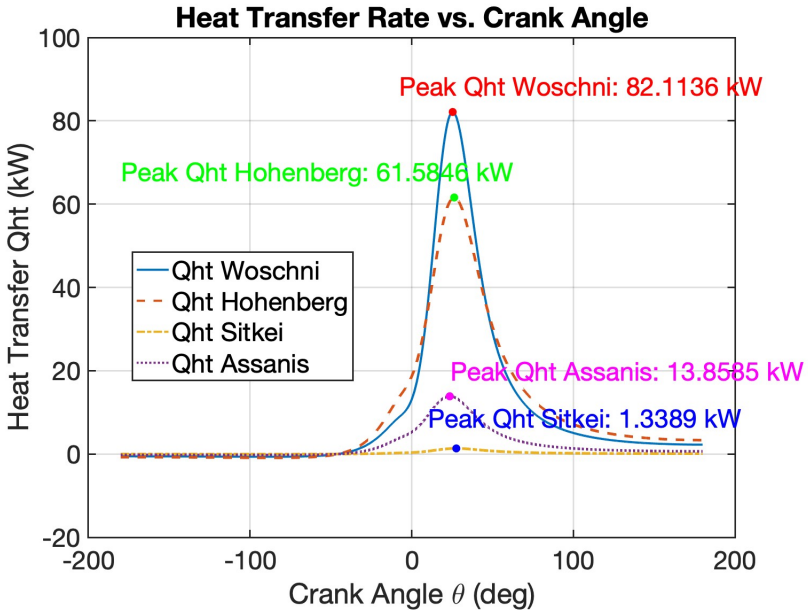

Figure 3.13: Comparison of Total Heat Transfer Rates (Q_{ht}) from Different Correlations.

The total instantaneous heat transfer rate (Q_{ht}) from the cylinder gases to the walls, shown in Figure 3.13, reflects the combined effect of HTC, the gas-wall temperature difference, and the instantaneous heat transfer surface area ($A_s(\theta)$). Consequently, the Q_{ht} profiles follow the q" trends. Woschni again yields the highest peak Q_{ht} (approx. $82.1\,\mathrm{kW}$), succeeded by Hohenberg ($61.6\,\mathrm{kW}$). Assanis and Sitkei predict markedly lower peak heat transfer rates, at approximately $13.9\,\mathrm{kW}$ and $1.3\,\mathrm{kW}$, respectively. These significant disparities in predicted Q_{ht} have direct and important implications for the overall simulated energy balance, influencing the calculated net work output and thermal efficiency of the engine cycle, as will be quantified in the subsequent summary of performance metrics.

3.3.5. Rate of Pressure Change and P-V Diagram

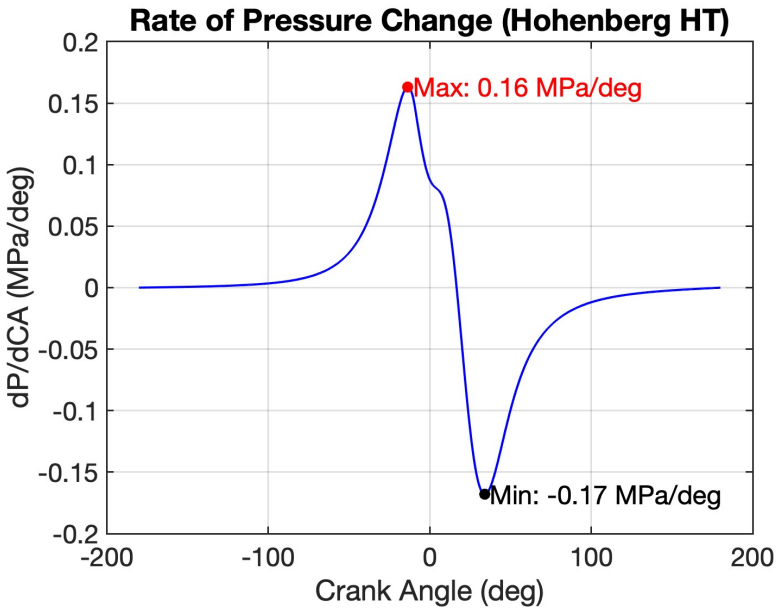

Figure 3.14: Rate of In-Cylinder Pressure Change (dP/dCA) using Hohenberg HTC Model.

The rate of in-cylinder pressure change (dP/dCA), illustrated in Figure 3.14 using results from the Hohenberg heat transfer model, offers a sensitive indication of combustion phasing and intensity. The profile exhibits a characteristic sharp rise, peaking at $0.16\,\mathrm{MPa/°CA}$ shortly after Top Dead Centre (TDC), which corresponds to the phase of rapid energy release from combustion. Subsequently, during the expansion stroke, dP/dCA becomes negative, reaching a minimum of $-0.17\,\mathrm{MPa/°CA}$ as the gas pressure decreases due to volume increase and heat loss. The precise location and magnitude of these positive and negative peaks are critical for assessing combustion stability and relating to phenomena such as engine knock or noise.

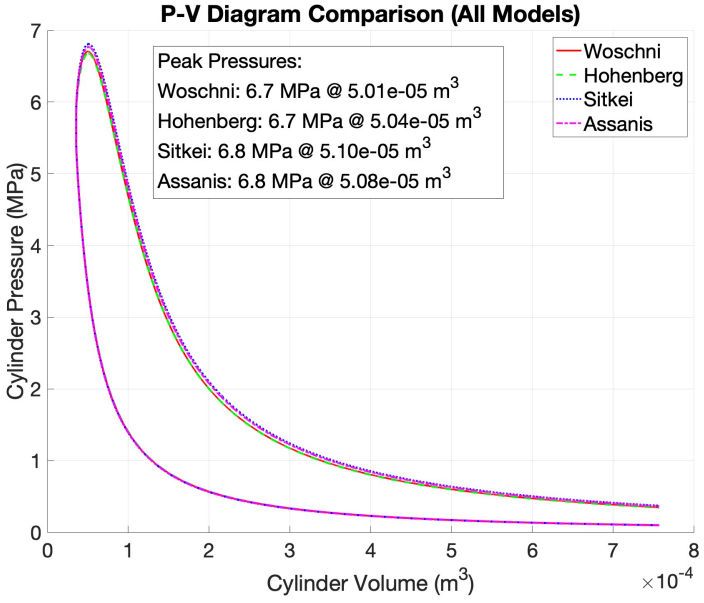

Figure 3.15: Comparative P-V Diagrams Using Different Heat Transfer Correlations.

In Figure 3.15, the P-V diagrams compare the various heat transfer models and graphically depict the work performed during the compression and expansion strokes. Although these open-loop diagrams have similar general shapes, the enclosed area varies slightly, reflecting the various heat loss predictions from each correlation. For instance, the Sitkei correlation, which consistently predicts lower total heat transfer rates (Q_{ht}) (as seen in Figure 3.13), yields a P-V loop that visually appears to encompass a slightly larger area. This suggests a marginally higher net indicated work for the modelled portion of the cycle. In contrast, P-V diagrams with slightly smaller enclosed areas are typically produced by correlations like Woschni or Hohenberg that predict higher heat loss. Since the simulation only considers the compression and expansion strokes and leaves out the gas exchange processes that would complete the thermodynamic cycle, these diagrams are shown as ”open” loops. Nonetheless, the area within these open loops provides a comparative measure of the net work transfer during the high-pressure part of the cycle under different heat transfer assumptions.

3.3.6. Comparative Numerical Performance Metrics Across Heat Transfer Correlations

The choice of heat transfer correlation, while showing similar dynamic pressure and temperature profiles (Figures 3.9 and 3.10), significantly impacts the integrated performance metrics of the simulated diesel engine. Table 3.4 presents a quantitative comparison of key output parameters obtained using the Woschni, Hohenberg, Sitkei, and Assanis correlations. All other engine and operating parameters were held constant for this comparison.

Table 3.4: Comparative Diesel Engine Performance Metrics and Thermal Conditions with Different Heat Transfer Correlations

Parameter	Woschni	Hohenberg	Sitkei	Assanis
Energy Balance (per cycle)				
Fuel Energy Input (J)	1487.72	1487.72	1487.72	1487.72
Total Actual Heat Release (J)	1487.72	1487.72	1487.72	1487.72
Total Heat Loss (J)	150.35	168.35	5.56	43.61
Total Internal Energy Change (J)	625.54	618.23	687.00	671.03
Total Actual Work (J)	746.84	743.68	796.03	782.54
Performance Indicators				
Efficiency (%)	50.20	49.99	53.51	52.60
IMEP (bar)	10.34	10.30	11.03	10.84
Crank Angle at Max Pressure (°CA)	16.50	16.70	17.00	16.90
Volumetric Efficiency (%)	105.75	105.75	105.75	105.75
Mass Loss	0.00	0.00	0.00	0.00
Thermal Conditions				
Peak Gas Temperature (K)	1857.46	1858.39	1920.99	1903.75
Average Gas Temperature (K)	860.67	858.59	892.17	883.94

Table 3.4 provides a quantitative comparison of key performance metrics and thermal parameters predicted by the diesel simulation when employing each of the four different heat transfer correlations. As expected, the specified **Fuel Energy Input** and the **Total Actual Heat Release** (defined by the Wiebe function to match this input) are consistent at approximately $1487.7\,\mathrm{J}$ across all models. However, the subsequent partitioning of this released energy into work, heat loss, and change in internal energy, along with other performance indicators, varies markedly.

A crucial check is the first law energy balance for the closed cycle: $Q_{\text{release}} \approx W_{\text{actual}} + Q_{\text{loss,total}} + \Delta U_{\text{total}}$.

- For Woschni: $746.84\,\mathrm{J}(\text{Work}) + 150.35\,\mathrm{J}(\text{Loss}) + 625.54\,\mathrm{J}(\Delta U) = 1522.73\,\mathrm{J}$.
- For Hohenberg: $743.68\,\mathrm{J}(\text{Work}) + 168.35\,\mathrm{J}(\text{Loss}) + 618.23\,\mathrm{J}(\Delta U) = 1530.26\,\mathrm{J}$.
- For Sitkei: $796.03\,\mathrm{J}(\text{Work}) + 5.56\,\mathrm{J}(\text{Loss}) + 687.00\,\mathrm{J}(\Delta U) = 1488.59\,\mathrm{J}$.
- For Assanis: $782.54\,\mathrm{J}(\text{Work}) + 43.61\,\mathrm{J}(\text{Loss}) + 671.03\,\mathrm{J}(\Delta U) = 1497.18\,\mathrm{J}$.

The sums for Sitkei and Assanis demonstrate a closer numerical match with the input heat release of $1487.72\,\mathrm{J}$ compared to Woschni and Hohenberg, which show larger deviations (approximately $35\,\mathrm{J}$ and $42.5\,\mathrm{J}$ respectively). These discrepancies can arise from the accumulation of numerical integration errors, which may be influenced differently by each heat transfer correlation's effect on the pressure derivative calculation throughout the cycle.

The predicted **Total Heat Loss** is where the models differ most. While Assanis also shows a relatively modest loss of $43.61\,\mathrm{J}$, the Sitkei correlation predicts an exceptionally low heat loss of only $5.56\,\mathrm{J}$. The Woschni and Hohenberg models, on the other hand, predict much greater heat losses, at $150.35\,\mathrm{J}$ and $168.35\,\mathrm{J}$, respectively. Due to the different HTC and heat transfer rate magnitudes previously shown (Figures 5.14 to 5.16), the predicted heat loss between Sitkei and Hohenberg is nearly thirty times different, highlighting the simulation's high sensitivity to the selected heat transfer model.

These differences in heat loss have a direct impact on the output of **Total Actual Work** and, in turn, the indicated **Thermal Efficiency**. With the least amount of heat loss, the Sitkei model produces the most work ($796.03\,\mathrm{J}$) and efficiency ($53.51\,\%$). This pattern is reflected in the Assanis model. In contrast, Woschni performs similarly to Hohenberg, which predicts the largest heat loss and yields the lowest work output ($743.68\,\mathrm{J}$) and efficiency ($49.99\,\%$). This inverse relationship is a direct consequence of the first law of thermodynamics: energy not lost as heat is available for work or to change the system's internal energy.

The **Total Internal Energy Change** (ΔU) over the modelled cycle also reflects this energy distribution. Models predicting lower heat loss (Sitkei, Assanis) generally show a larger increase in internal energy from the start to the end of the cycle compared to models with higher heat loss (Woschni, Hohenberg).

The **Peak Gas Temperature** is highest for the Sitkei model ($1921.0\,\mathrm{K}$), consistent with its minimal heat loss. Assanis also predicts a high peak temperature ($1903.8\,\mathrm{K}$), while Woschni ($1857.5\,\mathrm{K}$) and Hohenberg ($1858.4\,\mathrm{K}$) yield lower, very similar peak values. A similar pattern is seen in the **Average Gas Temperature** over the cycle, where Sitkei ($892.2\,\mathrm{K}$) and Assanis ($883.9\,\mathrm{K}$) maintain higher average temperatures than Woschni ($860.7\,\mathrm{K}$) and Hohenberg ($858.6\,\mathrm{K}$).

Parameters that show less sensitivity to the specific heat transfer model include the **Crank Angle at Maximum Pressure**, which varies by only half a degree (from $16.5\,°$CA to $17.0\,°$CA). The **Volumetric Efficiency** ($105.75\,\%$) remains constant, as it is primarily determined by engine geometry, intake conditions, none of which were altered by the heat transfer correlation choice in these comparative runs. The calculated **IMEP** values directly correlate with the work output, with the Sitkei model yielding the highest IMEP ($11.03\,\mathrm{bar}$).

In conclusion, the choice of heat transfer correlation introduces significant variability in predicting the energy balance and performance of the simulated diesel engine. The Woschni and Hohenberg models estimate higher overall heat losses, leading to more conservative performance predictions. The Sitkei model, in this application, tends towards near-adiabatic conditions, maximising work output. The Assanis model offers an intermediate outcome. These findings highlight the critical role of accurate heat transfer sub-modelling in 0D simulations and the inherent uncertainties associated with widely used empirical correlations.

4

Diesel Model Validation and Improvements

In this chapter, the developed zero-dimensional (0D) thermodynamic engine model for diesel combustion is evaluated and improved. There are two main phases to this chapter's structure. The baseline diesel model is first validated. To evaluate the model's predictive power for important in-cylinder phenomena under specific operating conditions, simulation outputs are compared to published experimental data for a Kubota 140 diesel engine.

Among the model improvements is the use of a temperature-dependent specific heat ratio (γ) to account for changes in gas properties, the computation of a specific gas constant (R) based on estimated exhaust product composition, and the addition of a double-zone Wiebe function to more accurately depict distinct combustion phases. In order to demonstrate how these improvements contribute to a more complex depiction of diesel engine operation, their effects on the simulation results are examined.

4.1. Validation Against Kubota 140 Engine Data

This section details the validation of the 0D thermodynamic engine model. The simulation results are compared against published experimental data for a Kubota 140 single-cylinder diesel engine, as reported by Bobi et al. [20]. This comparison focuses on key in-cylinder parameters that serve as critical indicators of the model's accuracy and its ability to capture essential engine cycle phenomena. Specifically, the validation assesses:

- The Heat Release Rate profile, to evaluate the combustion model's representation.
- In-Cylinder Pressure and Temperature traces, as fundamental thermodynamic variables sensitive to both combustion and heat transfer modelling.
- Heat Flux and Heat Transfer Coefficients predicted by the Hohenberg and Woschni correlations, to gauge their performance in estimating wall heat transfer intensity and characteristics.

The simulation was set up to replicate the geometry of the Kubota 140 engine and a specific operating point from the Bobi et al. study [20]. The core 0D thermodynamic model structure, numerical solution method (Euler forward integration), and the basic formulations of the heat transfer correlations were all maintained from the primary Hatz 1D90E simulations. A summary of the Kubota 140 engine specifications derived from manufacturer data [44] and the particular simulation input parameters used or derived for this validation exercise can be found in Table 4.1.

Table 4.1: Kubota 140 Engine Specifications and Simulation Input Parameters for Validation Case

Parameter	Symbol	Value	Unit/Note
Engine Specifications (Kubota 140 [44])			
Engine Type	–	Single Cylinder, 4-Stroke Diesel	
Compression Ratio	r	18	–
Bore	B	0.096	m
Stroke	S	0.097	m
Displacement Volume	V_d	$0.709\,\mathrm{L}$	
Rated Speed	N	2400	RPM
Rated Power	P_b	9.26	kW
Simulation Input Parameters & Assumptions (for Kubota 140 Validation)			
Fuel Type	–	Diesel (LHV = $44.8 \times 10^6\,\mathrm{J\,kg^{-1}}$)	
Fuel Flow Rate	$\dot{m}_f$	$2.38\,\mathrm{kg\,h^{-1}}$	From [20]
Air-Fuel Ratio	AFR	14.5	Stoichiometric (Assumed)
Start of Combustion	θ_s	-13	°CA (Tuned to match [20])
Combustion Duration	θ_d	40	°CA (Tuned to match [20])
Wiebe Factor	a	2	Dimensionless (Tuned)
Wiebe Exponent	n	3	Dimensionless (Tuned)
Specific Heat Ratio	γ	1.3	Constant, assumed
Temp. at BDC	T_{BDC}	$200\,\mathrm{K}$	From [20]
Pressure at BDC	P_{BDC}	$100\,\mathrm{kPa}$	From [20]
Wall Temperature	T_w	$450\,\mathrm{K}$	From [20] ($t_w = 2.25$)
Specific Gas Constant	R	$0.2869\,\mathrm{kJ\,kg^{-1}\,K^{-1}}$	Assumed
Derived Gas Properties (from assumed γ and R)			
Specific Heat	c_p	$1.2436\,\mathrm{kJ\,kg^{-1}\,K^{-1}}$	Calculated
Specific Heat	c_v	$0.9563\,\mathrm{kJ\,kg^{-1}\,K^{-1}}$	Calculated
Air Density	$\rho_{air,BDC}$	$1.7440\,\mathrm{kg\,m^{-3}}$	Calculated

A number of parameters were taken straight from the study by Bobi et al. [20] in order to simulate the Kubota 140 engine at its $2400\,\mathrm{RPM}$ operating point. These parameters included the fuel flow rate ($\dot{m}_f = 2.38\,\mathrm{kg/h}$), the effective wall temperature ($T_w = 450\,\mathrm{K}$), and the BDC conditions ($T_{BDC} = 200\,\mathrm{K}, P_{BDC} = 100\,\mathrm{kPa}$).The Wiebe combustion parameters ($\theta_s = -13\,°\mathrm{CA}$, $\theta_d = 40\,°\mathrm{CA}$, $a = 2, n = 3$) were iteratively tuned to achieve the best possible agreement between the simulation's predicted in-cylinder pressure, temperature and heat release profiles and those presented in the reference study. A constant specific heat ratio ($\gamma = 1.3$) and a specific gas constant ($R = 0.2869\,\mathrm{kJ\,kg^{-1}\,K^{-1}}$) were assumed for the working fluid, from which the specific heats c_p and c_v were derived, ensuring thermodynamic consistency. The air-fuel ratio was set to stoichiometric (14.5) based on the provided fuel flow rate and an implied air flow to match typical CI engine operation for the given data.

4.1.1. Comparison of Simulation Results with Published Kubota 140 Data

The following subsections present a visual and quantitative comparison of key in-cylinder parameters from the 0D simulation against data extracted or estimated from the reference study by Bobi et al. [20] for the Kubota 140 engine operating at $2400\,\mathrm{RPM}$. This comparison focuses on in-cylinder pressure, temperature, heat release rate, and specific heat transfer characteristics.

i. In-Cylinder Pressure

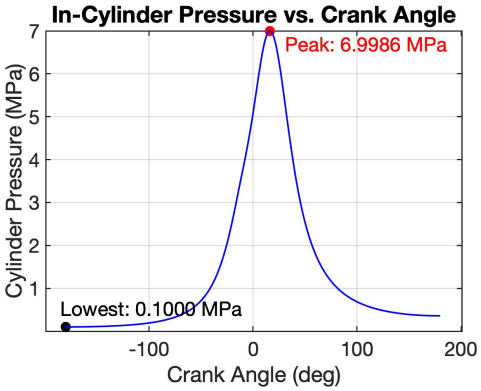

(a) Simulated Pressure

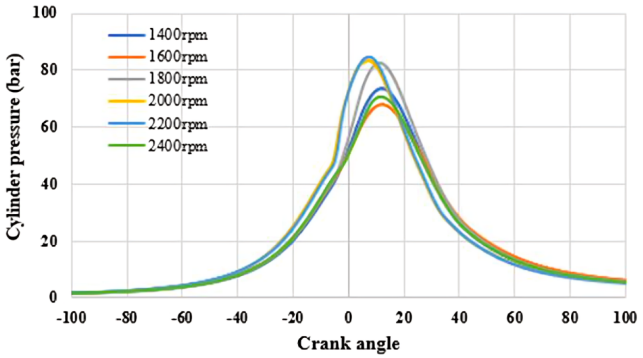

(b) Experimental Pressure [20]

Figure 4.1: Comparison of Simulated and Experimental In-Cylinder Pressure vs. Crank Angle for Kubota 140 Engine at $2400\,\mathrm{RPM}$.

Figure 4.1 compares the simulated in-cylinder pressure trace (a) with the experimental pressure curve for $2400\,\mathrm{RPM}$ reported by Bobi et al. [20] (b). The simulation predicts a peak pressure of approximately $7.0\,\mathrm{MPa}$ (or $70\,\mathrm{bar}$), occurring around $15\,°\mathrm{CA}$. This aligns closely with the experimental data, which shows a peak pressure also near $70\,\mathrm{bar}$ (estimated from their plot for the $2400\,\mathrm{RPM}$ green line) occurring between $10\,°\mathrm{CA}$ and $15\,°\mathrm{CA}$. The overall shape of the pressure curve, including the compression slope, the rapid rise during combustion, and the subsequent expansion, demonstrates good qualitative agreement between the simulation and the experimental trend.

ii. Cylinder Temperature

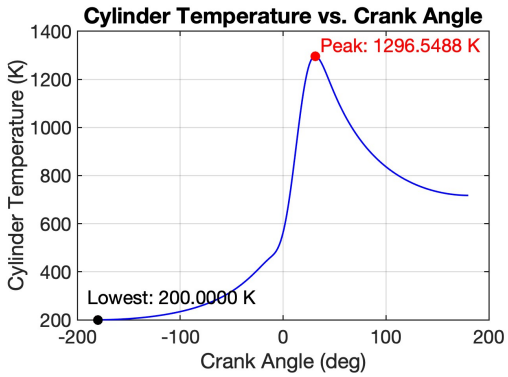

(a) Simulated Temperature

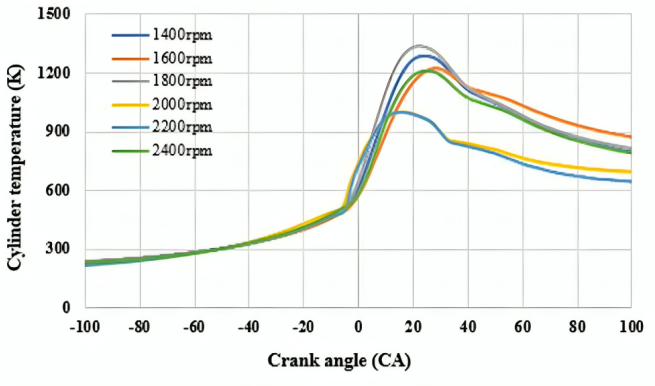

(b) Experimental Temperature [20]

Figure 4.2: Comparison of Simulated and Experimental In-Cylinder Temperature vs. Crank Angle for Kubota 140 Engine at $2400\,\mathrm{RPM}$.

Figure 4.2 compares the experimental data with the simulated cylinder temperature. A peak temperature of roughly $1297\,\mathrm{K}$ is predicted by simulation (a). A peak temperature of about $1200\,\mathrm{K}$ is indicated by the experimental data for $2400\,\mathrm{RPM}$ (b) from Bobi et al. [20]. The overall temperature profile, the sharp increase during combustion, and the subsequent drop during expansion all show a reasonable match, even though the simulated peak is somewhat higher. The simulation's peak temperature phasing, which happens shortly following the primary combustion event, also seems to be in line with the experimental trend.

iii. Heat Release Rate

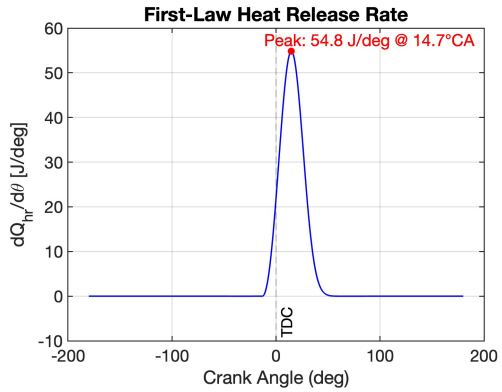

(a) Simulated Heat Release Rate

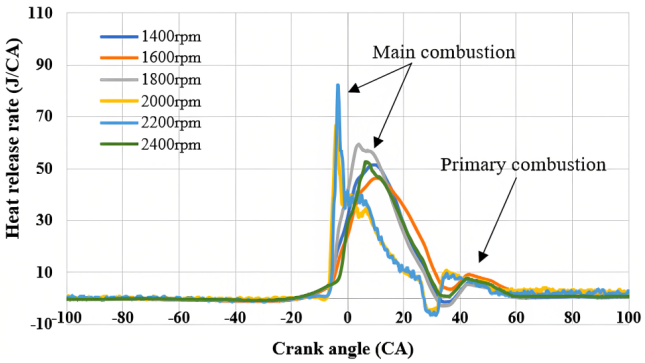

(b) Experimental Heat Release Rate [20]

Figure 4.3: Comparison of Simulated and Experimental Heat Release Rate vs. Crank Angle for Kubota 140 Engine at $2400\,\mathrm{RPM}$.

Figure 4.3 compares the first law-derived heat release rate (HRR) from the simulation (a) with the experimental HRR data from Bobi et al. [20] at $2400\,\mathrm{RPM}$ (b). The simulation predicts a peak HRR of $54.8\,\mathrm{J/°CA}$ at approximately $14.7\,°\mathrm{CA}$. The experimental data shows a primary peak HRR for $2400\,\mathrm{RPM}$ of around $50\,\mathrm{J/°CA}$ (green line), near $10\,°\mathrm{CA}$. While the simulated peak magnitude is slightly higher and marginally delayed, the overall shape of the main combustion pulse and its duration are reasonably well captured.

iv. Heat Transfer Coefficient (Woschni and Hohenberg Models)

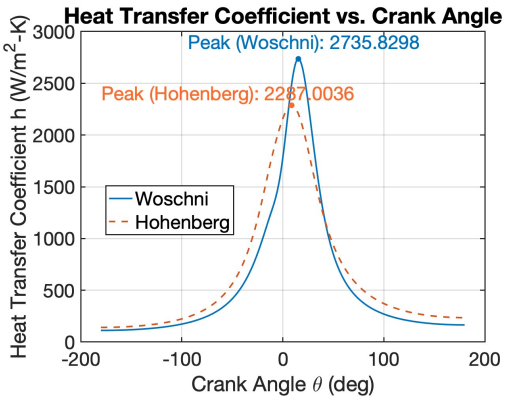

(a) Simulated HTC (Woschni & Hohenberg)

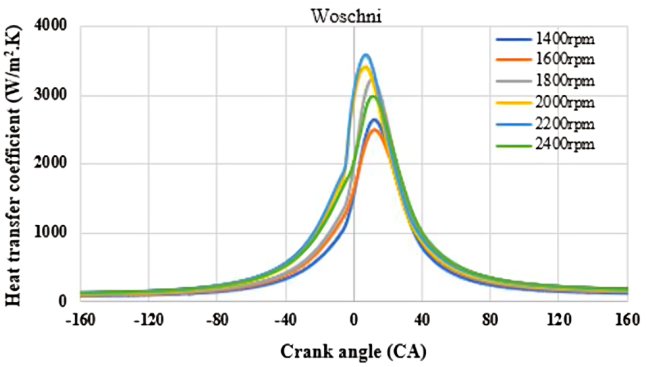

(b) Exp. Trend (Woschni) [20]

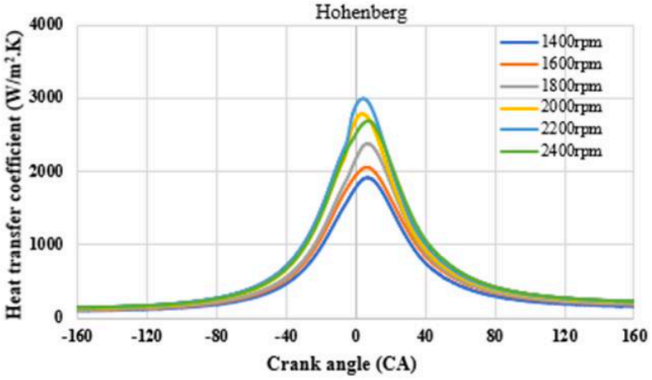

(c) Exp. Trend (Hohenberg) [20]

Figure 4.4: Comparison of Simulated and Experimental Heat Transfer Coefficient (HTC) vs. Crank Angle for Kubota 140 Engine at $2400\,\mathrm{RPM}$.

The simulated Heat Transfer Coefficients (HTC) using Woschni and Hohenberg correlations are shown in Figure 4.4(a), alongside experimental HTC trends from Bobi et al. [20] in Figure 4.4(b) and (c) for Woschni at $2400\,\mathrm{RPM}$. The simulated Woschni HTC peaks at $2736\,\mathrm{W/m^2{-}K}$, while the Hohenberg model predicts a peak of $2287\,\mathrm{W/m^2{-}K}$. The experimental Woschni data for $2400\,\mathrm{RPM}$ shows a peak around $2900\,\mathrm{W/m^2{-}K}$, and Hohenberg around $2400\,\mathrm{W/m^2{-}K}$. Both simulated models capture the sharp rise and fall of HTC around TDC, with Woschni generally predicting higher values than Hohenberg, consistent with the experimental trends presented by Bobi et al. The simulated magnitudes are in reasonable agreement with the experimental data for the corresponding correlation.

v. Heat Flux (Woschni and Hohenberg Models)

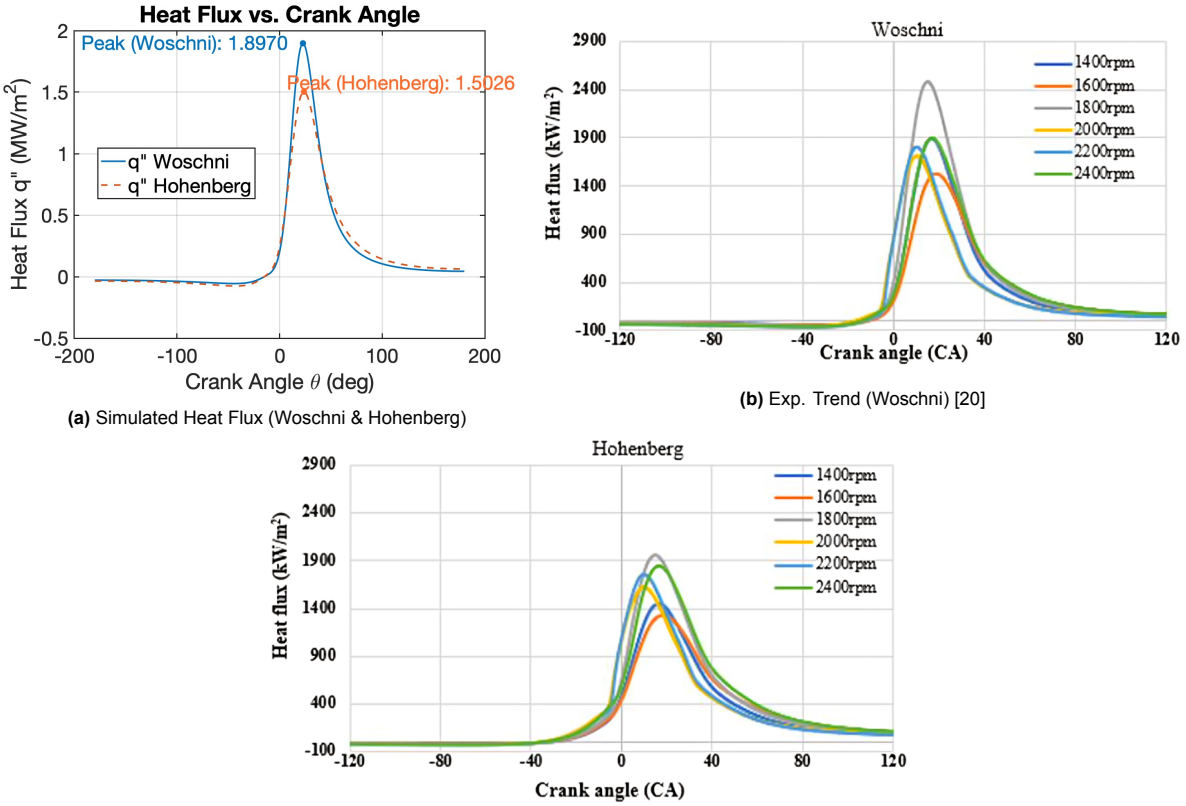

(a) Simulated Heat Flux (Woschni & Hohenberg)

(b) Exp. Trend (Woschni) [20]

(c) Exp. Trend (Hohenberg) [20]

Figure 4.5: Comparison of Simulated and Experimental Wall Heat Flux (q") vs. Crank Angle for Kubota 140 Engine at $2400\,\mathrm{RPM}$.

Figure 4.5(a) presents the simulated wall heat flux (q"). The Woschni model predicts a peak q" of $1.90\,\mathrm{MW/m^2}$, and the Hohenberg model predicts $1.50\,\mathrm{MW/m^2}$. The experimental data from Bobi et al. [20] in Figure 4.5(b) and (c) for Woschni at $2400\,\mathrm{RPM}$, indicates peak heat flux values where Woschni is higher than Hohenberg. For Woschni at $2400\,\mathrm{RPM}$, the experimental peak is around $1900\,\mathrm{kW/m^2}$ (or $1.9\,\mathrm{MW/m^2}$), aligning well with the simulation. For Hohenberg at $2400\,\mathrm{RPM}$, the experimental peak appears to be around $1400\,\mathrm{kW/m^2}$ (or $1.4\,\mathrm{MW/m^2}$), also showing good agreement with the simulated $1.50\,\mathrm{MW/m^2}$. The overall phasing of the heat flux is well represented by both models in the simulation compared to the experimental trends.

Overall Validation Assessment
The validation against the Kubota 140 engine data at $2400\,\mathrm{RPM}$ demonstrates that the 0D thermodynamic simulation, with tuned Wiebe parameters and standard heat transfer correlations, achieves a good level of agreement with published experimental results for key in-cylinder parameters. The simulated pressure and temperature profiles, as well as the derived heat release rate, show strong qualitative and reasonable quantitative correspondence with the reference data. Furthermore, the heat transfer coefficients and wall heat fluxes predicted by both Woschni and Hohenberg models in the simulation are comparable in magnitude and trend to those reported in the experimental study by Bobi et al. [20] for the $2400\,\mathrm{RPM}$ operating condition. This provides confidence in the fundamental structure and parameterization of the developed model.

4.2. Diesel Combustion Model Improvement

This section talks about the improvements made to the diesel simulation presented in Chapter 3. The aim of these improvements was to make the simulation more accurate and refined. The following concepts were added or refined in the simulation code:

4.2.1. Double Zone Wiebe Function:

While the single-zone Wiebe (SW) equation presented in Equation 2.18 is the most commonly used form of the Wiebe function, there are several benefits to expanding this to a double-zone (DW) form. It was demonstrated in research by [39] and [45] that the single-zone model leads to lower-than-actual heat losses because of its inability to represent combustion features near the chamber walls. This can be solved through a double-zone Wiebe function that has 2 zones, as presented in Figure 4.1. One zone is for premixed combustion and the other for diffusive combustion.

$$\begin{aligned} x_b(\theta) =& \kappa \left\{ 1 - \exp\left[-a_1 \left(\frac{\theta - \theta_0}{\Delta\theta} \right)^{m_1+1} \right] \right\} \\ &+ (1-\kappa) \left\{ 1 - \exp\left[-a_2 \left(\frac{\theta - \theta_0}{\Delta\theta} \right)^{m_2+1} \right] \right\} \end{aligned} \tag{4.1}$$

Here, κ is the fraction of fuel that burns in the slow premixed combustion wall region. $a1, a2$ and $m1, m2$ are the Wiebe factors of the respective zones [46].

Double Wiebe Model Results Comparison
By updating the code with Equation 4.1, changes are noticed in several plots and results. The Hohenberg model was chosen for this comparison study as an example. The following can be noticed by comparing the simulation for the Hohenberg convective model between single- and double-zone (SW and DW) Wiebe simulations:

1. Combustion Phasing and Energy Release Profile: The mass fraction burnt (x_b) profile in Figure 4.6 highlights a key improvement. The double Wiebe (DW) trace initiates combustion earlier (around -8 °CA) and displays a clear two-stage progression. This inflection or change in slope is characteristic of diesel combustion, representing an initial rapid (premixed) burn followed by a more prolonged (diffusion) burn. The single Wiebe (SW), by contrast, shows a smoother, linear rise, which is a simplification of this two-phase reality.

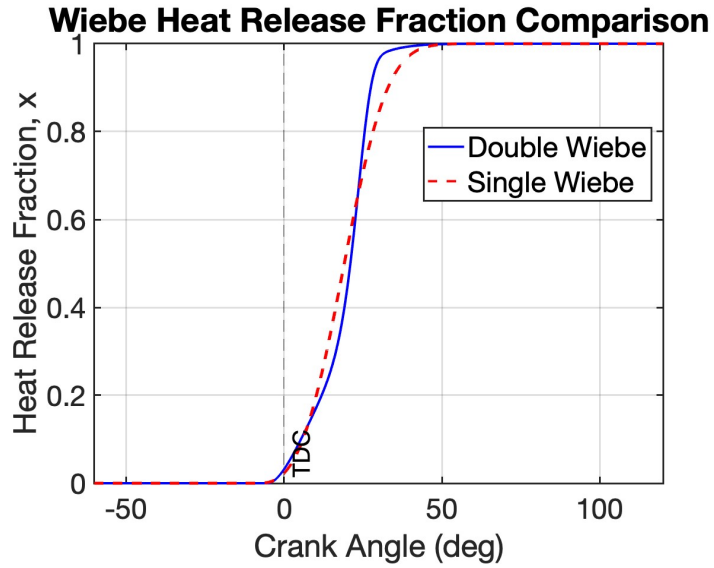

Figure 4.6: Wiebe Heat Release Fraction (x_b) Comparison for Single and Double Wiebe models.

This two-stage nature is explicitly visualised in the Average Rate of Heat Release (aROHR) (Figure 4.7). The DW model generates a distinct, sharp initial peak ($103.62\,\mathrm{J/°CA}$ @ $23.6\,$°CA), characteristic of the rapid premixed combustion phase in CI engines. The diffusion-controlled phase is then represented by a period of continuous heat release. Without this differentiation, the SW model yields only a single lower and broader peak ($55.09\,\mathrm{J/°CA}$ @ $18.7\,$°CA). A major step towards a more accurate depiction of diesel combustion physics is the DW's ability to model these two distinct phases.

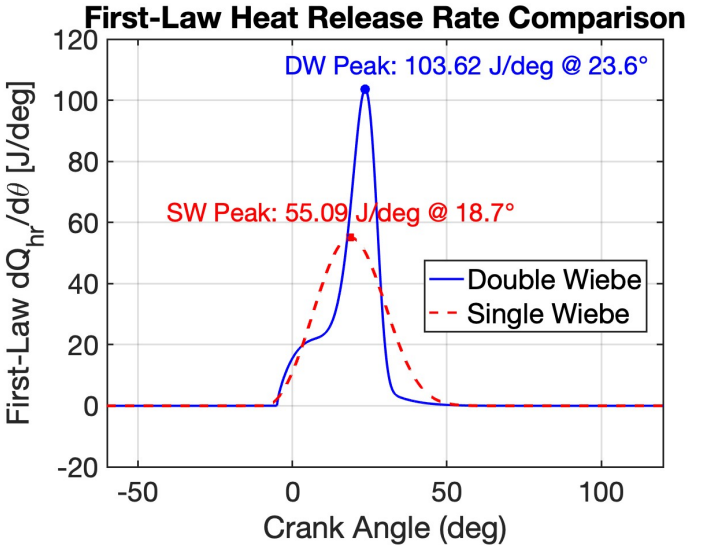

Figure 4.7: First-Law Heat Release Rate (aROHR) Comparison.

The cumulative heat release plot (Figure 4.8) visually confirms the difference. While both models ultimately release the same total amount of energy, the Double Wiebe (DW) curve rises much more steeply at the beginning. This steep initial rise indicates a faster accumulation of released energy early in the combustion process, which directly corresponds to the rapid premixed burning phase known to occur in diesel engines. The Single Wiebe, lacking this distinct initial phase, shows a more gradual energy accumulation.

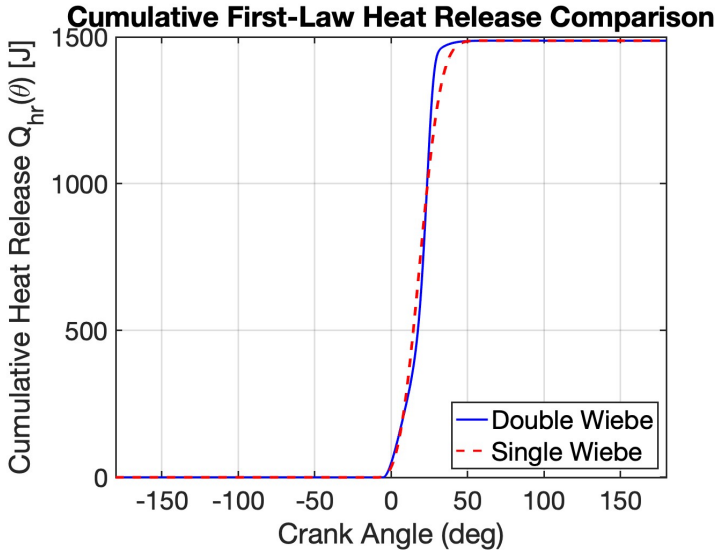

Figure 4.8: Cumulative First-Law Heat Release (Q_{hr}) Comparison.

2. Cylinder Pressure Dynamics and P-V Characteristics: Figure 4.9 shows the in-cylinder pressure. Although the single Wiebe (SW) simulation predicts a marginally higher absolute peak pressure ($6.71\,\mathrm{MPa}$ compared to the double Wiebe's (DW) $6.68\,\mathrm{MPa}$), the DW model's overall pressure curve provides a more realistic depiction of how diesel combustion influences cylinder pressure. Specifically, the DW pressure trace displays an initial, steeper rate of pressure rise that corresponds to its distinct premixed combustion phase, as evident from the aROHR profile. This two-stage impact on pressure development, with an initial quick rise from premixed burning and then continued pressure from diffusion burning, more closely mirrors the actual pressure characteristics observed in diesel engines than the singular, smoother pressure event predicted by the SW model. The later timing of the DW's overall peak pressure and the prolonged period of higher pressure during the expansion stroke are direct outcomes of this more detailed, two-stage heat release model.

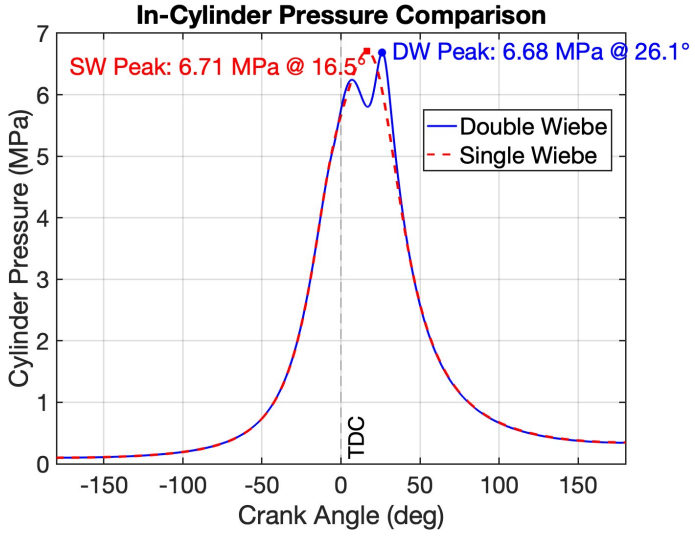

Figure 4.9: In-Cylinder Pressure Comparison.

The P-V diagram (Figure 4.10) reflects the pressure differences. The Double Wiebe model's distinct, two-stage heat release results in a P-V loop that is wider, especially during early expansion. This altered shape, stemming from the more detailed combustion representation, typically indicates a differ-

ent distribution of work production across the cycle, leading to a more accurate estimation of overall indicated work compared to a single-stage approximation.

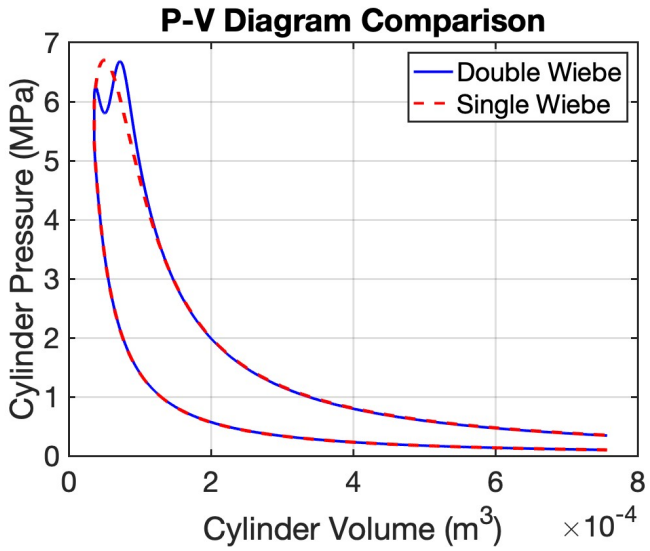

Figure 4.10: P-V Diagram Comparison.

3. In-Cylinder Gas Temperatures: The DW model's more intense initial (premixed) heat release directly leads to a significantly higher peak bulk gas temperature ($2038\,\mathrm{K}$) compared to the SW model ($1857\,\mathrm{K}$), as shown in Figure 4.11. The temperature rise is also visibly steeper for the DW case. Peak cycle temperatures have a significant impact on heat transfer rates, making their timing and prediction crucial. The combustion environment is better represented by the DW since it can capture a higher, earlier temperature peak due to distinct combustion phases.

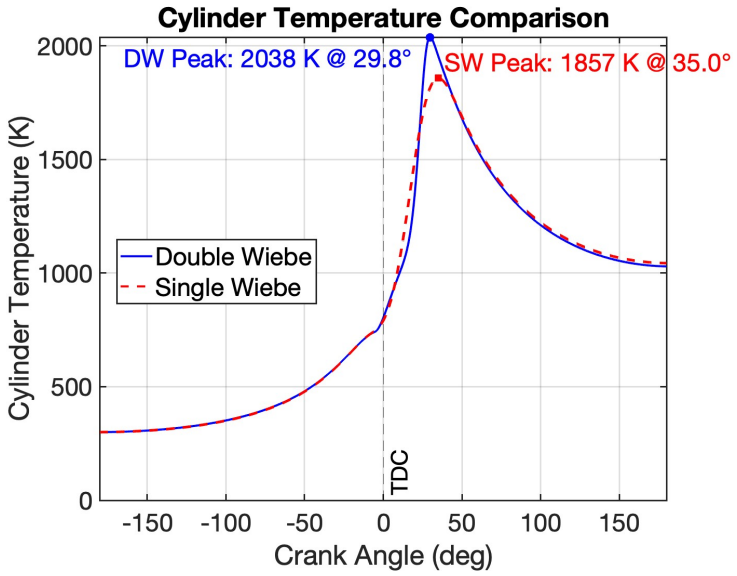

Figure 4.11: Cylinder Temperature Comparison.

4. Impact on Predicted Heat Transfer Characteristics (All Models): The more detailed combustion profile and altered in-cylinder temperatures predicted by the double Wiebe (DW) model have a cascading effect on the simulated heat transfer to the walls. This is observed across all four heat transfer correlations (Woschni, Hohenberg, Sitkei, and Assanis), as shown in Figures 4.12, 4.13, and 4.14.

Heat Transfer Coefficient (HTC):
The Heat Transfer Coefficients (HTCs) predicted by the DW model exhibit subtle differences from the single Wiebe (SW) model, as shown in Figure 4.12. With the Hohenberg model, for example, the DW simulation predicts a slightly higher peak HTC ($2689.8\,\mathrm{W/m^2{-}K}$ at $3.4\,°$CA) than the SW simulation ($2664.3\,\mathrm{W/m^2{-}K}$ at $3.8\,°$CA). Conversely, for the Woschni model, the SW simulation results in a higher peak HTC ($2581.7\,\mathrm{W/m^2{-}K}$ at $17.4\,°$CA) compared to the DW model ($2501.7\,\mathrm{W/m^2{-}K}$ at $25.5\,°$CA). Similar model-dependent variations are seen with Sitkei and Assanis. These shifts in HTC are a direct response of each empirical correlation to the subtly altered in-cylinder pressure and temperature fields, as well as potentially different characteristic velocities, produced by the more detailed DW combustion profile.

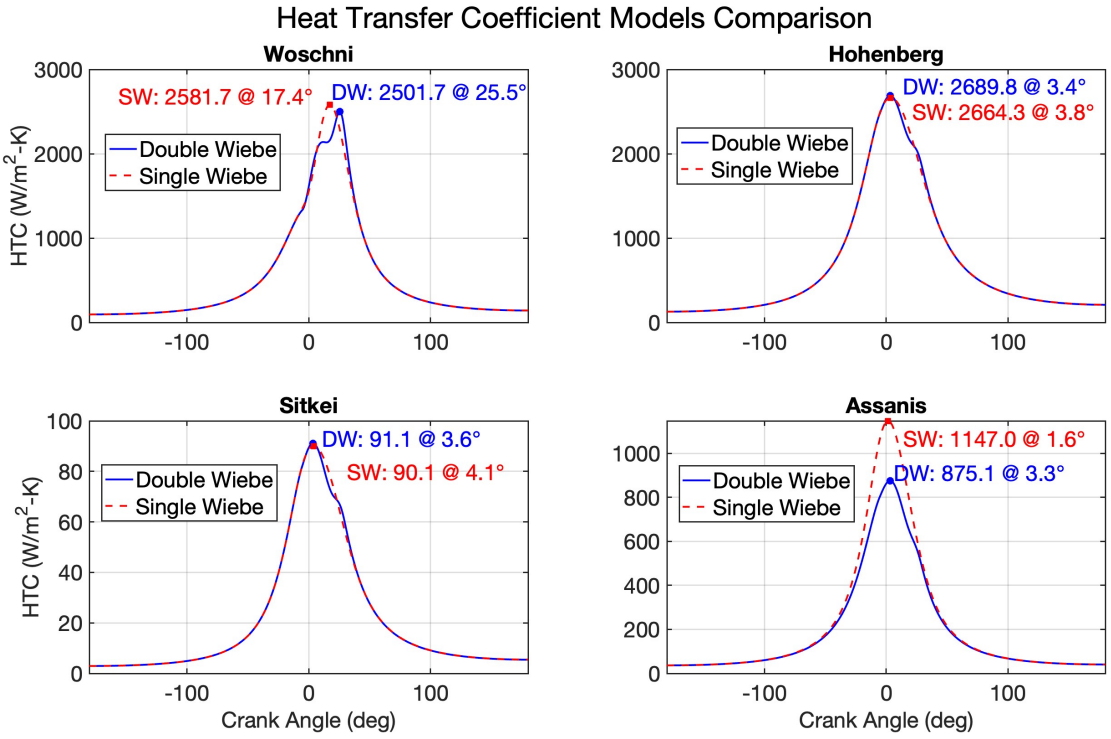

Figure 4.12: Heat Transfer Coefficient (HTC) Comparison: Single vs. Double Wiebe, across all four HTC models.

Heat Flux (q"):
A more consistent trend emerges when observing the wall heat flux (q"), as depicted in Figure 4.13. Across all four heat transfer correlations, the DW simulation consistently predicts a higher peak heat flux than the SW simulation. For example, using the Hohenberg model, the DW peak q" is $2.92\,\mathrm{MW/m^2}$, while the SW peak is $2.38\,\mathrm{MW/m^2}$. Likewise, for Woschni, DW q" peaks at $3.64\,\mathrm{MW/m^2}$ as opposed to SW's $2.77\,\mathrm{MW/m^2}$. The DW model achieves much higher peak gas temperatures (Figure 4.11), which is the main cause of this overall increase in predicted peak q". Heat transfer intensity is higher per unit area in the DW case due to the larger temperature difference ($T_g - T_w$) between the gas and the wall.

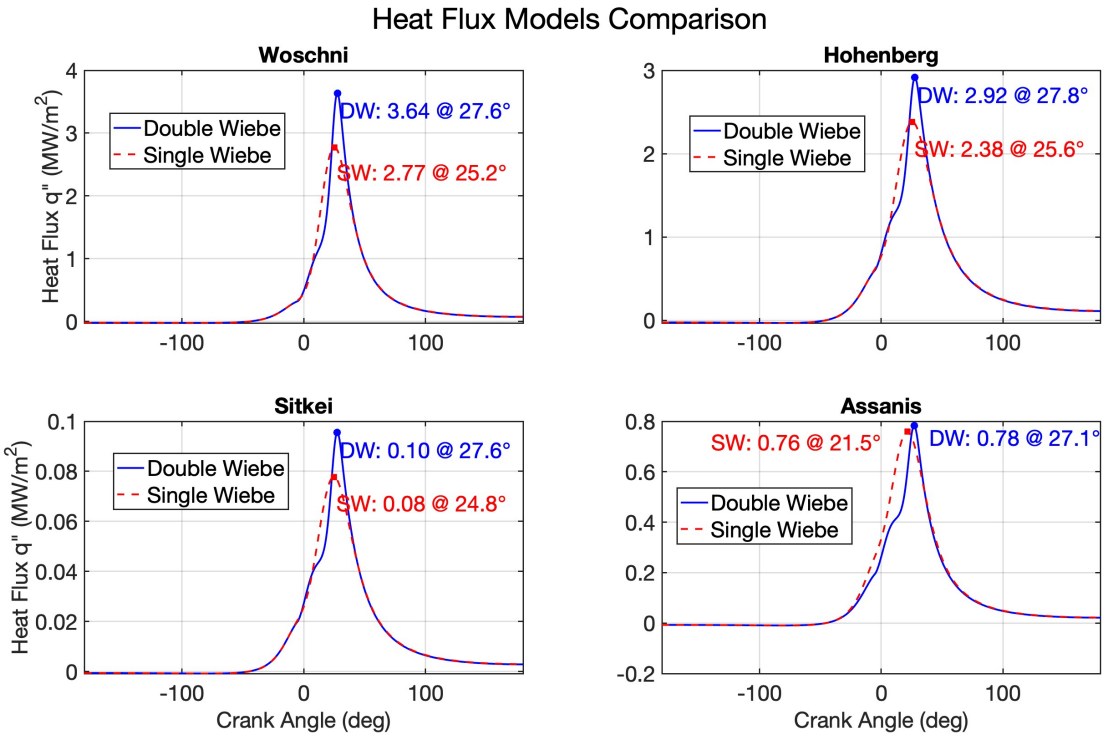

Figure 4.13: Heat Flux (q") Comparison: Single vs. Double Wiebe, across all four HTC models.

Total Heat Transfer Rate (Q_{ht}):
The total instantaneous heat transfer rate (Q_{ht}) from the cylinder gases to the walls, shown in Figure 4.14, directly reflects the trends observed in heat flux, as $Q_{ht} = q'' \cdot A_s(\theta)$. Consequently, for all four HTC models, the DW simulation results in a higher peak Q_{ht} occurring somewhat later in the cycle compared to the SW simulation. For instance, with the Hohenberg model, the DW peak Q_{ht} is $55.78\,\mathrm{kW}$ versus SW's $45.29\,\mathrm{kW}$; for Woschni, it's $69.50\,\mathrm{kW}$ (DW) compared to $52.72\,\mathrm{kW}$ (SW). This consistent prediction of higher peak heat transfer rates with the DW model reinforces that its more detailed combustion representation, leading to higher and differently phased gas temperatures, results in a more significant (and likely more realistic) estimation of thermal energy lost to the cylinder walls during the high-temperature phases of the cycle.

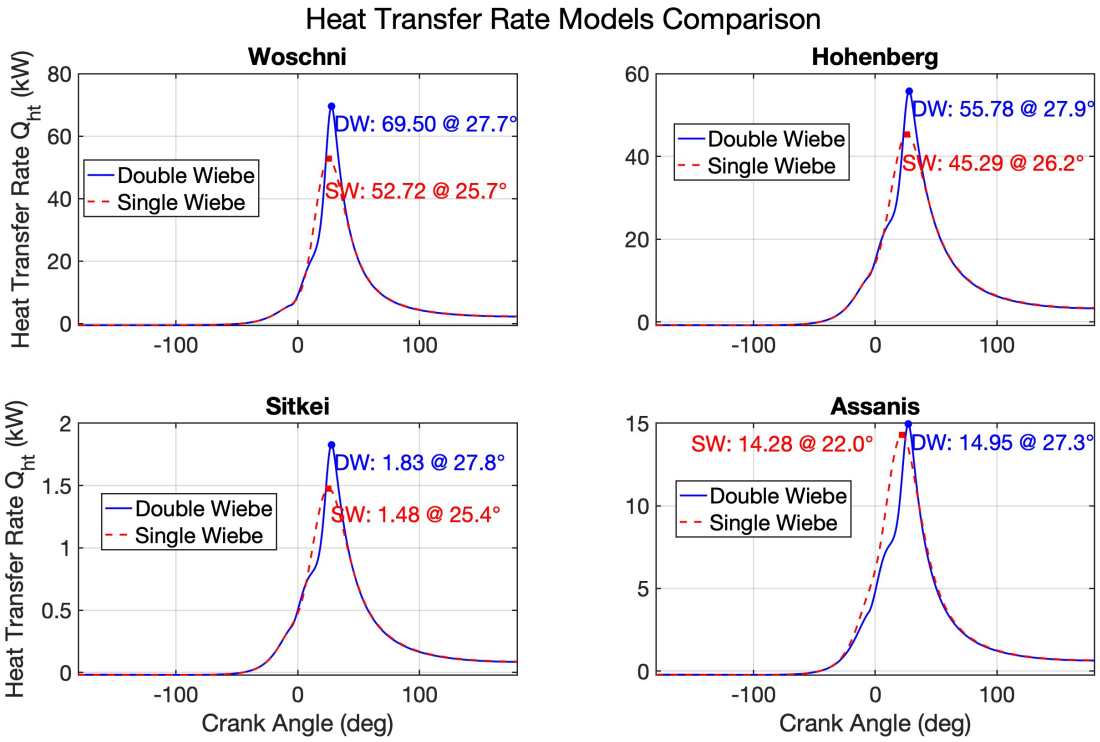

Figure 4.14: Heat Transfer Rate (Q_{ht}) Comparison: Single vs. Double Wiebe, across all four HTC models.

4.2.2. Temperature-dependent Specific Heat Ratio γ

Another improvement explored was to make the ratio of specific heat vary with the temperature in the simulation. Several different models for diesel combustion for γ were explored in a master's thesis by (Li,2017) [47]. It was found that the following simple model by Gatowski et al. has the best accuracy [48]:

$$\gamma(T) = 1.375 - 6.99 * 10^{-5} * T \tag{4.2}$$

Gatowski Model Results Comparison

The following differences were noted when the constant specific heat ratio ($\gamma = 1.3$) was replaced with the temperature-dependent Gatowski model, as described by Equation 4.2.

1. Specific Heat Ratio (γ) Model: The Gatowski equation shows that γ decreases as temperature increases. At lower temperatures (e.g., around 300 K), γ is higher (around 1.354). As temperatures rise significantly during combustion (approaching 2000 K), γ drops to lower values (around 1.23-1.24). This variation contrasts with the constant $\gamma = 1.3$ case.

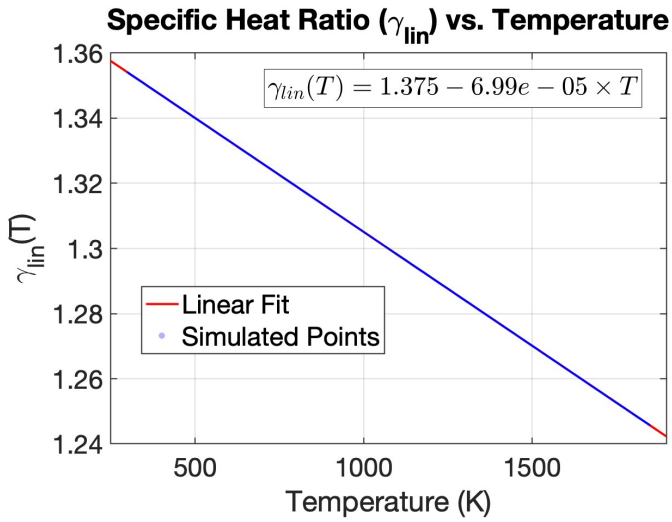

Figure 4.15: Gatowski Model

2. In-Cylinder Pressure and P-V Diagram: The introduction of a varying γ leads to a noticeable increase in peak cylinder pressure (Figure 4.16). The pressure rise appears to be slightly steeper with varying gamma. This higher pressure is reflected in the P-V diagram (Figure 4.17), where the varying gamma case traces a slightly higher loop, particularly around the peak pressure region near Top Dead Center (TDC).

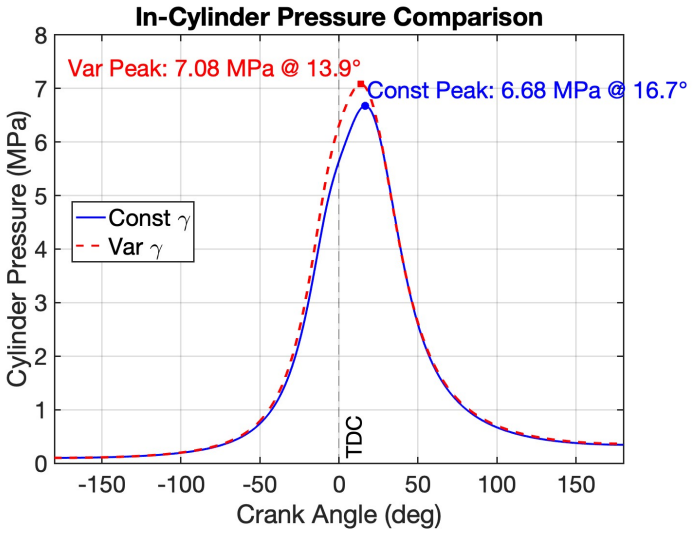

Figure 4.16: In-Cylinder Pressure Comparison

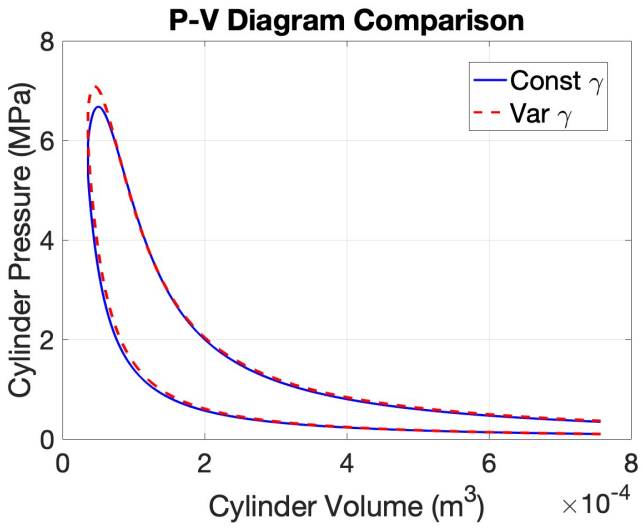

Figure 4.17: P-V Diagram Comparison

3. Cylinder Temperature: Interestingly, despite the higher peak pressure, the peak cylinder temperature is slightly lower with the varying gamma model (Figure 4.18).The temperature profile for the varying gamma case shows higher temperatures during the initial part of combustion and compression, and then slightly lower temperatures during the later part of expansion compared to the constant gamma simulation. This altered temperature profile is a direct consequence of how a temperature-dependent γ (and thus c_v and c_p) influences the energy equation.

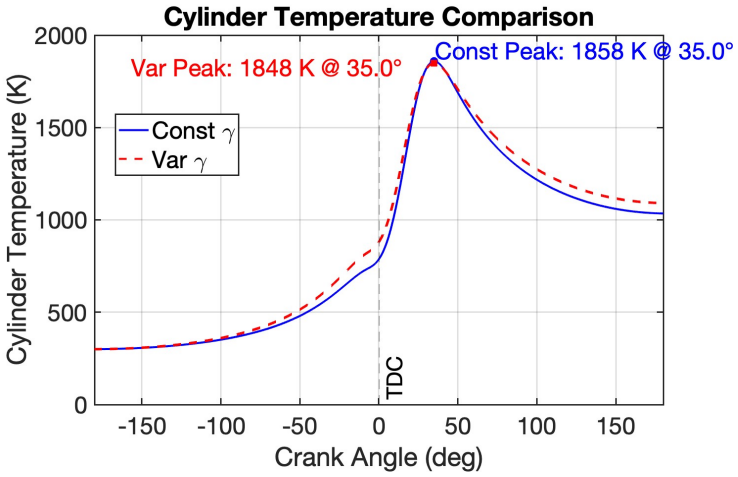

Figure 4.18: Cylinder Temperature Comparison

4. Heat Transfer Characteristics: The differences in pressure and temperature profiles directly impacted the Assanis simulation the most, while the changes in other models of Woschni, Hohenberg and Sitkei were almost negligible. These differences are explained below:

4.1 Assanis Heat Transfer Coefficient (HTC) Comparison (Constant vs. Varying γ):
Figure 4.19 illustrates the Assanis HTC for simulations using a constant γ versus a temperature-dependent $\gamma(T)$. The simulation with constant γ predicts a significantly higher peak Assanis HTC ($621\,\mathrm{W/m^2{-}K}$ at $2.1\,°$CA) compared to the varying $\gamma(T)$ case ($467\,\mathrm{W/m^2{-}K}$ at $0.4\,°$CA). The peak HTC for the varying $\gamma(T)$ case also occurs noticeably earlier. Observing the Assanis HTC formulation in Equation 2.43. The strong negative exponent on temperature (-0.73) makes it highly sensitive to changes in the predicted gas temperature (T_g). Furthermore, the characteristic velocity w_A in the Assanis model includes a term dependent on $(P_{firing} - P_{motoring})$; alterations in the pressure curve due

to $\gamma(T)$ will also influence w_A and thus h_c.

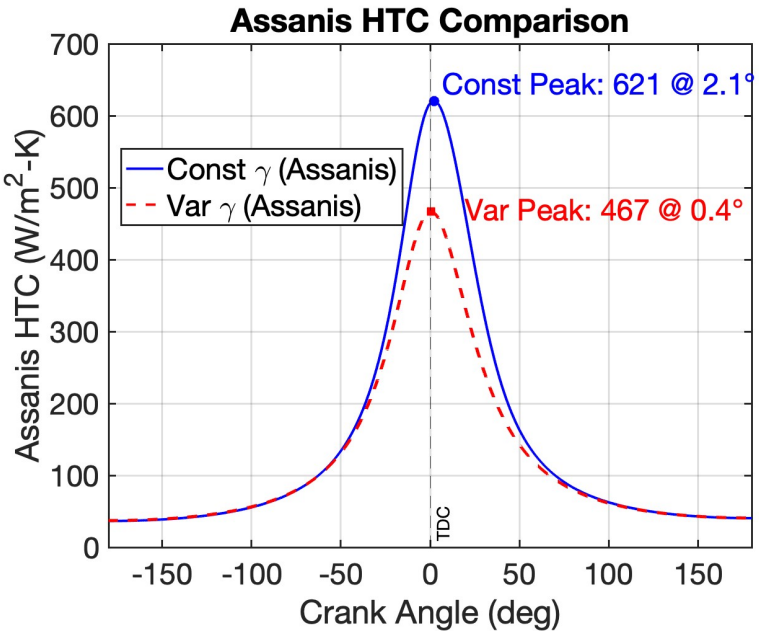

Figure 4.19: Assanis Heat Transfer Coefficient (HTC) Comparison: Constant γ vs. Varying $\gamma(T)$.

4.2 Assanis Heat Flux (q") Comparison (Constant vs. Varying γ):
The wall heat flux (q"), presented in Figure 4.20, largely follows the HTC trend. The constant γ simulation yields a higher peak Assanis q" ($0.47\,\mathrm{MW/m^2}$ at $23.6\,°$CA) than the varying $\gamma(T)$ case ($0.35\,\mathrm{MW/m^2}$ at $22.9\,°$CA). The timing of peak heat flux is also slightly advanced with varying $\gamma(T)$. Since $q'' = h_c(T_g - T_w)$, both the change in h_c and any modifications to the T_g profile due to $\gamma(T)$ contribute to this difference. The lower h_c from the varying $\gamma(T)$ case appears to be the dominant factor in reducing peak q''.

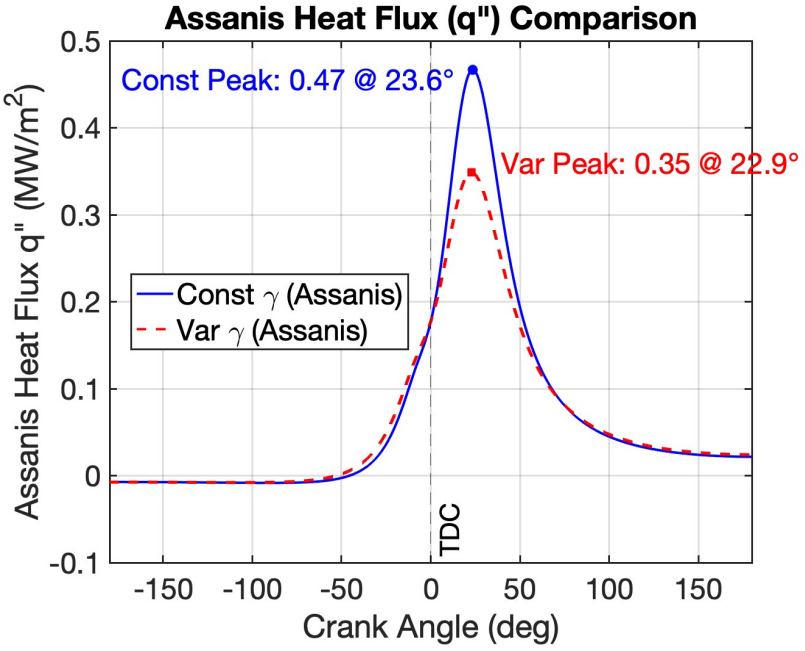

Figure 4.20: Assanis Heat Flux (q") Comparison: Constant γ vs. Varying $\gamma(T)$.

4.3 Assanis Heat Transfer Rate (Q_{ht}) Comparison (Constant vs. Varying γ):
The total heat transfer rate (Q_{ht}) in Figure 4.21 shows a twist. The varying $\gamma(T)$ simulation has a slightly higher peak Q_{ht} ($14.4\,\mathrm{kW}$ at $21.5\,°\mathrm{CA}$) than the constant γ one ($13.9\,\mathrm{kW}$ at $23.6\,°\mathrm{CA}$), and it peaks earlier. This happens because Q_{ht} depends not just on the heat transfer coefficient (h_c), but also on the gas temperature (T_g) and the changing surface area (A_s). Even if peak h_c is lower, if the T_g profile and A_s combine favourably at a certain point, the overall Q_{ht} can be higher then.

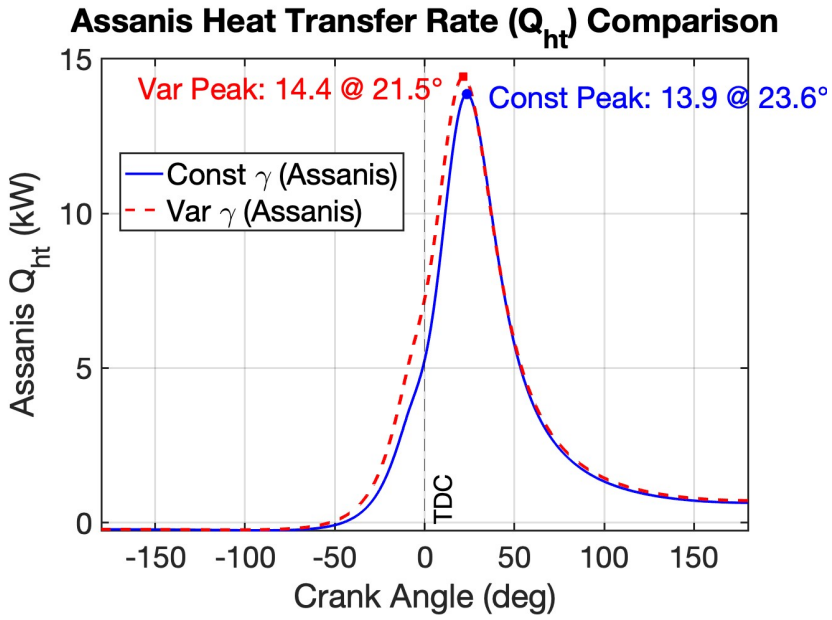

Figure 4.21: Assanis Heat Transfer Rate (Q_{ht}) Comparison: Constant γ vs. Varying $\gamma(T)$.

4.2.3. Specific Gas Constant R for Exhaust Products

The standard specific gas constant for air may not fully represent diesel engine exhaust. Using exhaust gas molar concentrations from stoichiometric calculations (CO_2: $7.46\,\%$, H_2O: $7.15\,\%$, O_2: $9.20\,\%$, N_2: $76.16\,\%$; Section 3.2.6), a composition-specific gas constant (R) was determined. The average molar mass (M_{mix}) of the exhaust products was first calculated:

$$\begin{aligned} M_{\text{mix}} &= (0.0746 \times 44.01\,\mathrm{g\,mol^{-1}}) + (0.0715 \times 18.02\,\mathrm{g\,mol^{-1}}) \\ &\quad + (0.0920 \times 32.00\,\mathrm{g\,mol^{-1}}) + (0.7616 \times 28.02\,\mathrm{g\,mol^{-1}}) \\ &= 28.855\,\mathrm{g\,mol^{-1}} = 0.0288\,\mathrm{kg\,mol^{-1}}. \end{aligned}$$

The specific gas constant was then found using the universal gas constant ($\bar{R} = 8.314\,\mathrm{J\,mol^{-1}\,K^{-1}}$):

$$R = \frac{\bar{R}}{M_{\text{mix}}} = \frac{8.314\,\mathrm{J\,mol^{-1}\,K^{-1}}}{0.0288\,\mathrm{kg\,mol^{-1}}} \approx 0.2881\,\mathrm{kJ\,kg^{-1}\,K^{-1}}. \tag{4.3}$$

This value of $R = 0.2881\,\mathrm{kJ\,kg^{-1}\,K^{-1}}$ was then used in simulations.

Impact on Simulation Results: Comparing simulations using this exhaust-product R against a standard air value revealed minimal differences in key engine performance metrics. The overall work, peak pressure characteristics, peak temperature, and efficiency remained virtually unchanged. Only a minor change in volumetric efficiency was noted: from $105.3\,\%$ for $R = 0.2869\,\mathrm{kJ\,kg^{-1}\,K^{-1}}$ to $105.75\,\%$ for $R = 0.2881\,\mathrm{kJ\,kg^{-1}\,K^{-1}}$.

5

Application and Evaluation of the 0D Thermodynamic Model for Hydrogen Combustion

5.1. Introduction: Rationale for Hydrogen Engine Simulation

The developed diesel engine model's performance was established by the discussion in Chapter 4. That chapter validated the model's ability to accurately reproduce important in-cylinder features, particularly the pressure evolution and heat release patterns typical of diesel combustion, by comparing it with published experimental data. This chapter expands the model's use to simulate a hydrogen-fuelled spark-ignition (SI) engine.

There is a growing interest in renewable fuels such as hydrogen for ICE. Current research highlights the importance of reliable hydrogen ICE simulation tools. For example, a life cycle assessment of hydrogen in shipping was carried out by Ventayol et al. [49], who discovered that hydrogen-fuelled ICE that use green hydrogen can offer a suitable decarbonisation pathway, possibly providing lifecycle and carbon emissions advantages over hydrogen fuel cells in such applications. This underscores the significance of understanding hydrogen ICE behaviour.

The primary objectives herein are:

- To configure the 0D model for a hydrogen SI engine using a baseline experimental dataset (Dataset 1), including tuning Wiebe combustion parameters (θ_s, θ_d, a, n) to match observed engine behaviour.
- To assess the performance of selected heat transfer correlations (Woschni, Hohenberg, Sitkei, Assanis) with this tuned hydrogen model.
- To evaluate the model's predictive capability against three additional experimental datasets (Datasets 2, 3, and 4) from the same hydrogen engine but under different operating conditions. For these cases, fundamental engine parameters (CR, γ, BDC conditions, λ, target heat release) are updated to match each dataset, while the Wiebe shape factors (a, n) and duration (θ_d) are kept from the Dataset 1 tuning. The start of combustion (θ_s) is adjusted as per each dataset's specific ignition timing.
- To conduct a sensitivity analysis of the hydrogen simulation to variations in the Wiebe parameters.
- To qualitatively compare in-cylinder phenomena predicted for hydrogen SI operation against those from the diesel CI simulation, acknowledging the differing engine platforms.

It is important to note that the experimental datasets for this hydrogen SI engine simulation originate from a different engine platform than that used for the primary diesel model validation. Thus, direct

quantitative comparison of overall engine performance metrics between the diesel and hydrogen simulations is influenced by these differing engine architectures.

5.2. Hydrogen Engine Model Configuration and Initial Experimental Benchmark (Dataset 1)

The hydrogen simulation was initially configured to replicate a single-cylinder research SI engine at a particular operating point of Dataset 1. This served to test the adaptability of key concepts from the diesel model to hydrogen, such as the Wiebe combustion model and the set of heat transfer correlations.

5.2.1. Experimental Benchmark and Operating Conditions (Dataset 1)

The initial benchmark for configuring and validating the hydrogen simulation was Dataset 1. For this operating point, the SI engine ran at approximately $1500\,\mathrm{RPM}$ with a lean air-fuel mixture, characterised by a global lambda (λ) value of 3.245. Key valve timings for the modelled closed cycle were an intake valve closing (IVC) at 224 °CA (intake) and exhaust valve opening (EVO) at 500 °CA. Initial conditions at BDC for the simulation were set to a pressure (P_{bdc}) of $166.45\,\mathrm{kPa}$ and a temperature (T_{bdc}) of $320.37\,\mathrm{K}$, based on this experimental dataset.

5.2.2. Model Adaptation and Parameterization for Hydrogen (Dataset 1)

Adapting the simulation framework from diesel to hydrogen operation for Dataset 1 involved several key modifications.

Engine Geometry:

The model was configured with the geometric specifications of the experimental SI engine used for the hydrogen tests. These are detailed in Table 5.1.

Table 5.1: Geometric Specifications of the Experimental Hydrogen SI Engine

Parameter	Value	Unit
Bore (B)	0.17	m
Stroke (S)	0.18	m
Connecting Rod Length (l)	0.34	m
Displacement Volume (V_{disp})	4.084×10^{-3}	m^3

The compression ratio for Dataset 1 was $r = 10.84$. This ratio is slightly different for experimental datasets 2, 3, and 4.

Fuel Properties (Dataset 1):

Hydrogen was defined as the fuel, with its Lower Heating Value (LHV) set to $120 \times 10^6\,\mathrm{J\,kg^{-1}}$. The mass of hydrogen per cycle ($m_{f,H2}$) was derived from the reported experimental total in-cylinder charge mass of $7.899 \times 10^{-3}\,\mathrm{kg}$ and the target lambda of 3.245, resulting in an $m_{f,H2}$ of approximately $6.929 \times 10^{-5}\,\mathrm{kg}$. The total effective heat input for the Wiebe combustion model was specified as $7155.0\,\mathrm{J}$ per cycle, aligning with the net energy release characteristics of the experimental point.

A constant value of 1.3492 for the specific heat ratio γ was used in this hydrogen simulation. This choice was made due to the limited availability in literature about temperature-dependent γ models specifically valid for hydrogen-fuelled engines. The chosen value is an estimated average that takes into account the variation of γ between the hydrogen experiment's peak combustion temperatures and intake conditions.

It is important to note that the target lambda, heat input and specific heat ratio and was slightly different for datasets 2, 3 and 4, as detailed in Table 5.3.

Mixture Properties and Estimated Combustion Product Composition (Dataset 1):
The composition of the primary combustion products was estimated for the hydrogen simulation under lean conditions (Dataset 1: $\lambda \approx 3.245$) in order to determine average mixture properties, such as the specific gas constant R_{mix}. This required a stoichiometric analysis with the estimated excess air, assuming a complete combustion of hydrogen (H_2).

The methodology included balancing the stoichiometric combustion equation for hydrogen and then adjusting for the actual air supplied based on λ. This yielded the primary products: water vapor (H_2O), unreacted (excess) oxygen (O_2), and nitrogen (N_2). The detailed balancing steps, calculation of molar fractions, and determination of the average molar mass of the product mixture ($M_{mix,prod}$) are provided in Section B.3 in Appendix B.

For Dataset 1, the estimated molar composition of the products is approximately: $H_2O \approx 12.16\%$, excess $O_2 \approx 13.65\%$, and $N_2 \approx 74.19\%$. This composition results in an average product molar mass ($M_{mix,prod}$) of approximately $27.341\,\mathrm{g\,mol^{-1}}$. This value, differing significantly from diesel exhaust due to the absence of carbon and high excess air, is crucial for deriving the mixture-specific gas constant R_{mix} used in subsequent thermodynamic calculations for this dataset. For other datasets (2, 3, and 4) with slightly different λ values, $M_{mix,prod}$ and R_{mix} were calculated following the same methodology, yielding very similar results due to the consistently lean operation.

Mixture Specific Gas Constant (R_{mix}) for Hydrogen Simulation (Dataset 1):
For the hydrogen simulation, a mixture-specific gas constant (R_{mix}) is needed for thermodynamic calculations like the derivation of specific heats and the ideal gas law ($PV = mR_{mix}T$). Below is the calculation for dataset 1 as an example. This value depends on the composition of the in-cylinder air-fuel mixture.

R_{mix} can be determined from the composition of the combustion products, using their average molar mass ($M_{mix,prod}$) calculated in Section 5.2.2 and the universal gas constant ($\bar{R} \approx 8.314\,46\,\mathrm{J\,mol^{-1}\,K^{-1}}$ or $8314.46\,\mathrm{J\,kmol^{-1}\,K^{-1}}$):

$$R_{mix} = \frac{\bar{R}}{M_{mix,prod}} = \frac{8314.46\,\mathrm{J\,kmol^{-1}\,K^{-1}}}{27.341\,\mathrm{kg\,kmol^{-1}}} \approx 304.09\,\mathrm{J\,kg^{-1}\,K^{-1}} \approx 0.3041\,\mathrm{kJ\,kg^{-1}\,K^{-1}} \tag{5.1}$$

This value reflects the properties of the gaseous mixture consisting primarily of H_2O, excess O_2, and N_2.

Combustion Model Parameterization (Dataset 1):
The single-zone Wiebe function was used for hydrogen fuel simulation given its simplicity, computational efficiency, and the ability to capture the overall energy release profile with a limited number of tunable parameters, which is advantageous when multi-zone combustion data is unavailable. An iterative process of fine-tuning the Wiebe parameters, like the start of combustion (θ_s), the combustion duration (θ_d), and the shape factors 'a' and 'n', was done to accurately capture the unique combustion behaviour of hydrogen. The initial estimates for these parameters were informed by the known rapid burning nature of hydrogen.

The primary objective of this tuning was to ensure close agreement between the simulation output and the experimentally derived data for four critical indicators:

1. The Average Rate of Heat Release (aROHR) profile,
2. The rate of pressure rise (dp/dθ),
3. The in-cylinder pressure trace ($P(\theta)$)
4. The cumulative heat release curve.

This multi-faceted comparison ensured a more holistic validation of the combustion and energy release dynamics. Through this iterative refinement procedure, the Wiebe parameters selected for the hydrogen simulation were $\theta_s = -20\,^\circ$CA, $\theta_d = 40\,^\circ$CA, $a = 4$, and $n = 3$.

Heat Transfer Correlations:
The hydrogen simulation was conducted using the same set of empirical heat transfer correlations (Woschni, Hohenberg, Sitkei, and Assanis) that were used and verified in the context of the diesel engine model (Chapter 4). This approach was deliberately chosen to assess these correlations' performance and sensitivity when subjected to the significantly different thermal environment and working fluid properties associated with hydrogen combustion. The cylinder wall temperature for these calculations was set to an average value of approximately $446\,\mathrm{K}$, derived from experimental temperature measurements of the cylinder head, piston crown, and liner temperatures, and implemented via a wall temperature factor ($t_w = 1.393$) relative to T_{bdc}.

5.2.3. Validation of Hydrogen Simulation Against Experimental Data

The configured hydrogen engine model, utilising the Hohenberg correlation as an example, was then run, and its outputs were compared against the experimental benchmark data to assess its predictive capability. A comprehensive comparison of key performance metrics between the simulation and experimental results for the hydrogen-fuelled engine operating between intake IVC and EVO is shown in Figure 5.1.

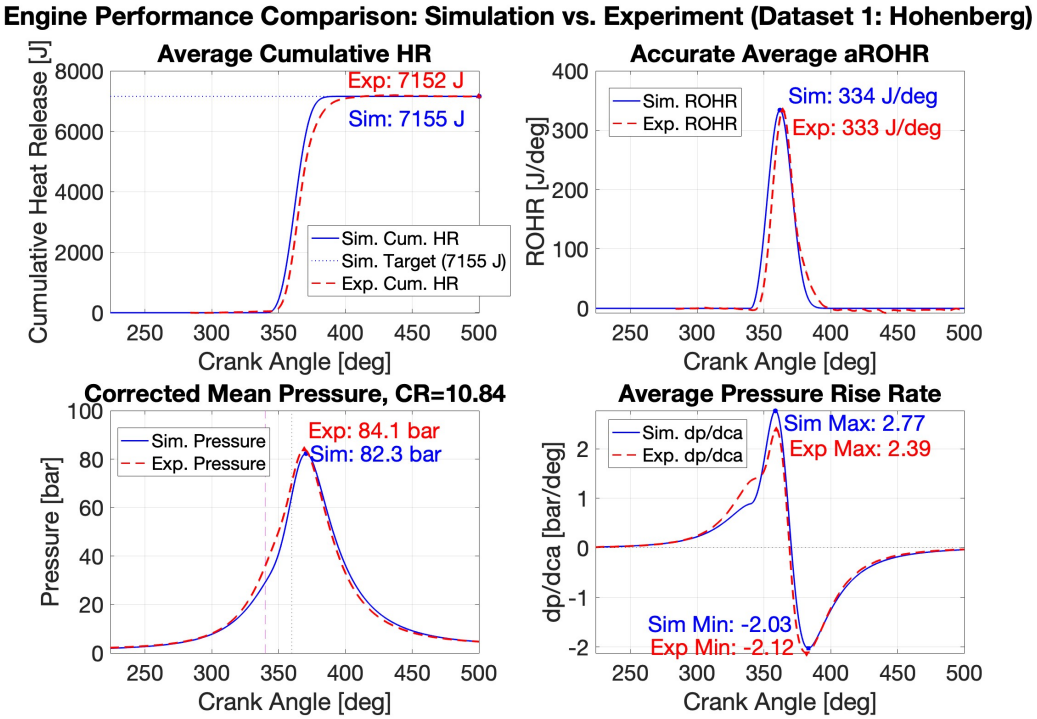

Figure 5.1: Engine Performance Comparison: Hydrogen Simulation (with Hohenberg HTC model) vs. Experiment

Presentation and Discussion of Results
Observing Figure 5.1, several key comparisons can be made:

- **Cumulative Heat Release (Top-Left):** With the simulation achieving a total of $7155\,\mathrm{J}$ versus the experimental value of $7152\,\mathrm{J}$, the simulated average cumulative heat release closely resembles the experimental curve. This indicates that the overall energy input and the total energy accounted for by the Wiebe function in the simulation are well-matched to the experiment.
- **Average Rate of Heat Release (aROHR) (Top-Right):** The experimental aROHR and the simulated aROHR profile agree well, especially when it comes to peak timing and magnitude. The experimental peak of $333\,\mathrm{J/°CA}$ closely resembles the peak aROHR predicted by the simulation, which is $334\,\mathrm{J/°CA}$. The overall shape and duration of the heat release event are also well captured, indicating that the bulk combustion process of hydrogen under these conditions is ef-

fectively represented by the tuned Wiebe function parameters ($a = 4, n = 3, \theta_s = -20\,°\text{CA}, \theta_d = 40\,°\text{CA}$).

- **In-Cylinder Pressure (Bottom-Left):** There is a significant correlation between the experimental pressure data and the simulated in-cylinder pressure trace. The corrected mean peak pressure for the simulation is $82.3\,\text{bar}$, which is very close to the experimental peak of $84.1\,\text{bar}$. The phasing of the pressure rise and the overall curve shape throughout the compression and expansion strokes are well replicated.
- **Rate of Pressure Rise (dp/dca) (Bottom-Right):** The model's performance is further supported by the comparison of the rate of pressure rise. The simulation predicts a maximum pressure rise rate of $2.77\,\text{bar}/°\text{CA}$, while the experiment shows a maximum of $2.39\,\text{bar}/°\text{CA}$. While the simulated peak is slightly higher and occurs marginally earlier, the overall profile, including the negative peak during expansion (Sim Min: $-2.03\,\text{bar}/°\text{CA}$ vs. Exp Min: $-2.12\,\text{bar}/°\text{CA}$), is quite similar.

5.2.4. Influence of Heat Transfer Correlation on Predicted Hydrogen Engine Performance

As established in Section 5.2.3, the hydrogen simulation, particularly when employing the Hohenberg heat transfer model, demonstrated a strong visual correspondence with experimental in-cylinder pressure and derived heat release data. To further investigate the sensitivity of overall engine performance predictions to the heat transfer correlation, the hydrogen simulation was executed independently with each of the four implemented correlations: Woschni, Hohenberg, Sitkei, and Assanis. All other simulation parameters, including engine geometry, initial conditions, total fuel energy input, and the Wiebe combustion parameters ($\theta_s = -20\,°\text{CA}$, $\theta_d = 40\,°\text{CA}$, $a = 4$, $n = 3$), were held constant.

While the dynamic traces of in-cylinder pressure, aROHR, and cumulative heat release showed considerable visual similarity across the models (representative plots in Appendix A), significant divergences emerged in the integrated performance metrics and energy balance, as summarised in Table 5.2.

Table 5.2: Predicted Hydrogen Engine Performance and Energy Balance: Impact of Different Heat Transfer Correlations

Parameter	Sitkei	Assanis	Woschni	Hohenberg
Total Heat Loss (J)	11.85	103.61	361.17	456.61
Net Work Output (J)	3983.48	3971.32	3937.48	3929.22
Internal Energy Change (End-Start, J)	3165.57	3151.96	3113.89	3101.84
Thermal Efficiency (%)	55.67	55.50	55.03	54.92
IMEP (Net, bar)	9.75	9.72	9.64	9.62

Common Input: Total Actual Heat Release (Wiebe) = $7155.00\,\text{J}$

With a constant combustion energy input of $7155\,\text{J}$, the predicted total heat losses varied dramatically, from only $11.85\,\text{J}$ with Sitkei to $456.61\,\text{J}$ with Hohenberg. These variations directly impact net work output and thermal efficiency, with Sitkei yielding the highest ($3983.48\,\text{J}$ work, $55.67\,\%$ efficiency) and Hohenberg the lowest ($3929.22\,\text{J}$ work, $54.92\,\%$ efficiency). These discrepancies arise from the unique empirical formulations of each correlation. The first law energy balance ($Q_{\text{in}} \approx W_{\text{out}} + Q_{\text{loss}} + \Delta U$) shows Sitkei achieving the closest numerical closure ($\sum \approx 7161\,\text{J}$), followed by Assanis ($\sum \approx 7227\,\text{J}$), while Woschni and Hohenberg exhibit larger deviations ($\sum \approx 7413\,\text{J}$ and $\sum \approx 7488\,\text{J}$ respectively), indicating greater accumulated numerical effects with these latter models under hydrogen conditions.

To assess which correlation provides the most applicable predictions for this hydrogen engine case, the simulated results are compared against available experimental targets: a mean in-cylinder heat loss of approximately $345.0\,\text{J}$, a mean IMEP around $8.2\,\text{bar}$, and a mean total actual work done per cycle of $3349.0\,\text{J}$.

Comparing these experimental targets with the simulation outputs:

- **Total Heat Loss (Experimental Target $\approx 345\,\mathrm{J}$):**
  - Woschni: $361.17\,\mathrm{J}$ (Difference: $16.2\,\mathrm{J}$, or +4.7%)
  - Hohenberg: $456.61\,\mathrm{J}$ (Difference: $111.6\,\mathrm{J}$, or +32.4%)
  - Sitkei: $11.85\,\mathrm{J}$ (Difference: $-333.1\,\mathrm{J}$, or -96.5%)
  - Assanis: $103.61\,\mathrm{J}$ (Difference: $-241.4\,\mathrm{J}$, or -69.9%)

  The **Woschni** correlation provides the closest prediction of heat loss.
- **Net Work Output (Experimental Target $\approx 3349\,\mathrm{J}$):**
  - Woschni: $3937.48\,\mathrm{J}$ (Difference: $588.5\,\mathrm{J}$, or +17.6%)
  - Hohenberg: $3929.22\,\mathrm{J}$ (Difference: $580.2\,\mathrm{J}$, or +17.3%)
  - Sitkei: $3983.48\,\mathrm{J}$ (Difference: $634.5\,\mathrm{J}$, or +19.0%)
  - Assanis: $3971.32\,\mathrm{J}$ (Difference: $622.3\,\mathrm{J}$, or +18.6%)

  All models significantly overestimate the net work output. The Woschni and Hohenberg models, while still high, are marginally closer to the experimental work value than Sitkei and Assanis.
- **IMEP (Experimental Target $\approx 8.2\,\mathrm{bar}$):**
  - Woschni: $9.64\,\mathrm{bar}$ (Difference: $1.44\,\mathrm{bar}$, or +17.6%)
  - Hohenberg: $9.62\,\mathrm{bar}$ (Difference: $1.42\,\mathrm{bar}$, or +17.3%)
  - Sitkei: $9.75\,\mathrm{bar}$ (Difference: $1.55\,\mathrm{bar}$, or +18.9%)
  - Assanis: $9.72\,\mathrm{bar}$ (Difference: $1.52\,\mathrm{bar}$, or +18.5%)

  Consistent with the work output, all models overestimate IMEP. Again, Woschni and Hohenberg show slightly less overestimation.

Considering these three key experimental targets for the hydrogen engine: The **Woschni correlation** demonstrates the best agreement for *Total Heat Loss*, predicting a value very close to the experimental target. While all models overestimate *Net Work Output* and consequently *IMEP*, the Woschni and Hohenberg models show a somewhat smaller degree of overestimation compared to Sitkei and Assanis. The significant underestimation of heat loss by Sitkei and Assanis directly contributes to their higher predicted work and IMEP values, moving them further from the experimental work and IMEP targets. The Hohenberg model, despite its good visual agreement for pressure traces (Section 5.2.3), substantially overpredicts heat loss and also overestimates work/IMEP.

Thus, among the four models tested, the Woschni correlation seems to provide the most balanced and accurately representative predictions for this particular hydrogen engine operating condition based on this multi-parameter comparison against experimental targets for heat loss, work output, and IMEP. The general overestimation of work and IMEP by all models suggests that other factors not fully captured by the current 0D simulation (such as actual combustion inefficiencies beyond the idealised Wiebe heat release, cycle-to-cycle variations, or other unmodelled losses present in the experimental engine) likely contribute to the discrepancy between simulated and measured work output.

5.2.5. Hydrogen Engine Operating Conditions for Evaluated Datasets

The evaluation of the hydrogen SI engine model utilised four distinct experimental datasets, each representing a different operating point of the same research engine. While the fundamental engine geometry (Table 5.1) and certain simulation constants (e.g., Wiebe shape factors $a = 4, n = 3$; combustion duration $\theta_d = 40\,^\circ$CA; Woschni heat transfer correlation) were maintained across these datasets after initial tuning with Dataset 1, several key operational and thermodynamic parameters were adjusted for each case to match the specific experimental conditions.

A crucial modification for every dataset was the Start of Combustion (θ_s), which represents the timing of ignition in an SI engine. Since optimal ignition timing varies depending on engine operating conditions (e.g., load, speed, mixture strength), this parameter was set specifically for each dataset to reflect the engine timing used in that experiment. Other parameters that varied for each dataset included the Compression Ratio (CR), which exhibited minor experimental variations; the initial conditions at BDC (P_{BDC}, T_{BDC}), the target net heat release (Q_{in}), and the average specific heat ratio (γ). The air-fuel equivalence ratio (λ) also differed for each dataset, necessitating a recalculation of the mixture-specific gas constant (R_{mix}) and, consequently, the specific heats (c_p, c_v) for each case, following the stoichiometric methodology detailed for Dataset 1 (Section 5.2.2).

Table 5.3 summarises these key distinguishing input parameters for the four hydrogen experimental datasets.

Table 5.3: Key Varied Input Parameters for Hydrogen Experimental Datasets (Simulated with Fixed Wiebe Shape $a = 4, n = 3, \theta_d = 40\,^\circ$CA and Woschni HTC)

Parameter	Dataset 1	Dataset 2	Dataset 3	Dataset 4
Start of Combustion, θ_s (°CA)	-20.0000	-18.0000	-16.0000	-14.0000
Compression Ratio, CR	10.8400	10.7900	10.7700	10.7700
Air-Fuel Equiv. Ratio, λ	3.2450	3.2455	3.2627	3.2381
Avg. Specific Heat Ratio, γ	1.3492	1.3507	1.3524	1.3542
P_{BDC} (kPa)	166.4500	167.8970	168.8620	168.4090
T_{BDC} (K)	320.3659	320.3617	320.3126	320.4114
Target Net Heat Release, Q_{in} (J)	7155.0000	7198.7300	7234.1300	7220.6700
Derived R_{mix} (kJ/kgK)	0.3041	0.3041	0.3043	0.3040

Note: For all datasets, the engine geometry (Bore $0.17\,\mathrm{m}$, Stroke $0.18\,\mathrm{m}$), engine speed ($\approx 1500\,\mathrm{RPM}$), total in-cylinder mass ($\approx 7.90 \times 10^{-3}\,\mathrm{kg}$), and wall temperature ($\approx 446.3\,\mathrm{K}$) were kept consistent, reflecting the common experimental engine platform.

5.2.6. Comparative Results for Additional Hydrogen Datasets

This subsection presents and discusses the comparison between simulation predictions (using fixed Wiebe shape parameters a, n, θ_d and the Woschni HTC model) and the experimental data for Datasets 2, 3, and 4. Each dataset comparison includes plots of average cumulative heat release, aROHR, corrected mean pressure, and average pressure rise rate.

Dataset 1 Comparison with Woschni HTC Model:

Before proceeding to the other datasets, Figure 5.2 presents the simulation results for Dataset 1 using the selected Woschni heat transfer correlation, compared against the experimental data. This serves as a baseline for the fixed Wiebe shape parameter evaluations.

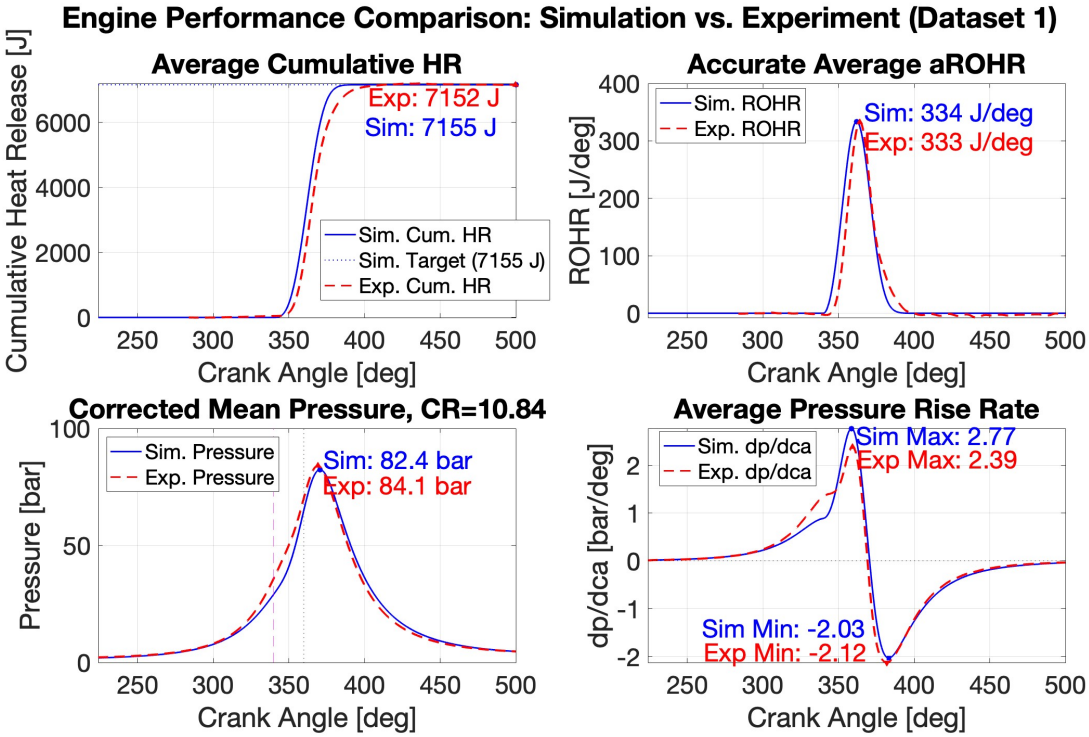

Figure 5.2: Performance Comparison: Hydrogen Simulation (Tuned Wiebe Shape, Woschni HTC) vs. Experimental Dataset 1.

Comparison with Experimental Dataset 2:

The differences can be seen in Figure 5.3. For Dataset 2, the simulated peak pressure reached $72.3\,\mathrm{bar}$ and slightly underpredicts the experimental peak of $73.5\,\mathrm{bar}$. The phasing of the pressure rise and peak pressure, however, shows good alignment. Though the simulation displays a slightly narrower aROHR profile, the simulated peak aROHR is $304\,\mathrm{J/°CA}$, closely matches the experimental $292\,\mathrm{J/°CA}$. The cumulative heat release matches the target Q_{in} of $7199\,\mathrm{J}$. The maximum rate of pressure rise (dp/dCA) is simulated at $1.91\,\mathrm{bar/°CA}$, higher than the experimental maximum of $1.54\,\mathrm{bar/°CA}$, suggesting a somewhat faster initial burn in the simulation than observed experimentally for this condition. The simulated IMEP was $9.60\,\mathrm{bar}$ compared to an experimental target of $8.06\,\mathrm{bar}$.

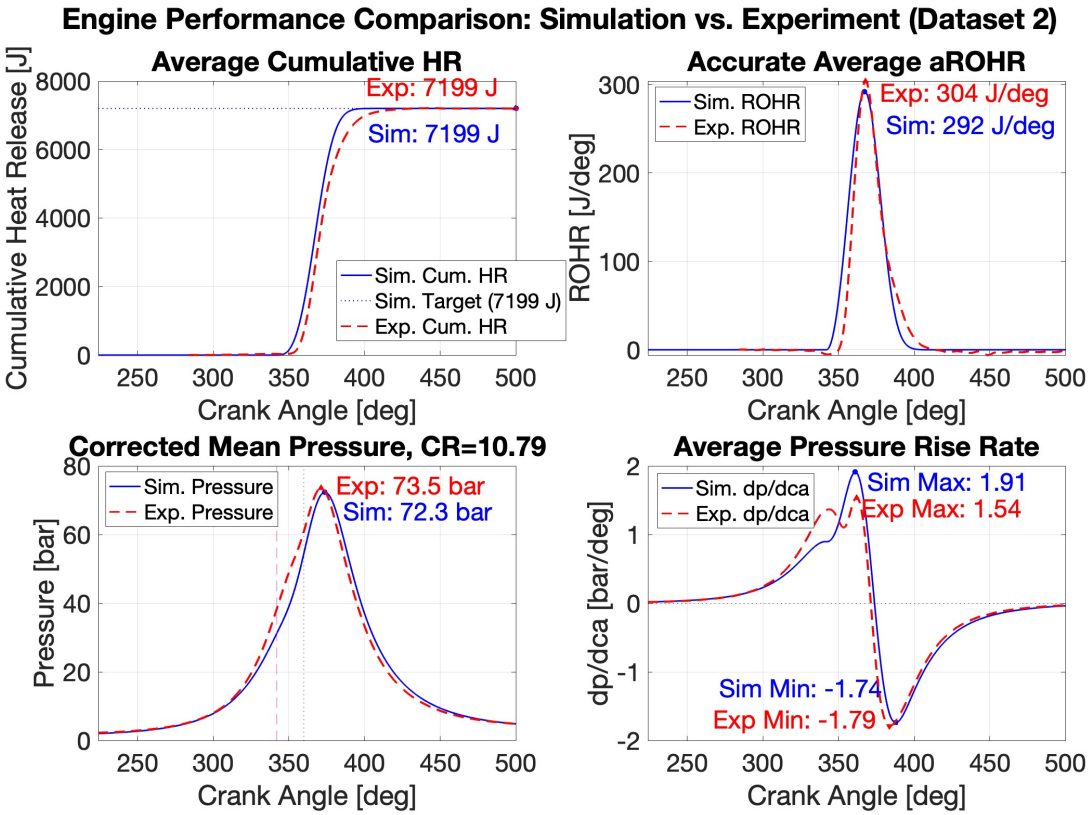

Figure 5.3: Performance Comparison: Hydrogen Simulation (Fixed Wiebe Shape, Woschni HTC) vs. Experimental Dataset 2.

Comparison with Experimental Dataset 3:
The simulation results are compared to experimental data in Figure 5.4. For Dataset 3, the simulated peak pressure ($61.0\,\mathrm{bar}$) closely matches the experimental value ($61.3\,\mathrm{bar}$), and the aROHR profiles show reasonable agreement in peak magnitude (Sim: $250\,\mathrm{J/°CA}$ vs. Exp: $266\,\mathrm{J/°CA}$) and general form. Cumulative heat release aligns with the target Q_{in} ($7234\,\mathrm{J}$). However, the simulated maximum rate of pressure rise (dp/dCA) is $1.09\,\mathrm{bar/°CA}$, notably lower than the experimental peak of $1.37\,\mathrm{bar/°CA}$. Furthermore, the shape of the experimental dp/dCA curve for Dataset 3 exhibits a sharper, more defined initial peak, whereas the simulation produces a somewhat broader, less intense rise. This suggests that the fixed Wiebe shape parameters may not fully capture the initial rapid flame development characteristic of this specific operating point. The simulated IMEP was $9.40\,\mathrm{bar}$ against an experimental target of $7.76\,\mathrm{bar}$.

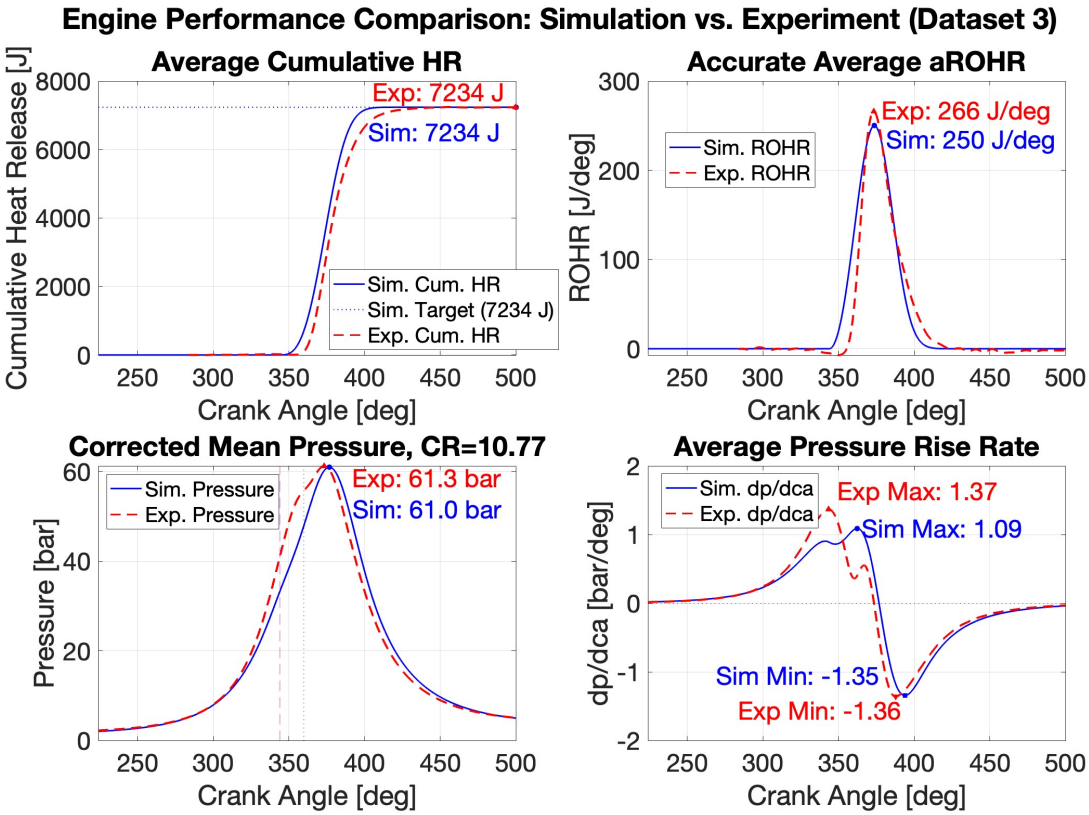

Figure 5.4: Performance Comparison: Hydrogen Simulation (Fixed Wiebe Shape, Woschni HTC) vs. Experimental Dataset 3.

Comparison with Experimental Dataset 4:

For Dataset 4, the simulation versus experimental comparison is presented in Figure 5.5. The plot demonstrates good agreement in peak pressure (Sim: $55.3\,\mathrm{bar}$ vs. Exp: $55.4\,\mathrm{bar}$) and good alignment in aROHR profiles (Sim peak: $236\,\mathrm{J/°CA}$ vs. Exp. peak: $227\,\mathrm{J/°CA}$). Cumulative heat release correctly matches the target Q_{in} ($7221\,\mathrm{J}$). Similar to Dataset 3, the simulated maximum dp/dCA ($0.91\,\mathrm{bar/°CA}$) is again lower than the experimental value ($1.35\,\mathrm{bar/°CA}$). Additionally, Dataset 4's experimental dp/dCA curve shows a clear, sharp initial peak that is less noticeable and more rounded in the simulation. This persistent variation in the initial dp/dCA profile between Datasets 3 and 4 suggests that the fixed Wiebe shape parameters are not very effective at accurately capturing the early phases of combustion in these different circumstances.

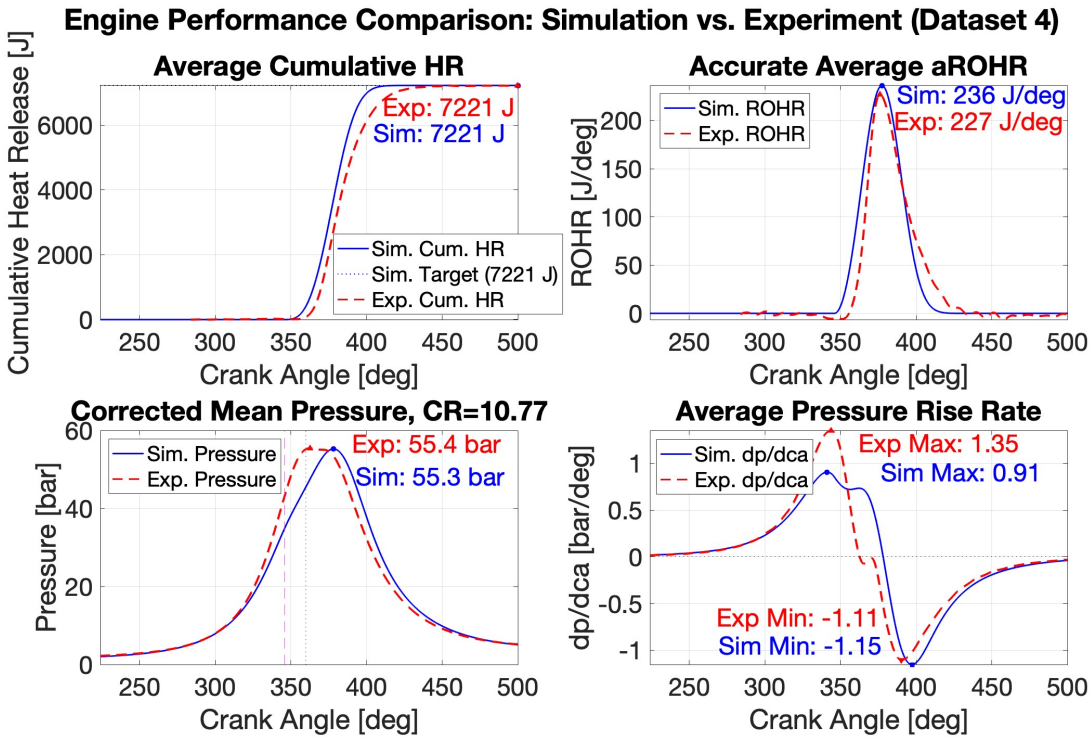

Figure 5.5: Performance Comparison: Hydrogen Simulation (Fixed Wiebe Shape, Woschni HTC) vs. Experimental Dataset 4.

5.2.7. Discussion of Model Performance Across Additional Datasets

For this hydrogen SI engine, the evaluation across Datasets 2, 3, and 4 using fixed Wiebe shape parameters (a, n, θ_d) tuned for Dataset 1 and the Woschni heat transfer model offers insights into the model's capabilities.

Overall, by modifying the start of combustion (θ_s) and basic thermodynamic inputs (CR, λ, P_{BDC}, T_{BDC}, Q_{in}, average γ), the model showed an acceptable ability to capture the general trends and magnitudes of in-cylinder pressure and aROHR across these varied operating conditions. Predicted peak pressure was mostly in agreement with experimental values, especially for Datasets 3 and 4. Overall, the aROHR's shape and magnitude were also fairly well represented, suggesting that, with proper ignition timing, the fixed Wiebe shape parameters ($a = 4, n = 3$) and duration ($\theta_d = 40°$) offer a reasonable approximation of the hydrogen burn profile across these lean conditions.

However, there were continued variations between the indicated mean effective pressure (IMEP) and the predicted rate of pressure rise (dp/dCA). In comparison to the experiment, the simulation tended to predict a different peak dp/dCA for Datasets 2, 3, and 4, with Dataset 2 showing a higher peak and Datasets 3 and 4 showing a lower peak. This implies that even though the total energy and burn time are equal, the fixed Wiebe shape may not accurately depict the intricate details of the initial flame development and propagation under all tested circumstances, which have a significant impact on the maximum pressure rise rate.

Furthermore, a systematic overestimation of IMEP (and consequently, net work output and thermal efficiency) was observed for all three additional datasets, similar to the trend seen with Dataset 1.

- Dataset 1 (Woschni): Sim. IMEP $9.64\,\mathrm{bar}$ vs. Exp. Target $8.22\,\mathrm{bar}$ (+$17.3\,\%$)
- Dataset 2 (Woschni): Sim. IMEP $9.60\,\mathrm{bar}$ vs. Exp. Target $8.06\,\mathrm{bar}$ (+$19.1\,\%$)
- Dataset 3 (Woschni): Sim. IMEP $9.40\,\mathrm{bar}$ vs. Exp. Target $7.76\,\mathrm{bar}$ (+$21.1\,\%$)
- Dataset 4 (Woschni): Sim. IMEP $9.22\,\mathrm{bar}$ vs. Exp. Target $7.48\,\mathrm{bar}$ (+$23.3\,\%$)

This persistent overprediction of IMEP across all datasets, even when parameters like heat loss (with Woschni for Dataset 1) or peak pressure show reasonable agreement, suggests influences beyond just the selected heat transfer model. Several factors could contribute:

1. **Fixed Wiebe Shape and Idealised Combustion:** The Wiebe function, particularly with fixed shape parameters (a, n, θ_d) tuned for one operating point (Dataset 1), represents an idealised and consistent energy release profile. Actual hydrogen SI combustion, especially under varying lean conditions across Datasets 2, 3, and 4, might exhibit changes in burn rate characteristics (e.g., flame development, burn-out duration) not captured by these fixed shape parameters. This could lead to deviations from the actual work output. While versatile, the Wiebe model is often used for compression-ignition processes. Its application to spark-ignited hydrogen combustion may not fully capture variations in burn rate across different lean operating conditions when only ignition timing is adjusted
2. **Cycle-to-Cycle Variability:** Experimental engine data typically represents an average over numerous individual cycles, each subject to inherent variations. The deterministic 0D simulation, however, predicts a single, idealised cycle based on averaged inputs.

In conclusion, the 0D model demonstrates a reasonable ability to predict general trends in pressure development and heat release for this hydrogen SI engine across various operating points when using fixed Wiebe shape parameters (a, n, θ_d) derived from Dataset 1. This was achieved by adjusting only the start of combustion (θ_s, taken from each experimental dataset) and other key operational inputs (CR, λ, Q_{in}, etc.) for each new condition.

However, for achieving more precise predictions of specific metrics like the rate of pressure rise (dp/dCA) and particularly Indicated Mean Effective Pressure (IMEP) and net work output across this wider range of conditions, further model refinement would likely be beneficial. It is expected that individually tuning the Wiebe shape parameters (a, n, θ_d) for each specific experimental dataset, rather than using a single fixed set, would yield closer agreement with the experimental dp/dCA and IMEP values.

5.2.8. Sensitivity of Hydrogen Simulation to Wiebe Combustion Parameters

To understand the influence of the individual Wiebe function coefficients on the simulated hydrogen combustion, a sensitivity analysis was performed. This study utilised the simulation model configured for experimental Dataset 1 as its baseline. Each of the four primary Wiebe parameters—start of combustion (θ_s), combustion duration (θ_d), and the shape factors 'a' and 'n' were systematically varied from their established baseline values for Dataset 1 (i.e., $\theta_s = -20\,^\circ$CA, $\theta_d = 40\,^\circ$CA, $a = 4.0$, and $n = 3.0$). When one parameter was varied, the other three were held at these baseline settings. As determined in Section 5.2.4, the Woschni heat transfer correlation was employed for all simulations within this sensitivity study. The effects of these parameter variations were assessed by comparing the simulated outputs for in-cylinder pressure, average cumulative heat release, average Rate of Heat Release (aROHR), and the rate of pressure rise (dp/dCA) against the experimental data from Dataset 1. The outcomes are presented graphically in Figures 5.6 through 5.9.

Sensitivity to Start of Combustion (θ_s):

The start of combustion, θ_s, directly dictates the phasing of the entire energy release event (Figure 5.6). Advancing θ_s shifts the aROHR, pressure rise curve, and peak pressure curve earlier, often increasing peak pressure value. Retarding θ_s delays these events and typically lowers peak pressure. The cumulative heat release curve translates along the crank angle axis with changes in θ_s. The baseline $\theta_s = -20\,^\circ$CA for Dataset 1 provided the best overall alignment with the experimental pressure and aROHR phasing.

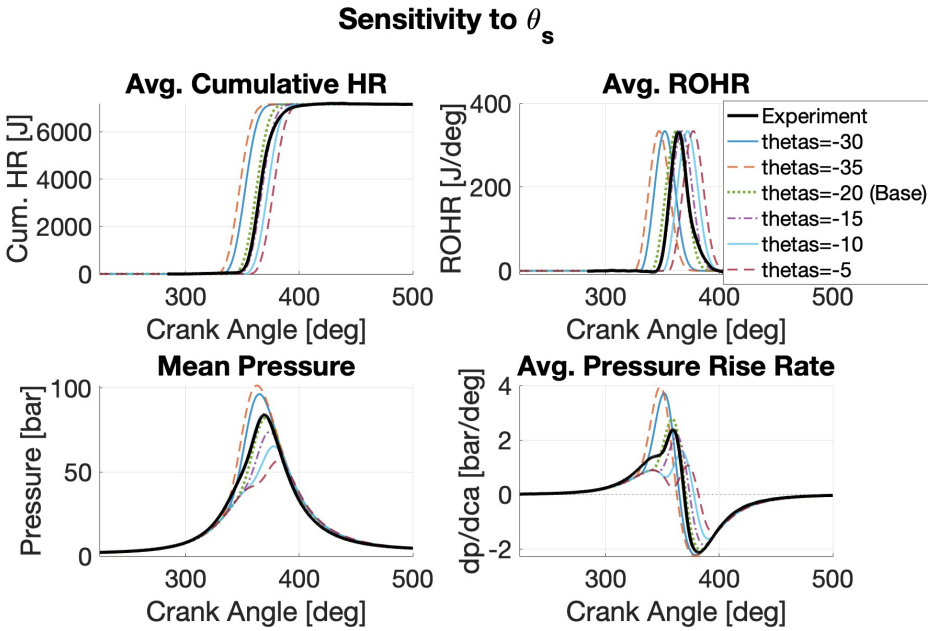

Figure 5.6: Impact of varying Start of Combustion (θ_s) on hydrogen simulation results (relative to Dataset 1 experimental data).

Sensitivity to Combustion Duration (θ_d):
Figure 5.7 shows how the interval of energy release is controlled by the combustion duration, θ_d. Reduced durations (e.g., $25\,°$CA) concentrate combustion, resulting in steeper pressure rises (dp/dθ), higher peak pressures, and narrower, higher aROHR peaks. Extended periods (e.g., $50\,°$CA) spread the heat release, resulting in lower peak pressures, broader, lower aROHR profiles, and gradual pressure development. Accordingly, the cumulative heat release slope also varies. The cumulative heat release curve's slope is directly affected. The baseline $\theta_d = 40\,°$CA for Dataset 1 was found to reasonably match the observed burn duration from the experimental data.

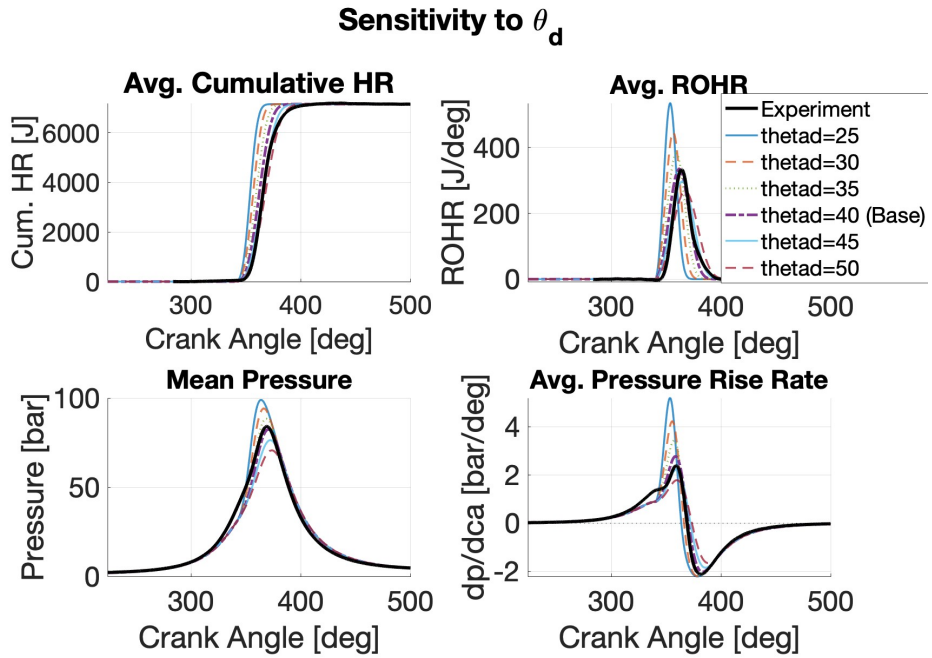

Figure 5.7: Impact of varying Combustion Duration (θ_d) on hydrogen simulation results (relative to Dataset 1 experimental data).

Sensitivity to Wiebe Shape Factor 'a':
The shape factor 'a' primarily influences the initial heat release rate and aROHR peak sharpness (Figure 5.8). Lower 'a' values (e.g., 2.5) result in a more gradual combustion onset and a wider aROHR peak, softening the initial pressure rise. Higher 'a' values (e.g., 5.0) accelerate early combustion, producing a more acute, sometimes advanced, aROHR peak and a quicker initial pressure increase. Its impact on peak pressure magnitude is less pronounced than θ_s or θ_d. The baseline $a = 4.0$ for Dataset 1 provided a good match to the experimental aROHR's initial development and peak form.

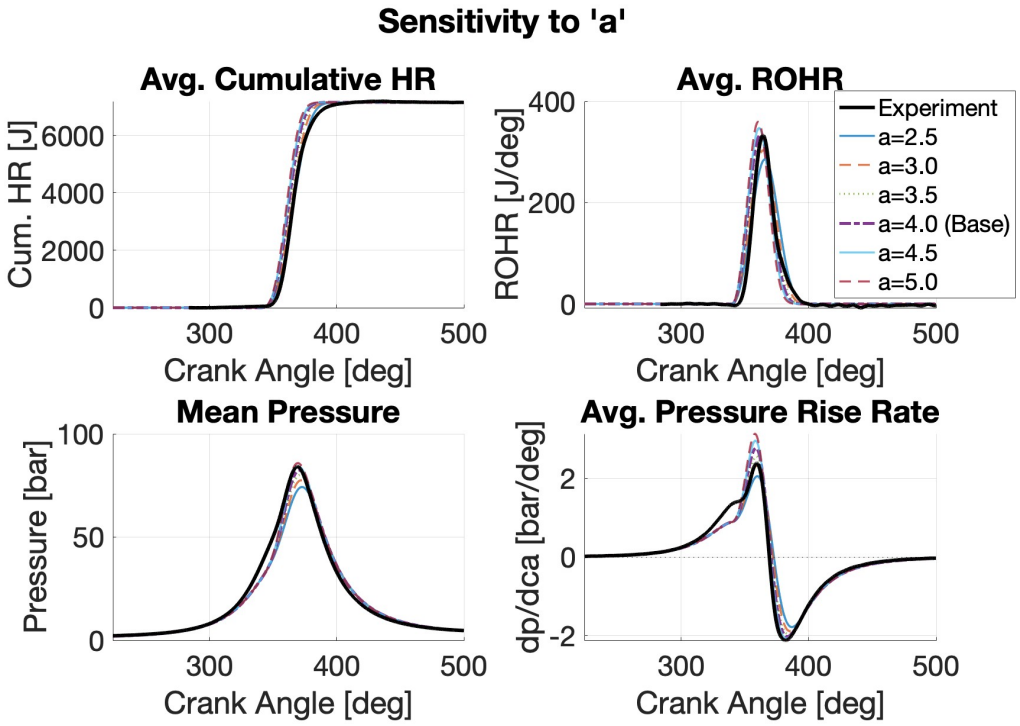

Figure 5.8: Impact of varying Wiebe shape factor 'a' on hydrogen simulation results (relative to Dataset 1 experimental data).

Sensitivity to Wiebe Exponent 'n':
The Wiebe exponent 'n' governs the heat release curve's symmetry and the location of maximum aROHR within the combustion duration (Figure 5.9). Smaller 'n' values (e.g., 1.5) skew the aROHR towards the end of combustion, delaying and reducing its peak, which consequently delays and lowers peak pressure and peak dp/dθ. Larger 'n' values (e.g., 4.0) centralise or advance the bulk of heat release, potentially advancing and increasing aROHR and pressure peaks. The cumulative heat release curve's shape is also affected. The baseline $n = 3.0$ for Dataset 1 offered a balanced heat release profile consistent with the experimental observations.

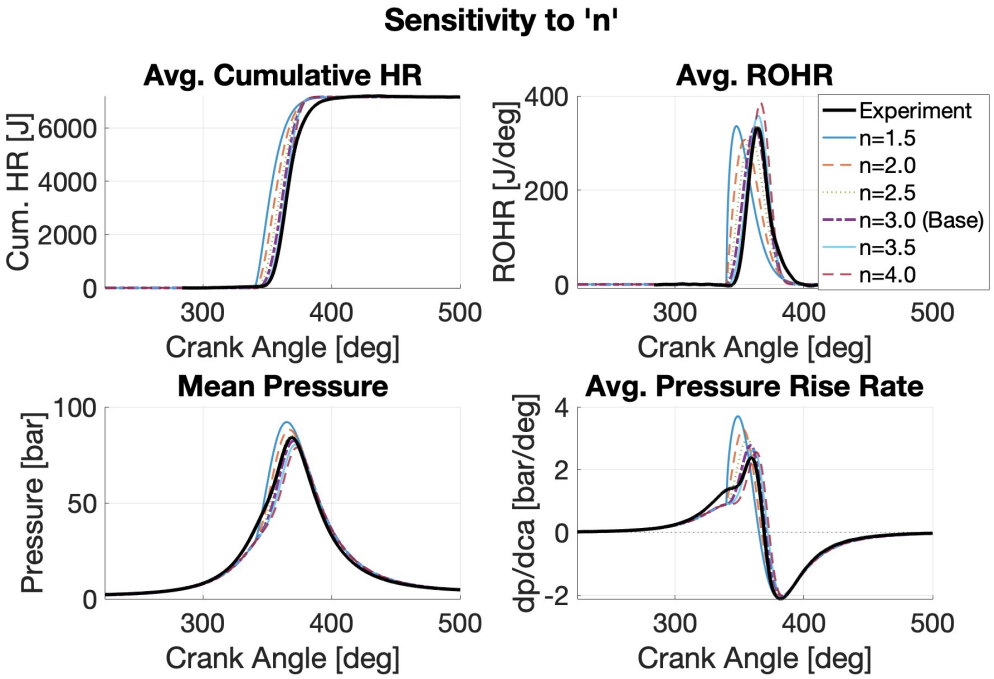

Figure 5.9: Impact of varying Wiebe exponent 'n' on hydrogen simulation results (relative to Dataset 1 experimental data).

5.2.9. Comparative Analysis: Simulated Diesel and Hydrogen Combustion Characteristics

This section transitions to a qualitative comparison of the baseline hydrogen SI simulation (Dataset 1, Section 5.2) and the baseline diesel CI simulation (Chapter 2). Before beginning this comparison, it is important to point out that these simulations are two different single-cylinder research engines, each with its own design and operating parameters specific to a particular fuel. Thus, using the Woschni heat transfer model for both fuels in this particular comparative analysis, the comparison seeks to highlight broad trends and fuel-driven differences predicted by the modelling framework.

To directly compare combustion phenomena that initiate at different absolute crank angles, subsequent plots use an x-axis representing time relative to the Start of Combustion (SoC). The SoC for each fuel is its Wiebe parameter θ_s. First, any crank angle θ is converted to absolute time $t_{abs}(\theta)$ from the simulation's start angle (θ_{start}) using engine speed (N in RPM):

$$t_{abs}(\theta)\ [\text{ms}] = \left(\frac{\theta - \theta_{start}}{N \times 6}\right) \times 1000 \tag{5.2}$$

where $N \times 6$ (Equals to $\omega_{deg} = N(rev/min) \times 360(deg/rev) \times \frac{1}{60}(min/sec)$) gives angular speed in degrees per second. The time relative to SoC (t_{relSoC}) is then:

$$t_{relSoC}(\theta) = t_{abs}(\theta) - t_{abs}(\theta_s) \tag{5.3}$$

This normalisation sets SoC at $t_{relSoC} = 0$ ms for both fuels, synchronising their combustion events for clearer comparative analysis.

Divergent Engine Configurations and Operational Conditions:
The substantial differences in engine design, operating speed, initial state, combustion timing, and particularly the total energy input per cycle, are fundamental to understanding the subsequent comparative analysis of in-cylinder processes.Table 5.4 summarises the key parameters that differentiate these two modelled scenarios.

Table 5.4: Comparison of Key Engine and Operating Parameters for Diesel and Hydrogen Simulations

Parameter	Diesel Simulation	Hydrogen Simulation
Engine Geometry & Base Setup		
Compression Ratio (CR)	21.500	10.840
Bore	0.104 m	0.170 m
Stroke	0.085 m	0.180 m
Displacement Volume	0.722 L	4.084 L
Engine Speed	3000.000 RPM	1500.000 RPM
Initial Conditions at BDC		
Pressure (P_{bdc})	100.000 kPa	166.450 kPa
Temperature (T_{bdc})	300.000 K	320.370 K
Wiebe Combustion Parameters		
Start of Combustion (θ_s)	−9.000°	−20.000°
Duration (θ_d)	40.000°	40.000°
Shape Factor (a)	2.000	4.000
Exponent (n)	3.000	3.000
Thermodynamic & Thermal Properties		
Specific Heat Ratio (γ)	1.300	1.349
Effective Wall Temperature (T_{wall})	500.000 K	446.300 K
Energy Input & Mass		
Target Net Heat Release	1488.000 J/cycle	7155.000 J/cycle
In-cylinder Mass Loss	Negligible (Modelled as Zero)	

Comparison of In-Cylinder Processes:

1. Normalized Pressure Development (vs. CA rel. SoC): The in-cylinder pressure traces are plotted against crank angle in relation to the SoC in Figure 5.10. These traces are normalised by the peak pressure (P/P_{peak}) of each fuel. Without taking into account the absolute peak pressure magnitudes, this normalisation makes it possible to compare the phasing and shapes of the pressure curves. Both fuels reach a normalized peak of 1.0. The diesel simulation (Engine D) achieves its peak normalized pressure at 26.0 after its SoC. The hydrogen simulation (Engine H) reaches its normalized peak slightly later, at 30.6 after its SoC.

Before SoC (during late compression), the diesel trace shows a relatively higher normalized pressure due to its much higher compression ratio. After SoC, the hydrogen pressure trace rises more steeply relative to its own peak and appears somewhat broader around its peak compared to diesel, suggesting a different character to its pressure development post-ignition despite the normalization.

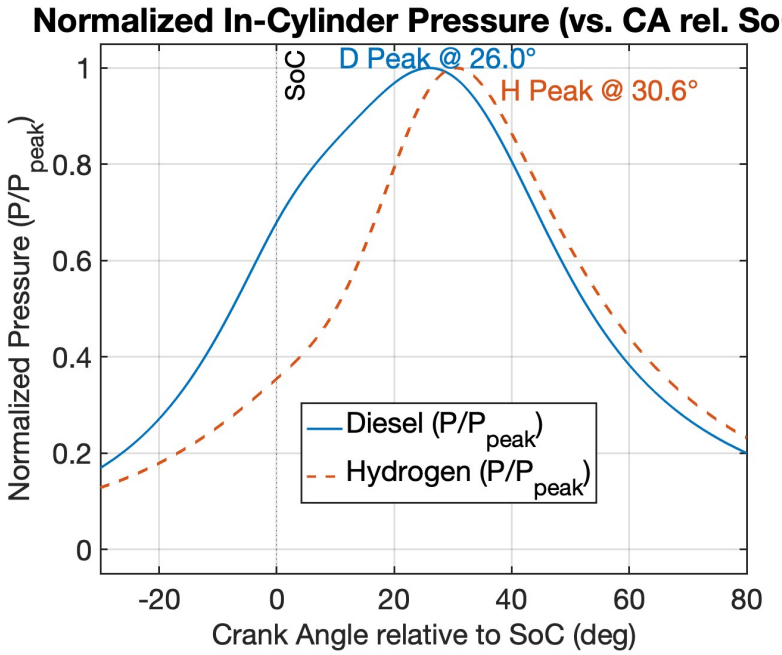

Figure 5.10: Normalized In-Cylinder Pressure (P/P_{peak}) for Diesel and Hydrogen vs. Crank Angle relative to SoC.

2. Normalized Combustion Rate Characteristics (vs. CA rel. SoC): Figure 5.11 compares the average Rate of Heat Release (aROHR), normalized by each fuel's total heat input per cycle (Q_{in}) and expressed as a percentage of Q_{in} released per degree crank angle. This allows a direct comparison of the burn rate shapes and intensities relative to the total energy available.

After its SoC, hydrogen shows a much higher peak normalised aROHR ($4.67\,\%\mathrm{Q_{in}/deg}$) at 22.0. Normalised aROHR for diesel peaks later at 27.7 after its SoC and is lower at $3.70\,\%\mathrm{Q_{in}/deg}$. Given that hydrogen has faster flame speeds and the Wiebe '$a = 4$' parameter for the hydrogen simulation promotes a vigorous initial burn, this indicates a more intense (higher rate relative to its total energy) and slightly earlier-peaking combustion for hydrogen once it is initiated. The diesel combustion, with $a = 2$, shows a relatively less intense peak rate. The shapes of the normalized aROHR curves also differ, with hydrogen showing a sharper rise and fall.

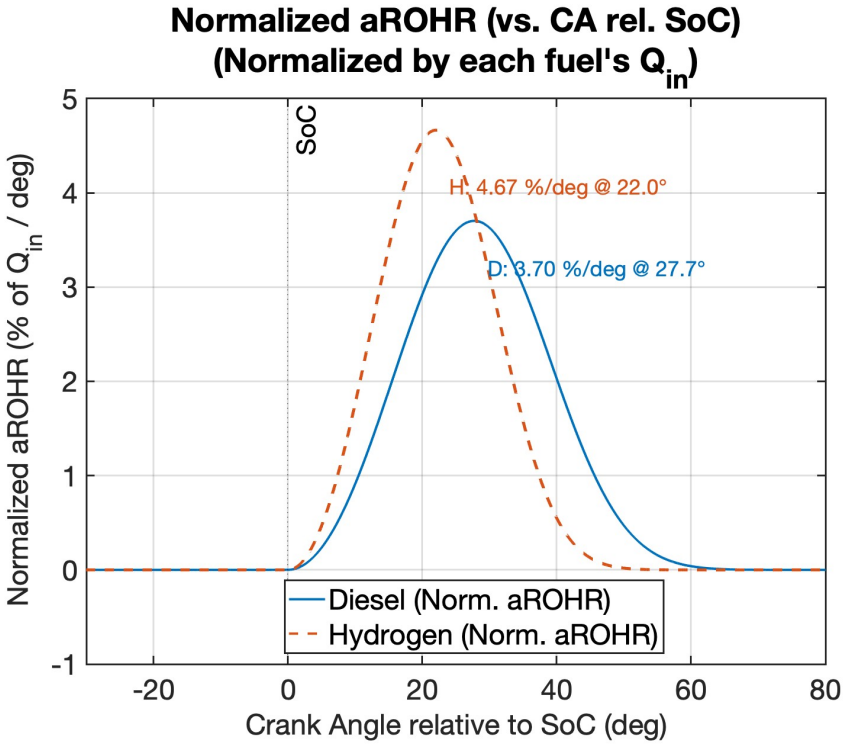

Figure 5.11: Normalized Average Rate of Heat Release (aROHR as % of Q_{in}/deg) for Diesel and Hydrogen vs. Crank Angle relative to SoC.

3. Normalized Cumulative Energy Release and P-V Cycle Shape: Plotting the cumulative heat release normalized by each fuel's maximum (Figure 5.12, shown against time relative to SoC) further illustrates that hydrogen completes its energy release slightly more rapidly in the time domain after SoC. This aligns with its higher peak normalized aROHR and its Wiebe 'a' parameter.

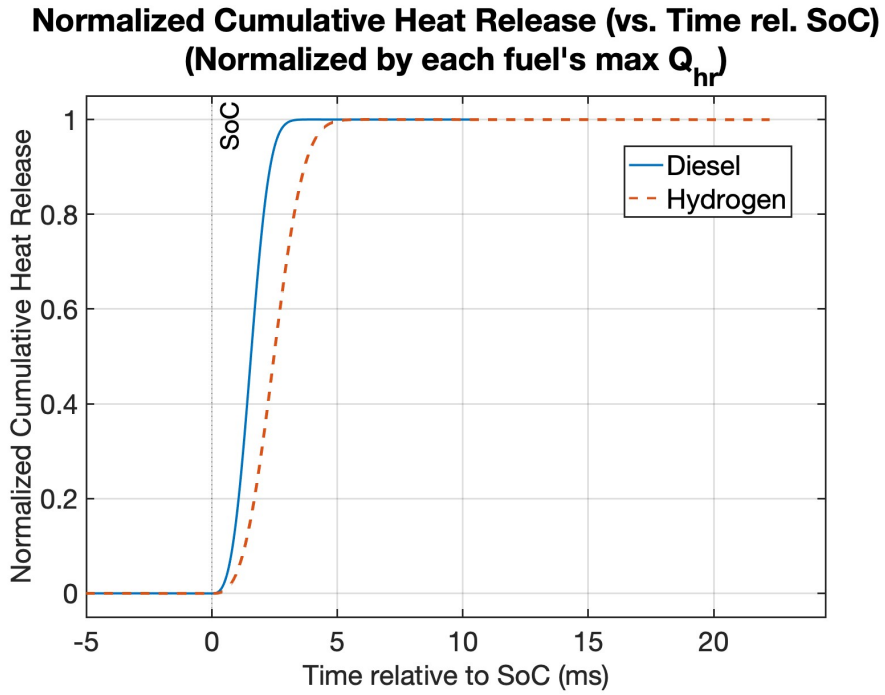

Figure 5.12: Normalized Cumulative Heat Release Profiles (Diesel vs. Hydrogen) vs. Time from Start of Combustion (SoC).

The normalized P-V diagrams (Figure 5.13), where volume is normalized by displacement and pressure by its respective peak, highlight differences in cycle shape. The plot includes theoretical isentropic compression lines for both engines, starting from their respective BDC conditions and using their specific γ values, normalized similarly. The actual compression lines for both diesel and hydrogen lie below their respective isentropic compression lines, indicating heat loss during compression. Diesel has a higher normalised pressure rise during compression due to its higher compression ratio (21.5 vs. 10.84). While both fuels achieve a normalised peak pressure of 1.0, diesel does it at a slightly lower normalised volume. The diesel cycle's higher compression ratio and particular heat release properties result in a larger area enclosed by the cycle in the diagram.

For the expansion stroke, the actual lines for both fuels lie above their respective theoretical isothermal expansion curves. This occurs because combustion continues to release significant heat even after peak pressure has passed. This demonstrates that the actual expansion is a complex polytropic process, shaped by the interplay of work output, continued combustion, and heat loss, with the distinct paths for diesel and hydrogen reflecting their unique heat release profiles.

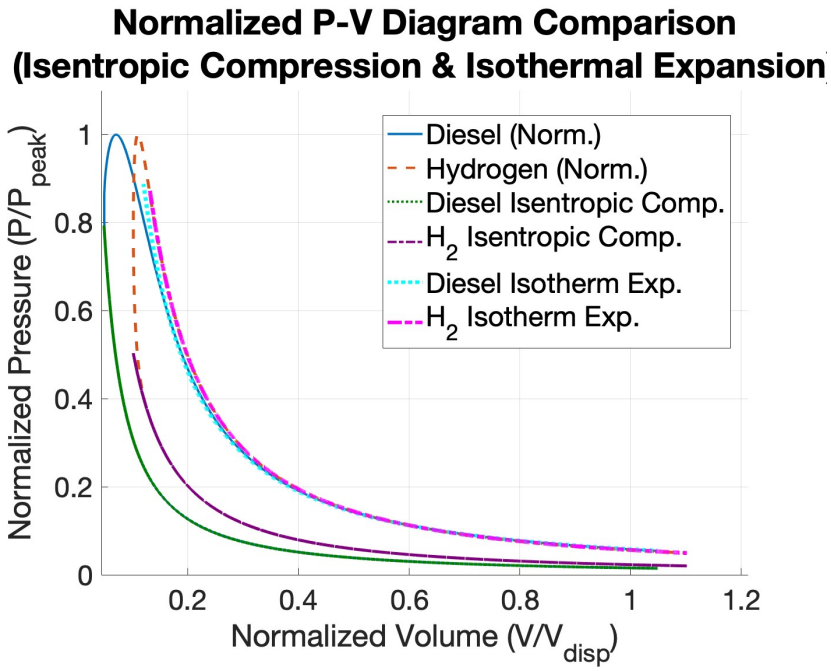

Figure 5.13: Normalized P-V Diagram Comparison (Diesel vs. Hydrogen), with Isentropic Compression Lines. Pressure normalized by peak, volume by displacement.

4. Heat Transfer Predictions (Time-Aligned to SoC): Fuel type significantly influences predicted heat transfer, with outcomes varying by the chosen correlation (Woschni, Hohenberg, Sitkei, Assanis), as shown in Figures 5.14, 5.15, and 5.16. Each figure presents subplots for these four correlations, comparing diesel and hydrogen for Heat Transfer Coefficient (HTC), heat flux (q"), and total heat transfer rate (Q_{ht}), respectively.

4.1 Heat Transfer Coefficient (HTC) (Figure 5.14):
All four correlations predict a higher peak HTC for the diesel simulation than for hydrogen. For instance, with Hohenberg, diesel's peak HTC is $2668\,\mathrm{W/m^2{-}K}$ versus hydrogen's $2425\,\mathrm{W/m^2{-}K}$; Woschni shows diesel at 2629 vs. hydrogen at $2354\,\mathrm{W/m^2{-}K}$. This consistent trend likely reflects the diesel engine's higher speed and compression ratio influencing the empirical HTC terms.

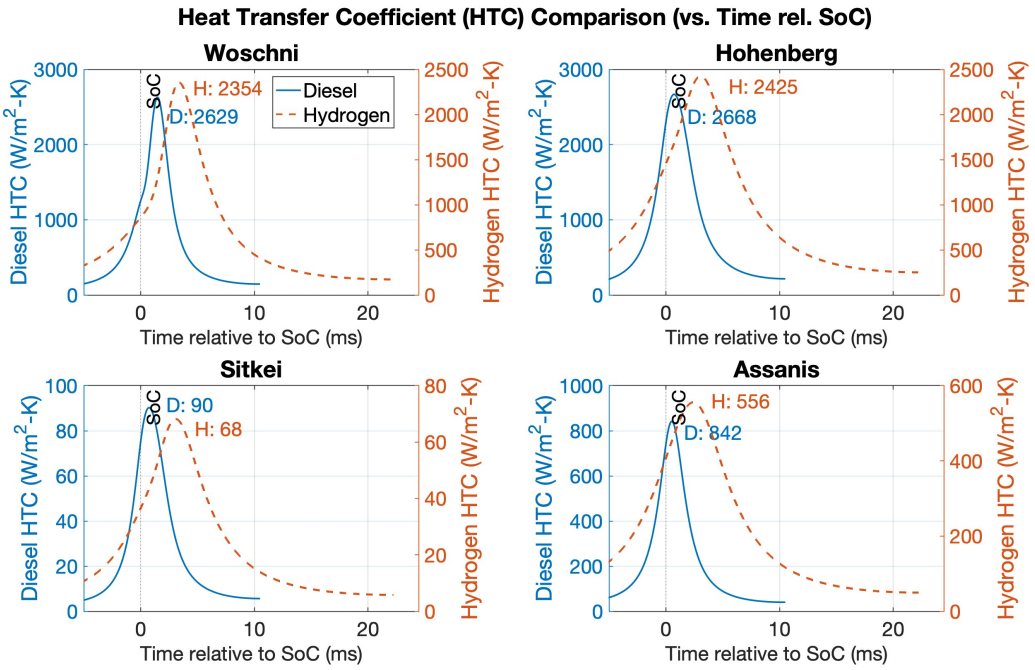

Figure 5.14: Heat Transfer Coefficient (HTC) Comparison across all models (Diesel vs. Hydrogen) vs. Time from SoC.

4.2 Heat Flux (q") (Figure 5.15):

The peak heat flux comparison is mixed. Hohenberg and Assanis predict a higher peak q" for hydrogen (Hohenberg: H_2 2.79 vs. Diesel $2.48\,\mathrm{MW/m^2}$). Conversely, Woschni shows a higher peak q" for diesel (Diesel 2.93 vs. H_2 $2.75\,\mathrm{MW/m^2}$), while Sitkei predicts very similar low peak values ($0.08\,\mathrm{MW/m^2}$) for both. The instances where hydrogen shows higher q" despite lower HTC highlight the impact of the gas-to-wall temperature difference, particularly relative to each engine's specific wall temperature.

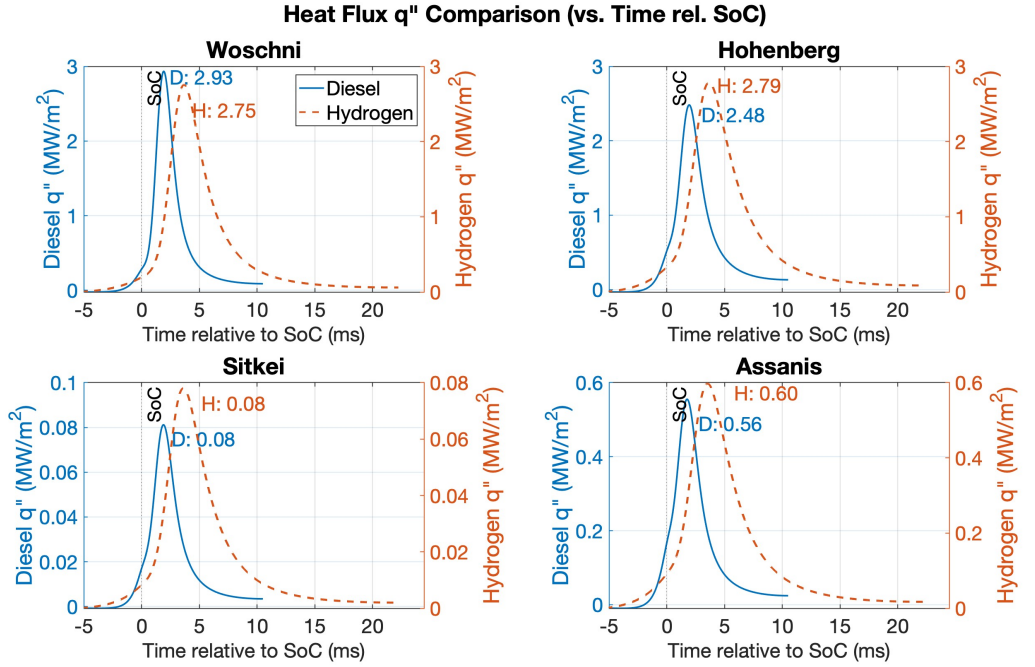

Figure 5.15: Heat Flux (q") Comparison across all models (Diesel vs. Hydrogen) vs. Time from SoC.

4.3 Heat Transfer Rate (Q_{ht}) (Figure 5.16):
A consistent and striking trend is observed for the total instantaneous heat transfer rate (Q_{ht}): hydrogen exhibits a dramatically higher peak Q_{ht} across all four correlations. For example, with Hohenberg, hydrogen's peak Q_{ht} is $156.0\,\mathrm{kW}$ compared to diesel's $47.2\,\mathrm{kW}$; for Woschni, it is $154.3\,\mathrm{kW}$ (H_2) versus $55.8\,\mathrm{kW}$ (Diesel). This is primarily due to the hydrogen engine's significantly larger combustion chamber surface area, which amplifies the heat transfer even when q" values are comparable or lower than diesel's. This results in substantially greater total cycle heat loss for the hydrogen simulation, as noted in Table 5.5.

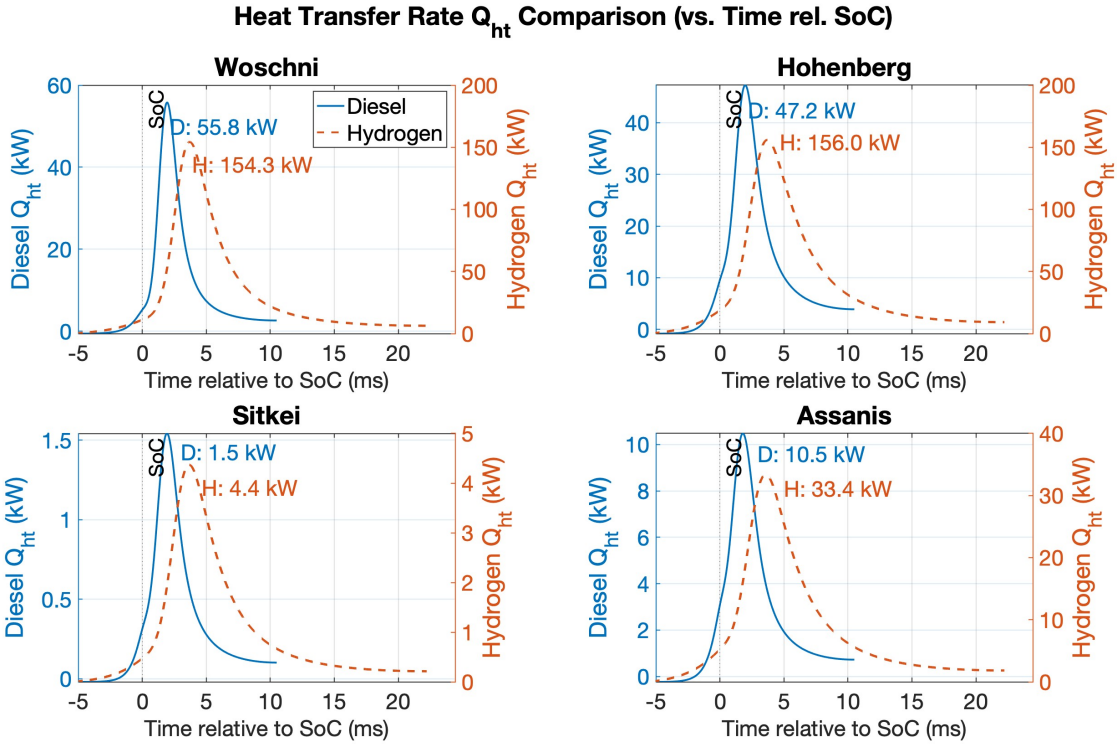

Figure 5.16: Heat Transfer Rate (Q_{ht}) Comparison across all models (Diesel vs. Hydrogen) vs. Time from SoC.

5. Overall Performance and Energy Balance Summary: A summary of the key performance metrics and energy balance components for both simulations is presented in Table 5.5.

Table 5.5: Summary of Key Performance Metrics and Energy Balance (Hohenberg HTC Model)

Parameter	Diesel Sim.	Hydrogen Sim.
Energy Input & Release		
Fuel Energy per Cycle (Input, J)	1487.70	8396.10
Total Actual Heat Release (Wiebe, J)	1487.70	7155.00
Energy Partitioning (Woschni Model)		
Net Work Output (J)	746.84	3937.48
Total Heat Loss (J)	150.35	361.17
Internal Energy Change (End-Start, J)	625.54	3113.89
Performance Indicators		
Thermal Efficiency (%)	50.20	55.03
IMEP (bar)	10.34	9.64
Volumetric Efficiency (%)	105.75	105.85
Combustion Phasing (Wiebe)		
Start of Combustion (θ_s, °CA)	-9.00	-20.00
Duration (θ_d, °CA)	40.00	40.00
Thermal Conditions		
Peak Gas Temperature (K)	1916.00	1651.00
Peak Pressure (MPa)	6.80	8.20
Avg. Gas Temperature (K)	858.60	768.70
Avg. Hohenberg HTC ($\mathrm{W\,m^{-2}\,K^{-1}}$)	611.50	693.90
Assumed Wall Temperature (K)	500.00	446.30

These comparative simulations, which are based on different engine platforms, capture the expected differences resulting from engine design and fuel characteristics. The properties of hydrogen influence peak pressures and heat transfer dynamics by enabling a quick, intense combustion event. Higher compression-end and peak cycle temperatures are a result of diesel's higher compression ratio.

6

Discussion, Conclusions, and Future Work

This thesis developed and assessed a zero-dimensional (0D) thermodynamic engine model in MATLAB. The model was first applied to a diesel compression-ignition (CI) engine and then adapted for a hydrogen-fuelled spark-ignition (SI) engine. This chapter reviews the main results, discusses their meaning, presents overall conclusions, and suggests paths for further research.

6.1. Discussion of Key Findings

The research provided several insights into the 0D model's performance and the effects of different sub-models and fuels.

6.1.1. Diesel Engine Simulation

The 0D model for the diesel engine (Hatz 1D90E) generally matched key in-cylinder data (pressure, temperature, heat release rate) from a similar published engine (Kubota 140) during initial validation (Chapter 4). This confirmed the basic soundness of the thermodynamic setup and the initial Wiebe combustion parameters for diesel.

A key finding was that the choice of heat transfer correlation (Woschni, Hohenberg, Sitkei, Assanis) greatly affected predicted total heat loss, which in turn changed the calculated work and efficiency (Section 3.3.6). For instance, whereas Hohenberg and Woschni showed greater heat loss and lower efficiency, Sitkei predicted very low heat loss and high efficiency. This demonstrates how crucial the choice of heat transfer model is in 0D simulations and how it can lead to a variety of performance predictions.

Subsequent enhancements to the diesel model (detailed in Section 4.2) further refined predictions:

- **Double Wiebe Function:** Implementing a two-stage Wiebe model (Eq. 4.1) led to an earlier start of combustion, a higher initial peak aROHR (e.g., $104\,\mathrm{J/°CA}$ vs. $55\,\mathrm{J/°CA}$ for single Wiebe with Hohenberg HTC), and higher peak gas temperatures, influencing predicted heat transfer rates across all HTC correlations.
- **Temperature-Dependent $\gamma(T)$:** In contrast to a constant $\gamma = 1.3$, the Gatowski model (Eq. 4.2) produced slightly lower peak temperatures but higher peak cylinder pressures. The Assanis heat transfer model showed notable sensitivity to these $\gamma(T)$-induced changes.
- **Exhaust Gas Constant R:** Adjusting R for exhaust composition had a minimal effect on the main performance metrics but it slightly altered the volumetric efficiency.

These refinements demonstrated the model's capacity to incorporate more detailed physics, with the double Wiebe and varying γ having tangible effects.

6.1.2. Hydrogen SI Engine Simulation

Adapting the 0D model to a hydrogen SI engine tested its flexibility. After tuning Wiebe parameters for a baseline experimental hydrogen dataset (Dataset 1), the simulation matched experimental pressure and heat release profiles well (Section 5.2.3).

When comparing the four heat transfer correlations against experimental targets for Dataset 1 (heat loss, work, IMEP), the Woschni model gave the most balanced results, especially for heat loss. Using these fixed Wiebe shape parameters (a, n, θ_d) and the Woschni HTC model, simulations for three additional hydrogen datasets (with adjusted ignition timing θ_s and operating inputs) showed that the model could reasonably predict trends in pressure and aROHR (Section 5.2.5). However, the rate of pressure rise (dp/dCA) showed some mismatches, and IMEP was consistently overestimated. This suggests that while a fixed Wiebe shape is a fair approximation for lean hydrogen SI combustion if ignition is timed correctly, more advanced combustion modelling or Wiebe parameters that change with operating conditions might be needed for higher accuracy across a wide range. The Wiebe parameter sensitivity study (Section 5.2.8) confirmed how each parameter affects the combustion shape.

6.1.3. Comparing Diesel and Hydrogen Simulations

Even though the diesel CI and hydrogen SI simulations used models of different engines, qualitative comparisons (Section 5.2.9) highlighted basic fuel differences. Hydrogen's fast burn led to high peak heat release and pressure rise rates. The diesel's high compression ratio led to higher temperatures at the start of combustion and often higher peak cycle temperatures. Normalized plots helped compare the shapes of processes like P-V diagrams and cumulative heat release.

6.1.4. Model Limitations

The 0D single-zone approach simplifies the complex reality inside the cylinder by assuming uniform conditions. This neglects temperature and composition variations important in actual CI combustion and hydrogen flame behaviour. Although empirical Wiebe functions are computationally quick, they depend on tuning and might not always be accurate. Despite being straightforward, the Euler forward integration method requires small step sizes for stability and is less accurate than higher-order techniques. The constant overestimation of IMEP for hydrogen raises the possibility that other small losses or real-world variables, such as incomplete combustion in extremely lean mixtures, are not taken into account.

6.2. Conclusions

The main conclusions from this research are:

1. The developed 0D thermodynamic model can simulate key in-cylinder events for both diesel CI and hydrogen SI engines with reasonable accuracy when appropriately tuned.
2. The choice of heat transfer correlation significantly impacts predicted heat loss, work, and efficiency. For the hydrogen SI engine case, Woschni provided the most balanced results against experimental targets.
3. A Wiebe function with carefully tuned parameters can represent bulk heat release for both diesel and hydrogen. For hydrogen SI, fixed Wiebe shape parameters (with adjusted ignition timing) captured general trends across different operating points, but showed limitations in predicting dp/dCA and IMEP accurately, suggesting a need for more adaptive combustion modelling for broader SI applicability.
4. The model successfully highlighted expected qualitative differences between diesel and hydrogen combustion based on their fuel properties and the different engine setups.
5. The 0D single-zone simplification and empirical sub-models introduce inherent limitations, contributing to discrepancies between simulation and experimental results, especially for overall performance metrics like IMEP.

6.3. Recommendations for Future Work

These steps would enhance the model's predictive capabilities and would broaden its applications:

1. **Dedicated Experimental Validation and Calibration:** Conducting specific diesel-fuelled experiments on the Hatz 1D90E engine and then investigating the possibility of testing and retrofitting the same engine with hydrogen would be an important next step. By offering a standardised engine platform for direct model validation and calibration, this would greatly lower the uncertainty involved in using different literature data sources and enable more accurate tuning of the combustion and heat transfer sub-models for both fuels on the same base engine.
2. **Full Cycle & Losses:** Extend the model to include gas exchange strokes and incorporate mechanical friction models to predict brake performance.
3. **Emissions:** Add sub-models for key emissions (NO_x, soot).
4. **CFD-based Heat-Loss Modelling:** Employ CFD to predict heat loss with higher fidelity by resolving combustion-induced turbulence and spatial temperature gradients within the cylinder.

A

Appendix A: Additional Plots

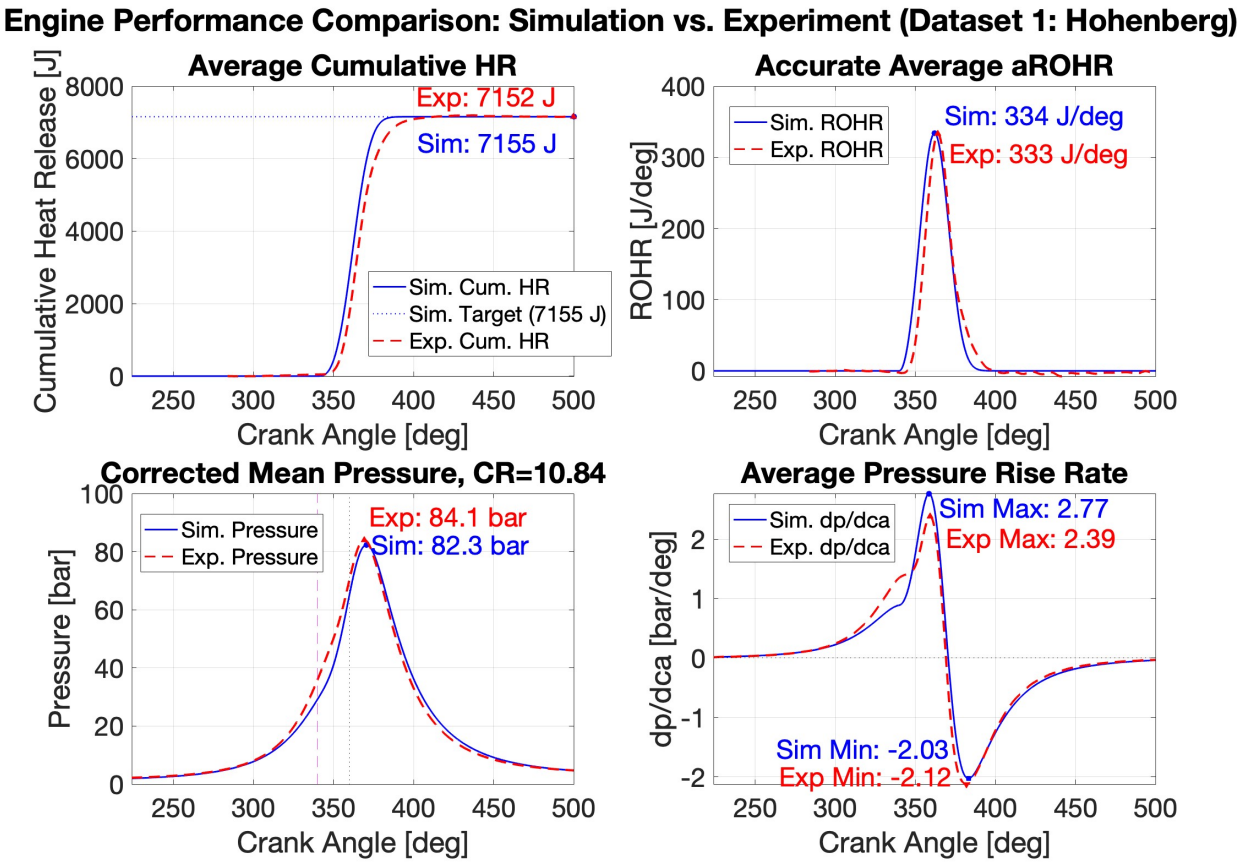

Figure A.1: Engine Performance Comparison: Hydrogen Simulation (with Hohenberg HTC model) vs. Experiment

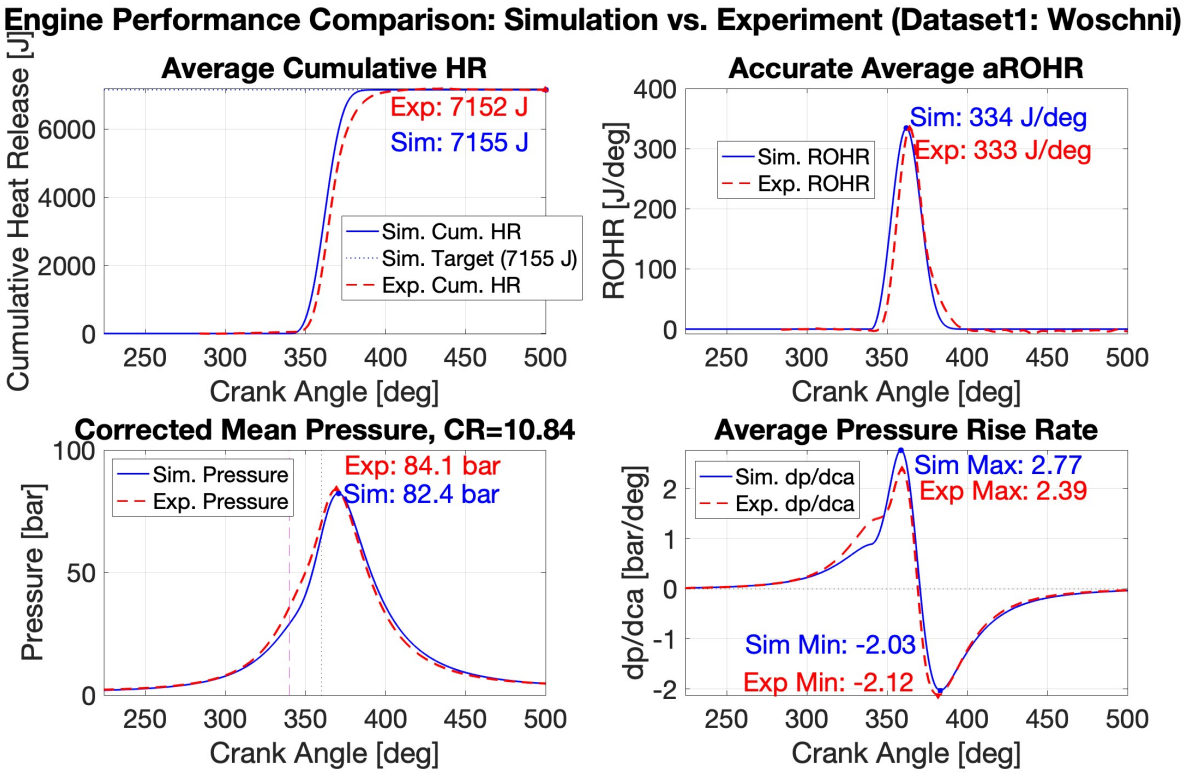

Figure A.2: Engine Performance Comparison: Hydrogen Simulation (with Woschni HTC model) vs. Experiment

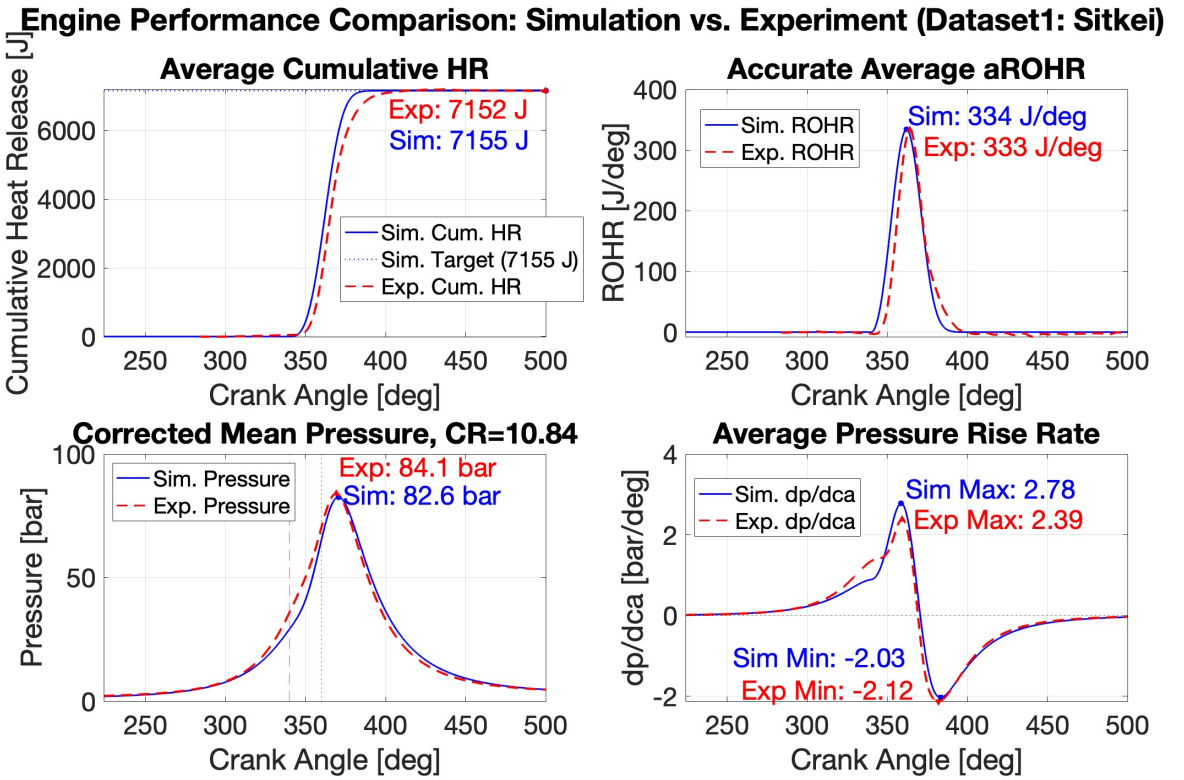

Figure A.3: Engine Performance Comparison: Hydrogen Simulation (with Sitkei HTC model) vs. Experiment

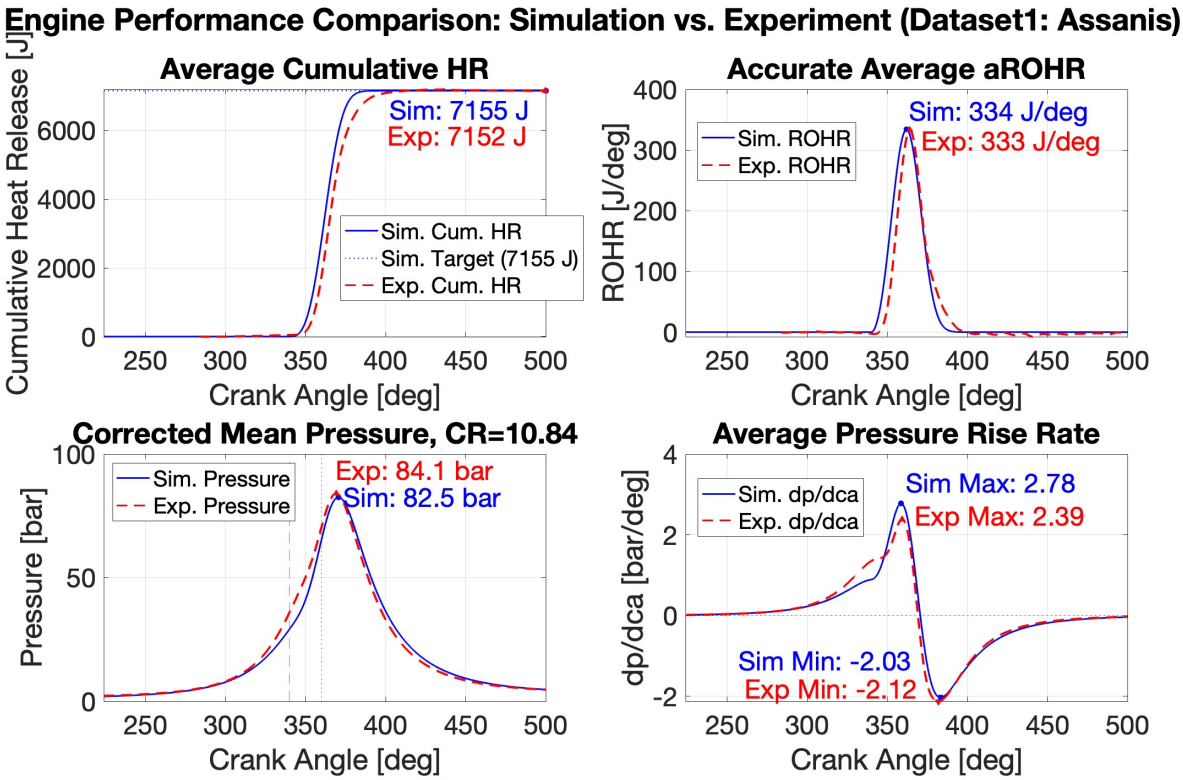

Figure A.4: Engine Performance Comparison: Hydrogen Simulation (with Assanis HTC model) vs. Experiment

B

Appendix B: Additional Calculations

B.1. Derived Gas Properties for Diesel Simulation

Using the assumed constant $\gamma = 1.3$ and specific gas constant $R = 0.2869\,\mathrm{kJ\,kg^{-1}\,K^{-1}}$, the specific heats for the diesel simulation were:

- $c_p = \gamma R/(\gamma - 1) \approx 1.2436\,\mathrm{kJ\,kg^{-1}\,K^{-1}}$
- $c_v = R/(\gamma - 1) \approx 0.9563\,\mathrm{kJ\,kg^{-1}\,K^{-1}}$

The initial air density at BDC was calculated as $\approx 1.1618\,\mathrm{kg\,m^{-3}}$.

B.2. Stoichiometric Combustion of Diesel

The complete combustion of dodecane with the theoretical (stoichiometric) amount of air can be represented by the balanced chemical equation [32]:

$$\mathrm{C_{12}H_{23}} + x_s(\mathrm{O_2} + 3.76\mathrm{N_2}) \rightarrow y_s\mathrm{CO_2} + z_s\mathrm{H_2O} + 3.76x_s\mathrm{N_2} \tag{B.1}$$

where $x_s, y_s,$ and z_s are the stoichiometric coefficients. Balancing for each element:

- Carbon (C): $12 = y_s \implies y_s = 12$
- Hydrogen (H): $23 = 2z_s \implies z_s = 11.5$
- Oxygen (O): $2x_s = 2y_s + z_s \implies 2x_s = 2(12) + 11.5 = 35.5 \implies x_s = 17.75$

Thus, the stoichiometric equation is:

$$\mathrm{C_{12}H_{23}} + 17.75(\mathrm{O_2} + 3.76\mathrm{N_2}) \rightarrow 12\mathrm{CO_2} + 11.5\mathrm{H_2O} + 66.73\mathrm{N_2} \tag{B.2}$$

From this, the stoichiometric AFR (mass basis) can be calculated as approximately 14.5.

Combustion with Excess Air (Actual AFR = 26.6)

The simulation operates with an actual AFR of 26.6, which is significantly leaner than the stoichiometric AFR of $\sim$14.5. The air-fuel equivalence ratio, λ, quantifies this excess air:

$$\lambda = \frac{\mathrm{AFR_{actual}}}{\mathrm{AFR_{stoichiometric}}} = \frac{26.6}{14.5} \approx 1.834 \tag{B.3}$$

This means that 1.834 times the stoichiometric amount of air is supplied. The number of moles of $\mathrm{O_2}$ supplied per mole of fuel is therefore $x_a = \lambda \cdot x_s = 1.834 \cdot 17.75 \approx 32.55$ moles. The combustion equation with excess air becomes:

$$\mathrm{C_{12}H_{23}} + x_a(\mathrm{O_2} + 3.76\mathrm{N_2}) \rightarrow y_s\mathrm{CO_2} + z_s\mathrm{H_2O} + (x_a - x_s)\mathrm{O_2} + 3.76x_a\mathrm{N_2} \tag{B.4}$$

Substituting the values:

$$C_{12}H_{23} + 32.55(O_2 + 3.76N_2) \rightarrow 12CO_2 + 11.5H_2O + (32.55 - 17.75)O_2 + (3.76 \cdot 32.55)N_2 \quad \text{(B.5)}$$

This simplifies to:

$$C_{12}H_{23} + 32.55O_2 + 122.40N_2 \rightarrow 12CO_2 + 11.5H_2O + 14.80O_2 + 122.40N_2 \quad \text{(B.6)}$$

The products include CO_2, H_2O, unreacted (excess) O_2, and N_2.

Molar and Mass Percentages of Combustion Products

Based on Equation B.6, the composition of the combustion products for the lean AFR of 26.6 can be estimated. These percentages are relevant for determining average properties of the exhaust gas, such as the specific gas constant R used in some thermodynamic calculations.

Molar Percentages:

The total moles of products per mole of fuel are $N_{prod} = 12(CO_2)+11.5(H_2O)+14.80(O_2)+122.40(N_2) = 160.7$ moles. The molar percentages are then:

- % $CO_2 = (12/160.7) \times 100\% \approx$ 7.47%
- % $H_2O = (11.5/160.7) \times 100\% \approx$ 7.16%
- % $O_2 = (14.80/160.7) \times 100\% \approx$ 9.21%
- % $N_2 = (122.40/160.7) \times 100\% \approx$ 76.16%

Mass Percentages:

Using molar masses (CO_2: $\sim$44.01 g/mol, H_2O: $\sim$18.02 g/mol, O_2: $\sim$32.00 g/mol, N_2: $\sim$28.02 g/mol), the total mass of products per mole of fuel is approximately $4638.6\,\text{g}$. The mass percentages are:

- % $CO_2 \approx$ 11.39%
- % $H_2O \approx$ 4.47%
- % $O_2 \approx$ 10.20%
- % $N_2 \approx$ 73.94%

These calculations provide an estimate of the primary combustion product composition under the specified lean operating conditions, highlighting the presence of significant excess oxygen.

B.3. Estimated Hydrogen Combustion Product Composition (Dataset 1):

To approximate the composition of the primary combustion products for the lean hydrogen operation ($\lambda \approx 3.245$), a stoichiometric analysis was performed. Below is the calculation for dataset 1 as an example. The complete combustion of hydrogen (H_2) with the theoretical (stoichiometric) amount of air ($x_{s,H2} = 0.5$ moles O_2) is:

$$H_2 + 0.5(O_2 + 3.76N_2) \rightarrow H_2O + 1.88N_2 \tag{B.7}$$

Given $\lambda \approx 3.245$, the actual moles of O_2 supplied per mole of H_2 is $x_{a,H2} = \lambda \cdot x_{s,H2} \approx 1.6225$. The combustion equation with excess air thus becomes:

$$H_2 + 1.6225O_2 + 6.1006N_2 \rightarrow 1H_2O + 1.1225O_2 + 6.1006N_2 \tag{B.8}$$

The products are primarily H_2O, unreacted O_2, and N_2. The total moles of these products per mole of H_2 fuel are $N_{prod,H2} = 1 + 1.1225 + 6.1006 = 8.2231$ moles. The molar fractions (y_i) of the major products are:

- $y_{H_2O} = 1.0/8.2231 \approx 0.12160$
- $y_{O_2} = 1.1225/8.2231 \approx 0.13650$
- $y_{N_2} = 6.1006/8.2231 \approx 0.74190$

Using the molar masses ($M_{H_2O} \approx 18.015\,\mathrm{g\,mol^{-1}}$, $M_{O_2} \approx 31.999\,\mathrm{g\,mol^{-1}}$, $M_{N_2} \approx 28.013\,\mathrm{g\,mol^{-1}}$), the average molar mass of this product mixture ($M_{mix,prod}$) is:

$$M_{mix,prod} = \sum(y_i \cdot M_i) = (0.12160 \cdot 18.015) + (0.13650 \cdot 31.999) + (0.74190 \cdot 28.013) \approx 27.341\,\mathrm{g\,mol^{-1}} \tag{B.9}$$

References

[1] AVL RACETECH. *410 Hp from 2-Liter Displacement – Prototype of the H2-ICE Race Engine from AVL RACETECH Proves Itself on the Testbed*. Press Release. Accessed on May 29, 2025. AVL List GmbH, Oct. 2023. URL: https://www.avl.com/en/press/press-release/410-hp-2-liter-displacement-prototype-h2-ice-race-engine-avl-racetech-proves-itself-testbed.

[2] Hannah Ritchie, Pablo Rosado, and Max Roser. *Energy Production and Consumption*. 2024. URL: https://ourworldindata.org/energy-production-consumption (visited on 03/18/2025).

[3] Stefan Tongur. *Preparing for Takeoff: Analyzing the Development of Electric Road Systems from a Business Model Perspective*. Doctoral Thesis. Stockholm, Sweden, 2018.

[4] R. Vijayagopal et al. "Comparing the Powertrain Energy Densities of Electric and Gasoline Vehicles". In: 2016-01-0903 (2016). DOI: 10.4271/2016-01-0903. URL: https://doi.org/10.4271/2016-01-0903.

[5] Automotive Technology. *What Are the Biggest Challenges Facing Electric Vehicle Adoption Today?* 2023. URL: https://www.automotive-technology.com/articles/what-are-the-biggest-challenges-facing-electric-vehicle-adoption-today (visited on 03/18/2025).

[6] Toyota Europe. *Prototype Corolla Cross Hydrogen Concept*. 2022. URL: https://www.toyota-europe.com/news/2022/prototype-corolla-cross-hydrogen-concept (visited on 03/18/2025).

[7] TNO. *Hydrogen Internal Combustion Engine Accelerates CO2 Reduction*. Oct. 2022. URL: https://www.tno.nl/en/newsroom/insights/2022/10/hydrogen-internal-combustion-engine/ (visited on 03/18/2025).

[8] Lloyd Van Horn Armstrong and Charles Lafayette Proctor. *Diesel Engine: Definition, Development, Types, & Facts*. Feb. 2025. URL: https://www.britannica.com/technology/diesel-engine (visited on 03/18/2025).

[9] John B. Heywood. *Internal Combustion Engine Fundamentals*. illustrated. McGraw-Hill Education, 1988, p. 960. ISBN: 007028637X, 9780070286375.

[10] Gavin W. Jones and Badrul Chowdhury. *Distribution System Operation and Planning in the Presence of Distributed Generation Technology*. May 2008. DOI: 10.1109/TDC.2008.4517274. URL: https://ieeexplore.ieee.org/document/4517274.

[11] Colin R. Ferguson and Allan T. Kirkpatrick. *Internal Combustion Engines: Applied Thermosciences*. 2, illustrated. Wiley, 2001, p. 369. ISBN: 0471356174, 9780471356172.

[12] J. Huang et al. "Experimental Investigation on the Performance and Emissions of a Diesel Engine Fuelled with Ethanol-Diesel Blends". In: *Applied Thermal Engineering* 29 (2009), pp. 2484–2490. DOI: 10.1016/j.applthermaleng.2008.12.016.

[13] A. Irimescu. "Convective Heat Transfer Equation for Turbulent Flow in Tubes Applied to Internal Combustion Engines Operated Under Motored Conditions". In: *Applied Thermal Engineering* 50 (2013), pp. 536–545.

[14] E.C. Trujillo et al. "Methodology for the Estimation of Cylinder Inner Surface Temperature in an Air-Cooled Engine". In: *Applied Thermal Engineering* 31.8-9 (Dec. 2011), p. 1474. DOI: 10.1016/j.applthermaleng.2011.01.033.

[15] Z. Zak et al. "In-Cylinder Heat Transfer Modelling". In: *Journal of Middle European Construction and Design of Cars* 14.3 (Feb. 2016).

[16] B. Lawton. “Effect of Compression and Expansion on Instantaneous Heat Transfer in Reciprocating Internal Combustion Engines”. In: *Proceedings of the Institution of Mechanical Engineers, Part A: Journal of Power and Energy* 201.3 (1987), pp. 175–186. URL: http://dx.doi.org/10.1243/PIME_PROC_1987_201_022_02.

[17] J. Chang et al. *New Heat Transfer Correlation for an HCCI Engine Derived from Measurements of Instantaneous Surface Heat Flux*. Tech. rep. 2004-01-2996. SAE International, 2004. DOI: 10.4271/2004-01-2996. URL: https://doi.org/10.4271/2004-01-2996.

[18] C. D. Rakopoulos and G. C. Mavropoulos. “Experimental Evaluation of Local Instantaneous Heat Transfer Characteristics in the Combustion Chamber of Air-Cooled Direct Injection Diesel Engine”. In: *Energy* 33 (2008), pp. 1084–1099.

[19] Mior A. Said et al. “Modelling of In-Cylinder Convective Heat Transfer Losses to the Combustion Chamber Wall of Compression-Ignition Engine”. In: *Proceedings of the Second International Conference on Advances in Mechanical, Aeronautical and Production Techniques (MAPT 2014)*. ISBN: 978-1-63248-037-8. Institute of Research Engineers and Doctors, USA, 2014, pp. 74–77. DOI: 10.15224/978-1-63248-037-8-101.

[20] Shahzad Bobi and Yossapong Laoonual. “Evaluation of Heat Loss to Cylinder Wall of Compression Ignition Engine by Heat Transfer Models”. In: *GMSARN International Journal* 16 (2022), pp. 240–246.

[21] Johannes Michl et al. “Derivation and validation of a heat transfer model in a hydrogen combustion engine”. In: *Applied Thermal Engineering* 98 (2016), pp. 502–512. DOI: 10.1016/j.applthermaleng.2015.12.062.

[22] Bowen Wang et al. “Combustion and heat transfer characteristics of a heavy-duty low-pressure-direct-injection hydrogen engine with a flat-roof-and-shallow-bowl combustion chamber”. In: *International Journal of Hydrogen Energy* 96 (2024), pp. 597–611. DOI: 10.1016/j.ijhydene.2024.11.359.

[23] Rafig Babayev et al. “Computational comparison of the conventional diesel and hydrogen direct-injection compression-ignition combustion engines”. In: *Fuel* 307 (2022), p. 121909. DOI: 10.1016/j.fuel.2021.121909.

[24] Joachim Demuynck et al. “Heat loss comparison between hydrogen, methane, gasoline and methanol in a spark-ignition internal combustion engine”. In: *World Hydrogen Energy Conference 2012*. Vol. 29. 2012, pp. 138–146. DOI: 10.1016/j.egypro.2012.09.018.

[25] T. Shudo and H. Suzuki. “New Heat Transfer Equation Applicable to Hydrogen-Fuelled Engines”. In: *Proceedings of the ASME Internal Combustion Engine Division Fall Technical Conference*. Paper No. ICEF2002-515. ASME. New Orleans, Louisiana, USA, 2002.

[26] Muhammad Ihsan Shahid et al. “Comparative analysis of different heat transfer models, energy and exergy analysis for hydrogen-enriched internal combustion engine under different operation conditions”. In: *Applied Thermal Engineering* 247 (2024). DOI: 10.1016/j.applthermaleng.2024.123004.

[27] Abdul Sharief, T. K. Chandrashekar, and B. S. Samaga. “Study on Heat Transfer Correlation in IC Engines”. In: *SAE International Powertrains, Fuels and Lubricants Congress*. 2008-01-1816. Shanghai, China: SAE International, June 2008. DOI: 10.4271/2008-01-1816.

[28] M. S. Lounici et al. “Investigation on Heat Transfer Evaluation for a More Efficient Two-Zone Combustion Model in the Case of Natural Gas SI Engines”. In: *Applied Thermal Engineering* (2010). DOI: 10.1016/j.applthermaleng.2010.09.012. URL: https://doi.org/10.1016/j.applthermaleng.2010.09.012.

[29] G. Woschni. *A Universally Applicable Equation for the Instantaneous Heat Transfer Coefficient in the Internal Combustion Engine*. Tech. rep. 670931. SAE International, 1967. URL: https://doi.org/10.4271/670931.

[30] G. F. Hohenberg. *Advanced Approaches for Heat Transfer Calculations*. Tech. rep. 790825. SAE International, 1979. URL: https://doi.org/10.4271/790825.

[31] G. Sitkei and G. V. Ramanaiah. *A Rational Approach for Calculation of Heat Transfer in Diesel Engines*. Tech. rep. 720027. SAE International, 1972. URL: https://doi.org/10.4271/720027.

[32] Prof.dr. Bendiks Jan Boersma. *Internal Combustion Engines MT44100: Lecture Slides*. Course materials for MT44100. 2023–2024.

[33] S. Mauro et al. “Internal Combustion Engine Heat Release Calculation Using Single-Zone and CFD 3D Numerical Models”. In: *International Journal of Energy and Environmental Engineering* 9 (2018), pp. 215–226. DOI: 10.1007/s40095-017-0257-6.

[34] R. Ebrahimi. “Effect of Specific Heat Ratio on Heat Release Analysis in a Spark-Ignition Engine”. In: *Scientia Iranica* 18.6 (Dec. 2011), pp. 1231–1236. DOI: 10.1016/j.scient.2011.11.010.

[35] S. Loganathan. *Performance Simulation of CIDI Engine Fuelled with Alternate Oxygenated Fuel (DME) and Oxygenated (Diglyme) Diesel Blend by Generic Approach with Universal Oxygenate Correction Factor*. Tech. rep. Department of Mechanical Engineering, Aarupadai Veedu Institute of Technology, India, 2011.

[36] Phuong X. Pham. “Influences of Molecular Profiles of Biodiesels on Atomization, Combustion and Emission Characteristics”. PhD thesis. Le Quy Don Technical University, Mar. 2015. DOI: 10.13140/2.1.4430.1609.

[37] A. K. Agarwal et al. “Combustion Characteristics of Diesel Engines”. In: *Applied Energy* 260 (2020), p. 114239. DOI: 10.1016/j.apenergy.2019.114239.

[38] A. Sanli et al. “The influence of engine speed and load on the heat transfer between gases and in-cylinder walls at fired and motored conditions of an IDI diesel engine”. In: *Applied Thermal Engineering* (2008), pp. 1395–1404.

[39] H.S. Soyhan et al. “Evaluation of Heat Transfer Correlations for HCCI Engine Modelling”. In: *Applied Thermal Engineering* 2-3 (2008). HAL identifier: hal-00498971, pp. 541–549. DOI: 10.1016/j.applthermaleng.2008.03.014.

[40] Carmen Chicone. “Chapter 5 - Reaction, Diffusion, and Convection”. In: *An Invitation to Applied Mathematics: Differential Equations, Modeling, and Computation*. 1st. Elsevier, 2017, pp. 85–193. DOI: 10.1016/B978-0-12-804153-6.50005-X.

[41] Hatz Americas. *Hatz 1D90E - D-Series Diesel Engine*. 2025. URL: https://www.hatzamericas.com/hatz-products/d-series/models/1d90e/.

[42] Hatz GmbH & Co. KG. *Hatz Drive Solutions D-Series Industrial Diesel Engines*. Tech. rep. Datasheet, Document No. 70257171. Ernst-Hatz-Str. 16, 94099 Ruhstorf a. d. Rott, Germany: Motorenfabrik Hatz GmbH & Co. KG, Oct. 2022.

[43] R. Stone. *Introduction to Internal Combustion Engines*. 3rd. Macmillan Press Limited, 1999.

[44] Kubota Corporation. *Kubota RT140 Diesel Engine*. https://www.dieselparts.com.au/engines/kubota-diesel-engine-rt140.

[45] H. Zhao, H. Xie, and Z. Peng. “Effect of recycled burned gases on homogeneous charge compression ignition combustion”. In: *Combustion Science and Technology* 177.10 (2005), pp. 1863–1882.

[46] Jinlong Liu and Cosmin E. Dumitrescu. “Single and double Wiebe function combustion model for a heavy-duty diesel engine retrofitted to natural-gas spark-ignition”. In: *Applied Energy* 248 (2019), pp. 95–103. DOI: 10.1016/j.apenergy.2019.04.098.

[47] Shangming Li. “A Temperature-dependent Model of Ratio of Specific Heats Applying in Diesel Engine”. Supervisor: Sergey Ushakov, IMT. Master’s thesis. Norwegian University of Science and Technology, Department of Marine Technology, June 2017.

[48] J. A. Gatowski et al. *Heat release analysis of engine pressure data*. SAE Technical Paper 841359. SAE International, 1984.

[49] Anna Amat Ventayol et al. “Comparative life cycle assessment of hydrogen internal combustion engine and fuel cells in shipping”. In: *International Journal of Hydrogen Energy* 109 (Mar. 2025), pp. 774–788. DOI: 10.1016/j.ijhydene.2025.02.150.